

**ENHANCEMENT OF COOPERATIVE CROSS-POLAR  
RADAR TARGETS**

By

**ANDREW M. UKRAINEC, B. Eng.**

A Thesis  
Submitted to the School of Graduate Studies  
in Partial Fulfilment of the Requirements  
for the Degree  
Doctor of Philosophy

McMaster University  
© Copyright by Andrew M. UkraineC, May 1994

DOCTOR OF PHILOSOPHY (1994)  
(Electrical Engineering)

McMASTER UNIVERSITY  
Hamilton, Ontario

TITLE: Enhancement of Cooperative Cross-polar  
Radar Targets

AUTHOR: Andrew M. Ukraineec, B. Eng. (McMaster University)

SUPERVISOR: Dr. Simon Haykin

NUMBER OF PAGES: xii, 106

**ENHANCEMENT OF COOPERATIVE CROSS-POLAR  
RADAR TARGETS**



# Abstract

A polarimetric radar navigation (PRAN) system makes use of a specially modified marine radar and polarization rotating twist-grid retroreflectors in order to navigate a confined waterway, even in inclement weather or after dark. Despite the polarization diversity offered by such a radar target, depolarization allows significant cross-polar clutter to obscure the reflector return. The objective of the thesis is to successfully demonstrate the enhancement and detection of a cooperative cross-polar target.

A field experiment is designed in Hamilton Bay, and 28 scans of real-time non-coherent HH-pol and HV-pol radar video recorded in a digital format from atop the Canadian Centre for Inland Waters, in Burlington, Ontario. The two reflectors are located at sites in the Dofasco area and the La Salle Park area. A conventional cell-averaging CFAR processor is initially used to give a benchmark against which to compare joint signal processing methods. A dimensionless normalized target-to-clutter ratio (NTCR) is introduced to quantify performance, along with standard sub-images to subjectively show the effect of the processing.

An adaptive cross-polar interference canceller is designed which processes the dual-polarization channels jointly, reducing the nonstationary clutter variance and enhancing the target. An analog implementation of the processor was granted Canadian and U.S. patents.

In another approach, mutual information based unsupervised learning of linear and nonlinear networks is investigated. The RBF network is shown to greatly enhance cross-polar reflector response in the non-Gaussian statistical environment.

Next, a modular solution integrates all three methods to produce superior reflector enhancement in average and peak clutter.

Finally, a novel post-detection processor is demonstrated that successfully uses *a priori* information about the reflector location along the water-land boundary of the waterway. A fuzzy processor combines primary detection information with the output from a vision-based edge detector to effectively remove false alarms.



# Acknowledgements

I would like to sincerely thank my supervisor, Dr. Simon Haykin, for all his helpful suggestions, support, and encouragement over the years. I would also like to thank the members of my advisory committee, Dr. D.W. Capson and Dr. W.F.S. Pohlman, for their helpful comments and advice. I am indebted to Arunas Macikunas, Bob Cho and Wolfgang Stehwein for their assistance with the field experiment, and for many helpful suggestions. I'd also like to extend thanks to Ed Lewis of the Canadian Centre for Inland Waters, Burlington, Ontario, for providing a location for the radar experiment, and support. To all the researchers and staff of the Communications Research Laboratory with whom I've had the opportunity to have many interesting discussions, a hearty thank-you. Finally, the financial support of the National Sciences and Engineering Research Council (NSERC) of Canada, the Ontario Government (OGS scholarship), and the Electrical Engineering department of McMaster University is acknowledged and greatly appreciated. Last but not least, I'd like to thank my parents who patiently supported and encouraged me throughout my studies.





# Contents

<b>Abstract</b>	<b>iii</b>
<b>Acknowledgements</b>	<b>v</b>
<b>1 Introduction</b>	<b>1</b>
1.1 Precise navigation problem . . . . .	1
1.2 Polarimetric reflector . . . . .	3
1.3 Signal processing issues . . . . .	5
1.3.1 Related previous work . . . . .	7
1.4 Solutions pursued . . . . .	8
1.5 Organization of the thesis . . . . .	9
<b>2 Radar experiment</b>	<b>11</b>
2.1 Design of the experiment . . . . .	11
2.2 System description . . . . .	14
2.2.1 Radar system . . . . .	14
2.2.2 Data acquisition . . . . .	17
2.2.3 Data recovery . . . . .	17
2.3 Preliminary data processing . . . . .	17
2.3.1 System calibration . . . . .	17
2.3.2 Radar range normalization . . . . .	17
2.3.3 Example images . . . . .	20
2.4 Traditional processing . . . . .	20
2.4.1 CFAR processing . . . . .	25
2.5 Summary . . . . .	30
<b>3 Adaptive cross-polar interference canceller</b>	<b>31</b>
3.1 Principle of adaptive interference cancellation . . . . .	31
3.2 Discrete-time adaptation algorithms . . . . .	32
3.2.1 The LMS algorithm . . . . .	32
3.2.2 The RLS algorithm . . . . .	33
3.2.3 Adaptive canceller performance . . . . .	35
3.3 Discussion of results . . . . .	38

3.4	Analog implementation . . . . .	38
3.4.1	Continuous-time adaptation algorithm . . . . .	39
3.5	Summary . . . . .	42
4	Mutual information networks . . . . .	43
4.1	Information-theoretic principles . . . . .	43
4.2	Unsupervised learning of neural networks . . . . .	45
4.2.1	Linear network . . . . .	45
4.2.2	Radial basis function neural network . . . . .	47
4.3	Experimental results . . . . .	52
4.3.1	Linear network . . . . .	52
4.3.2	The RBF network . . . . .	55
4.4	Summary . . . . .	60
5	Modular neural network . . . . .	63
5.1	Network design . . . . .	63
5.2	Experimental results . . . . .	64
5.3	Summary and discussion . . . . .	70
6	Post-detection processing . . . . .	73
6.1	Motivation for post-detection processing . . . . .	73
6.2	Description of the approach . . . . .	73
6.2.1	The CARTOON algorithm . . . . .	75
6.2.2	Fuzzy detection processing . . . . .	77
6.3	Example of post-detection processing . . . . .	77
6.4	Implementational issues . . . . .	83
6.5	Summary . . . . .	83
7	Conclusions . . . . .	85
7.1	Summary of results . . . . .	85
7.2	Contributions of the thesis . . . . .	86
A	PRAN system specifications . . . . .	89
A.1	Radar system . . . . .	89
A.2	Sampling system . . . . .	90
B	Calibration of radar system . . . . .	91
B.1	Radar receiver modeling . . . . .	91
B.2	Sampling system modeling . . . . .	95
B.2.1	Resultant calibration curve . . . . .	95
C	Confidence of the estimator . . . . .	99
	Bibliography . . . . .	100

# List of Tables

2.1	Experimental parameters of the radar reflectors. . . . .	11
2.2	Estimated parameters of unprocessed HV-pol sub-images. . . . .	20
2.3	Estimated parameters for CA-CFAR processed HV-pol sub-images. . . . .	26
3.1	TCR estimate for ACPIC / CA-CFAR processed sub-images. . . . .	38
4.1	Estimated parameters of linear network processed sub-images. . . . .	55
4.2	Estimated parameters of RBF network processed sub-images. . . . .	57
5.1	Estimated parameters of modular network processed sub-images. . . . .	64
7.1	Summary of NTCR performance of signal processors. . . . .	85
B.1	Parameter estimates for behavioural model of radar receiver. . . . .	91
B.2	Parameter estimates for linear model of the sampling system. . . . .	92
B.3	Look-up table relating digital values to input power in dBm. . . . .	96



7 x

=

# List of Figures

1.1	An artist's depiction of the polarimetric radar navigation system in operation. From cover of [9]. . . . .	2
1.2	The trihedral twist-grid reflector [44]. . . . .	4
1.3	The signal processing and detection system. . . . .	8
2.1	Map showing the location of the radar and reflectors used for the experiment.	12
2.2	Antenna's viewpoint, assembled from three wide-angle photos. . . . .	13
2.3	Diagram of the dual-polar non-coherent radar receiver. . . . .	14
2.4	Experimental radar setup. . . . .	15
2.5	Experimental data acquisition setup. . . . .	15
2.6	Block diagram of the experimental data acquisition setup. . . . .	16
2.7	Block diagram of the experimental data recovery setup. . . . .	16
2.8	Simple trigonometric model of the radar's height-range plane. . . . .	18
2.9	PPI images of HH-pol and HV-pol digitized video of the bay area. . . . .	19
2.10	The HH-pol sub-images of interest. . . . .	21
2.11	The HV-pol sub-images with the locations of the reflectors marked. . . . .	22
2.12	The target and clutter densities and the associated parameters used in calculating the normalized TCR figure of merit. . . . .	23
2.13	Estimated histograms of peak target and average clutter of unprocessed data.	24
2.14	Representative patches of HV-pol clutter from the corresponding Dofasco and La Salle Park areas. . . . .	25
2.15	Target and clutter masks used in CFAR processing. . . . .	26
2.16	Sub-images of the CFAR processing, prior to detection. . . . .	27
2.17	Estimated histograms of peak target and average clutter for CA-CFAR processed result. . . . .	28
3.1	Discrete time cross-polar interference canceller . . . . .	32
3.2	Ideal cancellation performance. . . . .	35
3.3	Sub-images of ACPIC processed data. . . . .	36
3.4	Estimated histograms of peak target and average clutter for ACPIC result.	37
3.5	Continuous time cross-polar interference canceller. . . . .	39
3.6	Block diagram of analog implementation. . . . .	40
3.7	Schematic of analog cross-polar interference canceller. From the U.S. patent [26]. . . . .	41

4.1	Linear neural network architecture. . . . .	45
4.2	The radial basis function neural network architecture. . . . .	47
4.3	Scatter plot of the output of the linear network. . . . .	52
4.4	Sub-images of linear network processed data. . . . .	53
4.5	Estimated histograms of peak target and average clutter for linear network result. . . . .	54
4.6	Scatter plot of training data. The components of the estimated mixture densities are superimposed. . . . .	56
4.7	Scatter plot of output of RBF network. . . . .	56
4.8	Surface plot of nonlinear transformation learned by the RBF network. . . .	57
4.9	Sub-images of the RBF network processed data. . . . .	58
4.10	Estimated histograms of peak target and average clutter for RBF network result. . . . .	59
5.1	Modular neural network. . . . .	64
5.2	Sub-images of modular network processed data. . . . .	65
5.3	Estimated histograms of peak target and average clutter of the modular network processed data. . . . .	66
5.4	Estimated receiver operation curves for the adaptive interference canceller network output. . . . .	67
5.5	Estimated receiver operation curves for RBF network output. . . . .	68
5.6	Estimated receiver operation curves for modular network result. . . . .	69
6.1	Block diagram of post-detection processing. . . . .	74
6.2	Block diagram of the CARTOON algorithm. . . . .	76
6.3	Binary edge maps produced by the CARTOON algorithm. . . . .	78
6.4	Result after radially processed first edge detection. . . . .	79
6.5	Gaussian measurement function applied to detections. . . . .	80
6.6	Gaussian measurement function applied to edges. . . . .	81
6.7	Final post-detection result. The original HH-pol image is superimposed as a visual aid. . . . .	82
B.1	(a) Block diagram of signal path in the system. (b) Radar receiver calibration. (c) Sampling system calibration. . . . .	92
B.2	Measured radar receiver calibration data. . . . .	93
B.3	Behavioural model fitted to measured radar characteristics. . . . .	93
B.4	Digitized sine waves used to calibrate gain. . . . .	94
B.5	Radar receiver calibration curve. . . . .	94

# Chapter 1

## Introduction

### 1.1 Precise navigation problem

Inland confined waterways, such as the St. Lawrence seaway and the Mississippi River, are of great importance in the transportation of goods by ship. The shipping community strongly desires to make best use of this resource. However, some factors exist that limit the time that the waterways may be used. During periods of low visibility, namely fog, heavy rain, or darkness, the ships cannot navigate by visual aids. The buoys which are used as visual aids in navigation are deployed at the beginning of the shipping season, and removed at the end of the season. To extend the season beyond the times when buoys are available, and to travel in times of poor visibility, another navigational aid is needed to supplant, or replace that of visual navigation by the ship's pilot. It goes without saying that such a system must be robust and provide an accuracy of navigation comparable to that of the ship's pilot. It was judged that a ship's pilot could navigate visually within an accuracy of approximately  $\pm 3$  meters from the channel centreline and  $\pm 7$  meters from the channel limits [12].

One of the conventional solutions is to use microwave transponders. The transponders are placed into the environment at surveyed locations, and the ship is equipped with the proper transmission and receiver equipment to interrogate the transponders, along with an automated navigational computer. A ship traveling the waterway would periodically transmit a coded RF signal, which would cause a local transponder to transmit back to the ship a known signal on differing RF carrier frequency. The navigational computer can then translate the measured delays into ranges to the transponders, and thus use triangulation to locate the ship within the waterway. The disadvantages of such a system are that the transponders are relatively complex, expensive, and considered a high maintenance item. Since the transponders are active, their batteries must be replaced regularly. Other navigational systems such as Loran-C, differential Loran-C, and Navstar GPS are also possible candidate solutions. These systems, however, are currently limited in their accuracy, which ranges from  $\pm 15$  meters to  $\pm 50$  meters. These accuracies do not meet the abilities of the ship's pilot and hence are deemed not satisfactory.

Rather than using transponders, the use of a marine radar system was investigated as

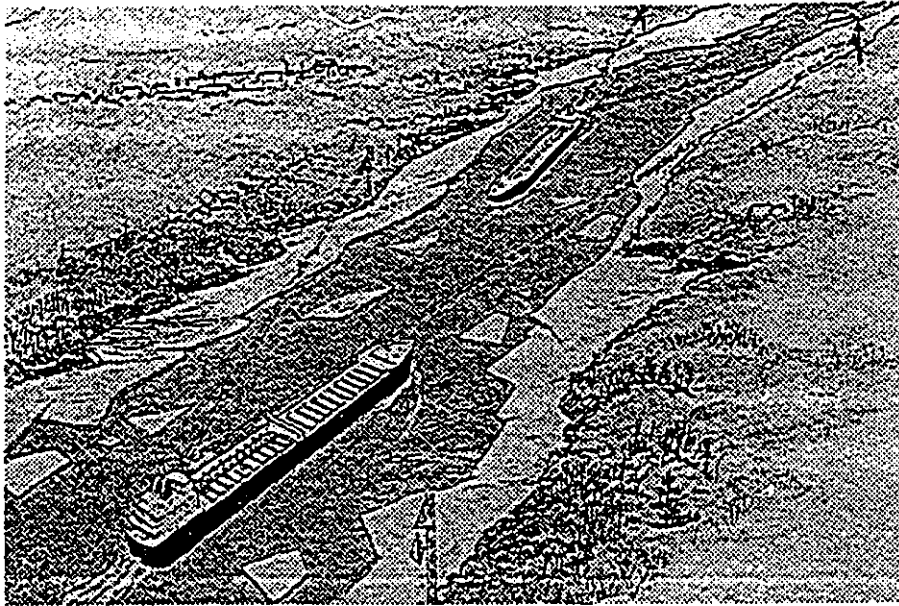


Figure 1.1: An artist's depiction of the polarimetric radar navigation system in operation. From cover of [9].

a means by which radar ranging to known targets could effect the same operation as a microwave transponder. The discriminants that are available to the radar systems designer for the identification of stationary targets are power, frequency, and polarization. Doppler processing is not applicable since reflector targets are generally fixed, and do not have a velocity component relative to the background clutter. Other forms of coherent processing are not considered since the complexity and cost of such a system would make it impractical to the shipping community. The marine radar (e.g. Decca 1229) which most ships are already fitted with is non-coherent, making use of a cheap X-band magnetron as the high-power RF transmitter. Preliminary investigations demonstrated that it was not possible to reliably detect common trihedral reflectors using a typical marine radar system since the reflectors were obscured by land clutter, and affected by multipath attenuation. To make the returns from the reflectors greater, the size of the trihedral would have to be greatly increased, making them impractically large. The use of frequency diversity is possible if the reflector is designed with a nonlinear transfer function which would then return generated harmonics that could be received. This idea is also dismissed since a great deal of power would be needed to be transmitted to operate a nonlinear device (e.g. diode) in the reflector.

This leaves polarimetric diversity. The polarization of an electromagnetic wave is defined as the direction of the electric field component. Most marine radars transmit with the electric field linearly polarized in the horizontal plane. A passive reflector target which is able to rotate the plane of polarization efficiently is obviously needed. It is known that a



dihedral reflector mounted on a 45 degree angle from the horizontal has the desirable property of rotating a linearly polarized field through 90 degrees efficiently. Early studies [20] showed that the dihedral exhibited the polarimetric characteristics that could be exploited in navigation. Unfortunately, the dihedral only exhibits its polarization rotating property over a very narrow azimuthal angle. Further investigations of reflector design resulted in the invention of the trihedral twist-grid reflector, which has the same polarization characteristics as the dihedral as well as a wide azimuthal response [42, 43]. Using the reflector in field experiments verified its desirable performance characteristics [4].

The novel polarimetric radar for accurate navigation (PRAN) system was thus invented at the Communication Research Laboratory. The system consists of a set of polarization-twisting reflectors situated along a confined waterway in known locations so that a ship with the proper radar equipment can ascertain its position with respect to the shoreline. Figure 1.1 shows a possible deployment of the system along a confined waterway. An experimental proof-of-concept site was setup in the Hamilton Bay to study an operational system in a setting which provided varying clutter backgrounds. A typical non-coherent marine radar transceiver was retrofitted with a dual-polarized antenna, a dual-polar rotating joint, and a second radar receiver section in order to receive the vertically polarized returns. The radar is configured to transmit horizontally polarized energy, and receive both linear orthogonal polarization channels; the conventional horizontally polarized returns as well as the vertically polarized returns, the latter containing the desired twist-grid reflector response, are the resultants. The received log video signals then go on to signal processing stages and plan position indicator (PPI) displays. In an operational system an automatic detection processor would detect the targets (and false alarms!), and pass on the locations of the detections to the tracking algorithm. The reflector target detections are input on a scan-by-scan basis. The tracking algorithm uses the current and past information to locate the ships' position on an electronic chart. The unique issues involved in the ship tracking problem were addressed in the thesis by Lee [36]. In experimental trials using a circular polarized radar to detect the trihedral twist-grid reflectors it was verified that a repeatable accuracy of better than  $\pm 3$  m could be achieved [47]. The system has been commercialized by Offshore Systems Limited, of Vancouver, BC and named RANAV.

The interested reader is referred to Haykin [21] which gives a complete historical perspective on the development of the PRAN system.

## 1.2 Polarimetric reflector

As already mentioned, the trihedral twist-grid reflector has the special property of efficiently converting horizontally polarized radar transmissions to vertically polarized returns. Figure 1.2 shows a diagram of the reflector, with the horizontally polarized incident electric field being converted to the vertically polarized plane.

The design and operational characteristics of the twist-grid retrodirective reflectors is described in detail by Macikunas [42, 43, 44, 41]. The normal trihedral reflector operates on a multiple-bounce principle, reflecting the incident electromagnetic wave from its metal surface back towards its source, as suggested by Fig. 1.2. This gives the trihedral reflector a

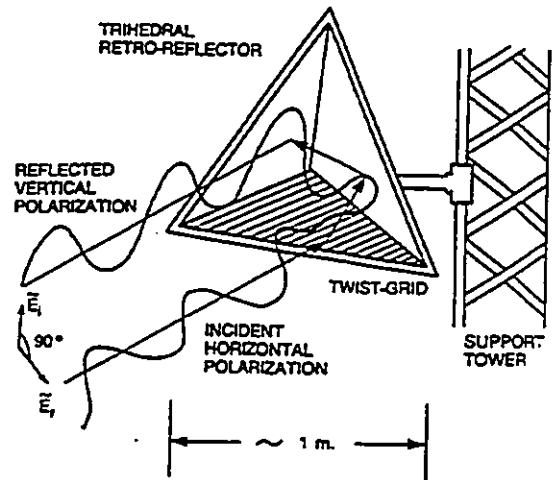


Figure 1.2: The trihedral twist-grid reflector [44].

high radar cross section (RCS) relative to a flat plate reflector, for example. The unmodified trihedral does not perform any polarization rotation. To achieve the desirable rotation property a wire grid was added to one of the faces of the reflector, creating a hybrid of microwave devices, namely the trihedral and the wire grid. As is well-known, a grid of wires in the x-y plane oriented at 45 degrees will rotate an incident wave traveling along the z-axis with its electric field in x-z (or y-z) plane by 90 degrees. The spacing of the wires is dependent on the frequency of operation. Using the necessary geometric coordinate transforms, the orientation of the wires on the bottom face of the reflector is found. The geometrical analysis further specifies that the cross-polar performance is optimum when the trihedral reflector is mounted with the bottom face rotated 15 degrees counterclockwise from horizontal, and tilted down 35 degrees from vertical. The wires are mounted in a dielectric substrate, such as Styrofoam, that operates as a necessary spacer between the wire grid and the metal face of the bottom trihedral panel. The spacer width turns out to be a critical parameter. If chosen incorrectly, destructive interference between the wires and the metal reflector can result. The hybrid design shows excellent azimuthal response, maintaining a 10 dB cross-to-like polarized response over a 43.6 degree azimuthal angle. The design also shows high efficiency: a cross-polarized echo level which is no more than 1 dB below a like-polarized echo of a normal trihedral reference target.

Summarizing the important properties of a trihedral twist-grid reflector:

- passive device;
- efficient rotation of polarization;
- high cross-polar radar cross section;
- wide azimuthal angular response;

- low cost and simple construction;
- insensitive to alignment errors;
- robust.

The twist-grid reflectors have wide angular response, but it is recognized that a constellation of reflectors may be needed for coverage of an area with a wide angular response requirement. Also, although the reflectors are robust in operation, a configuration of redundant trihedrals may be required to overcome multipath problems, as well as failure due to physical reasons (e.g. damaged by weather).

Limitations in the marine radar system components, as well as multipath and the natural depolarization characteristics of the environment increase the clutter in the received radar returns and make the reflectors less visible than is desirable. Several possible approaches may be taken to make the trihedral twist-grid reflector more visible. An obvious solution is to make the twist-grid reflectors larger, hence making the radar cross section (RCS) of the targets larger and thereby increasing the target-to-clutter ratio. This may solve the problem, but larger reflectors would increase the cost of manufacturing and installing such a system in proportion to the number of reflectors needed for navigating the waterway. Another possible solution is to increase the quality of the radar system components. This is also an expensive proposition and is subject to diminishing returns. The incremental improvements in performance come at an increasingly higher cost. The third possible solution and the one discussed herein, involves processing the horizontally and vertically polarized returns jointly in an optimum fashion to increase the target-to-clutter ratio.

### 1.3 Signal processing issues

In the case of an ideal radar system operating in an environment where there is little cross-polarized response in the radar returns except from the twist-grid reflector, the plan position indicator (PPI) display of the vertical polarized channel would be expected to show a single range cell indicating the position of the reflector, and a background clutter level at least 10 dB below the target. The experimental system, however, does show significant clutter returns on the vertically polarized channel, although they are reduced in power compared to that on the horizontally polarized channel. The increase of energy on the vertically polarized channel could occur as a result of degraded cross-polarized (cross-polar) performance in the antenna or rotary joint, as well as a result of depolarization of the H-pol (horizontally polarized) transmission due to the clutter. The manufacturer's specifications given in Appendix A indicate the channel separation of the rotary joint to be 50 dB, and the cross-polar discrimination of the antenna to be greater than 25 dB. The trihedral twist-grid reflectors are quoted [44] as having a like-polarized (like-polar) rejection of 16-24 dB. These system imperfections would account for a portion of the observed clutter, but would not account for regions with a response greater than that of the trihedral twist-grid reflector. Assuming that these components are operating within specification, it is concluded that the relatively large power response received from the clutter range cells on the V-pol (vertical polarized) channel occurs due to depolarization.

The phenomenon which causes a received wave to have a different polarization from the transmitted wave is called depolarization. The radar environment generally consists of targets, land clutter, and sea clutter whose back-scatter has different polarization properties. For example, a target may consist of various asymmetric objects with partially conductive surfaces, and this can cause varying polarization qualities. Diffuse scattering is the main cause for depolarization in land and sea clutter, although man-made objects can cause small regions to have significant depolarization values. Due to the physical non-homogeneous nature of various clutter regions, we therefore expect the depolarization values to vary over some range. Cross-polar returns for land clutter are quoted to be typically in the range of 3-10 dB less than the corresponding co-polar returns for linearly polarized X-band radar [16]. The corresponding range for sea clutter is 6-10 dB.

The polarization scattering matrix (PSM) describes the interaction that takes place between an electromagnetic wave and the target or clutter. The polarized electric field can be represented by the complex vector [45]

$$e(t, z) = \begin{bmatrix} e_H(t, z) \\ e_V(t, z) \end{bmatrix} = h \exp[j(\omega t - kz)] = \begin{bmatrix} |e_H| \\ |e_V| e^{j\delta} \end{bmatrix} e^{j\delta_H}, \quad (1.1)$$

where  $e_H(t, z)$  is the complex electric field component in the horizontally polarized direction,  $e_V(t, z)$  is likewise the vertically polarized component,  $h$  is the complex wave polarization,  $\omega$  is the angular frequency,  $k$  is the propagation constant, and  $\delta = \delta_V - \delta_H$  is the electrical phase difference between H and V electric field components. The x-direction is designated the horizontal polarized component, the y-direction the vertically polarized component, and the z-direction is the direction of propagation of the wave. Assuming a linear polarization basis, the scattering matrix may be written as [45]

$$S(H, V) = \begin{bmatrix} |S_{HH}| \exp(j\theta_{HH}) & |S_{VH}| \exp(j\theta_{VH}) \\ |S_{HV}| \exp(j\theta_{HV}) & |S_{VV}| \exp(j\theta_{VV}) \end{bmatrix}, \quad (1.2)$$

where  $|S_{HH}|$  denotes the amplitude of the H-pol transmitted and H-pol received component,  $\theta_{HH}$  is the corresponding phase, and likewise for the rest of the parameters. The scattered wave polarization is therefore

$$h_s = S(H, V) \cdot h_T, \quad (1.3)$$

where  $h_T$  is the transmitted wave polarization. For the problem at hand, the transmitter produces only H-pol signals, and the receives both H-pol and V-pol scattered energy non-coherently. This implies that the information available at the output of the radar receiver is limited to estimates of the amplitude terms  $|S_{HH}|$  and  $|S_{HV}|$ .

The inland waterway scene is one of inhomogeneous clutter, with sea and land clutter, as well as strong returns from undesirable point targets. The envelope of the radar receiver output is often approximated by the Rayleigh distribution [62]. Land and sea clutter deviate from this assumption, especially at higher resolutions. Often the land clutter can be described by the log-normal or more accurately by the Weibull probability density function

for various terrain or sea states [18]. In any case, in general the clutter can be characterized as having a non-stationary and non-Gaussian probability density function. The signal processing solution must therefore address this important fact.

There is *a priori* information that an engineer can use to improve the visibility and hence detection of the target. The targets are cooperative retrodirective reflectors with the polarization rotating properties already discussed above. The location of the targets is controlled by the installers of the system, so the placing of the target adjacent to a stationary undesirable point target with a large cross-polar response can be avoided. This can be verified by first surveying the proposed installation area with an operational PRAN radar system. The path from the ship's radar antenna to the reflector target must also be un-obscured by natural objects (e.g. trees) or artificial objects (e.g. metal towers). The preferred location for these targets is therefore near the boundary between land and water. Since it is desired that a detection be performed on a per scan basis, no scan-to-scan integration is used to improve performance. The tracking algorithm, however, can perform the integration between scans and thus further improve detection. The momentum and maximum maneuvering speed of the ships along with the scan period (typically 2 sec) limit the relative displacement of the target between scans. A good design should incorporate this available *a priori* information to maximize performance of the system.

### 1.3.1 Related previous work

There have been various attempts at using polarization diversity to improve detection performance, and some of the approaches that reflect on the problem of interest are briefly described herein. When making use of diversity to gain an improvement in performance, there is a question of how to combine information available in the returns in order to come up with a sufficient statistic for a detection strategy.

In a research study done at CRL, Lewis et al. [37] showed that horizontal like- and cross-polarized RCS measurements had a significant variation that could be used as a discriminant for ice. Orlando et al. [56] made use of this observation and demonstrated that ice classification performance increased when the cross-polar channel information was added.

In [38], Long suggests the use of the ratio of horizontal and vertical like polar returns as the sufficient statistic. He observes that when transmitting both horizontal and vertical linear polarizations and receiving like polarizations, the ratio of received target RCS is approximately unity for simple targets, such as corner reflectors or flat plates, and that the ratio varies more widely for other forms of clutter, such as sea clutter. This approach seems to be effective in suppressing sea spikes, as well as interference from other radars.

Similarly, Dunn [11] observes that box-like targets typically contain diplanes and therefore are more likely to have a significant cross-polar return. He proposes a technique that subtracts a fixed portion of the like-polar return from the cross-polar return, and registers a target detection only if the result exceeds a threshold. This is a simple type of fixed weight canceller with a hard limiter on the output.

Nathanson [51] proposes an adaptive solution referred to as an adaptive polarization

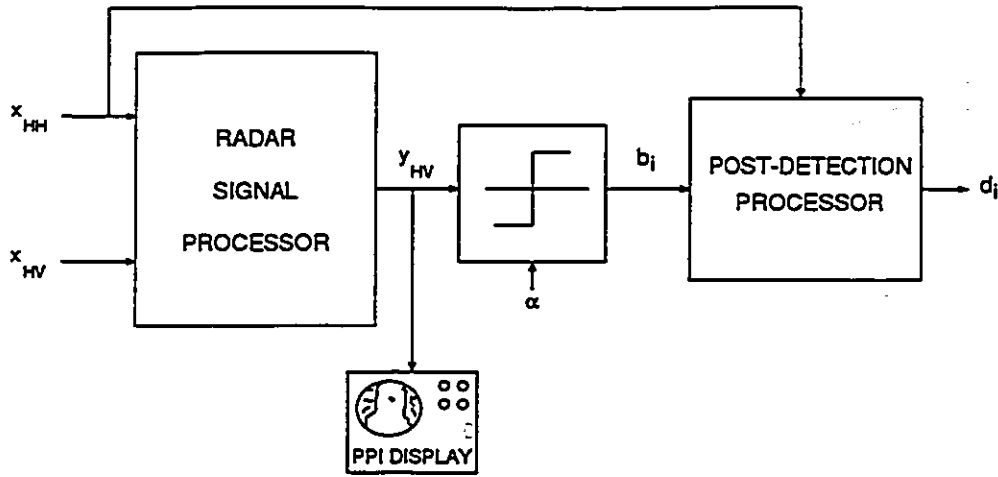


Figure 1.3: The signal processing and detection system.

canceller (APC) for clutter suppression in coherent circularly polarized radars. The circuit enhances the like-polarized channel by using the cross-polarized channel as an independent measure of the rain clutter return.

Further investigation of the adaptive filter approach has been done by Giuli et al. [7] in the context of a circular polarized radar system operating in rain clutter. Using computer simulated data it is shown that an adaptive polarization canceller output, averaged over independent trials, would improve the probability of detecting a fluctuating target by approximately 9 dB.

An extension of this work by Giuli et al. [17] is the symmetrical adaptive polarization canceller (SAPC) designed to suppress jamming interference. Two symmetric cancellers operating on both polarization channels simultaneously achieve a high degree of suppression under the conditions that the jammer is highly polarized and at a significantly different polarization from the desired target. A comprehensive summary of adaptive polarization processing is provided by Giuli [16].

## 1.4 Solutions pursued

The main aim in this thesis is the successful signal processing of the received cross-polar data in order to enhance the reflector targets, making them more visible to the human operator, and simultaneously improving the automatic detection performance. Figure 1.3 is a block diagram of the signal processing and detection system.

The radar signal processor accepts video data,  $x_{HH}$  and  $x_{HV}$  from the logarithmic-response non-coherent radar receiver and processes the HH-pol and HV-pol data in an optimum fashion. The signal processor should make use of adaptive and non-linear elements to address the non-stationary and non-Gaussian nature of the inhomogeneous clutter

environment. One element of the solution is an adaptive cross-polar interference canceller, designed to cope with varying clutter regions. Another element is the nonlinear radial basis function (RBF) network that is trained using a mutual information principle in order to capture the non-Gaussian nature of the clutter. These two elements perform well, but have different desirable characteristics that beg to be combined. A non-learning modular network is investigated as a possible architecture for incorporating sub-networks together with the objective of maximum information preservation.

To reduce the clutter a conventional cell-average constant false alarm rate (CA-CFAR) processor is also investigated. The enhanced image produced by the method (prior to thresholding) has the property of a constant false alarm rate. The CA-CFAR process is used as a benchmark against which other methods are judged. The resultant processed image,  $y_{HV}$ , may then be displayed on a plan position indicator (PPI) display alongside a conventional HH-pol PPI display that is normally used by the operator.

For automatic detection, the image is passed onto the threshold unit. The thresholding stage maps the continuous image to a binary image,  $b_i$ . The parameter  $\alpha$  sets the threshold and thus determines the false alarm rate. Finally, a post-detection processor is designed that uses *a priori* information about the waterway to remove false targets. Modern image processing techniques based on human vision are used to determine the land-water boundary. The fuzzy processor only accepts detections that occur in and around such a boundary, and rejects all other detections as false alarms. The final detected output,  $d_i$ , contains the desired reflector locations.

Throughout the processing stages an effort is made to consider solutions which are implementable in analog neural network architectures. Some of the currently available VLSI architectures are discussed by Haykin [25]. Only simple elements need to be considered for use in the neural network architecture, namely: delays, weights (both fixed and adaptive), multipliers, integrators, summers, threshold units, and Gaussian response units. Using these basic elements, structures such as adaptive filters, automatic gain controls, and fuzzy logic functions can be constructed.

## 1.5 Organization of the thesis

The thesis is organized as follows. The radar field experiment at the Canadian Centre for Inland Waters (CCIW) is explained in detail in Chapter 2. It is the data base collected in this experiment that is used throughout to test the various processing methods. As a benchmark, the cell-averaging constant false alarm rate (CA-CFAR) process is introduced and the results calculated for the HV-pol received data. Sub-images containing the target are chosen. Measures are defined that are used to evaluate the successfulness of the reflector enhancement for the various methods. Clutter and target statistics are collected over the 28 available scans.

Chapter 3 details the adaptive cross-polar interference canceller, its learning algorithms and operational characteristics. An analog hardware implementation of the canceller for enhancing cross-polarized target returns was granted Canadian and U.S. patents. Digital simulations are used to evaluate system performance under varying clutter environments.

In order to deal with the non-linear nature of the clutter distributions, neural networks based on minimizing mutual information between the outputs are developed and described in Chapter 4. The networks are trained off-line, and therefore are non-adaptive when operating. A linear network and a non-linear network based on the radial basis function (RBF) neural network are evaluated. New unsupervised training methods are employed to learn the parameters in the RBF networks.

It is generally recognized that it is easier to solve subproblems, and then integrate the results for a complete solution. This philosophy, discussed in Chapter 5, leads to robust modular network designs that integrate the best characteristics of the sub-networks. The adaptive canceller and RBF networks are thus combined into a modular network that should demonstrate the desirable properties of both designs.

Finally, the post-detection problem is tackled. At this stage *a priori* information is introduced to eliminate residual false alarms. The desirable locations for the twist-grid reflector is along the land-water boundary. A modern edge-detection algorithm (based on vision research) is adapted for use in the radar environment. Fuzzy set reasoning is used to combine the primary detections with the land-water boundary information to remove obvious false alarms. The operation is demonstrated using a sample situation.

The thesis is concluded in Chapter 7 with some final remarks on the subject.



## Chapter 2

# Radar experiment

In this chapter the radar experiment is presented, along with the introduction of some traditional processing techniques. The discussion includes sections on the overall design of the experiment, the location of the reflectors, the calibration of the radar system, and the digital acquisition of the data that are used throughout the study. Returning from the field experiment to the laboratory, the focus is on the retrieval and preprocessing of the data. Finally, conventional radar processing results are presented as a benchmark to compare with further processing. Example radar images are presented to subjectively judge the various stages of processing.

### 2.1 Design of the experiment

Retrodirective twist-grid reflectors were installed at two sites in the Hamilton Bay, as shown in Fig. 2.1, demarcated by triangular markers ( $\Delta$ ) along the shoreline. These reflectors are referred to by their locations, namely the Dofasco site (the property belongs to the Dofasco steel company), and the La Salle Park site (the location was on the border of the La Salle Park conservation area, in Burlington, Ontario). The Dofasco site, on the Hamilton side of the Bay, represents a harsh industrial setting in the sense that there are many large clutter returns from this area. The La Salle Park site is in a location with milder land clutter; a

	Dofasco	La Salle Park
Range to reflector	2300 m	3100 m
Number of reflectors	2	1
RCS of reflector	4846 sq. m	458 sq. m
Reflector cell size (range)	7.5 m	7.5 m
Reflector cell size (azimuth)	2.7 m	4.0 m

Table 2.1: Experimental parameters of the radar reflectors.





Figure 2.2: Antenna's viewpoint, assembled from three wide-angle photos.

park-like setting mixed with residential units. The polarimetric radar was located on the rooftop of the Canadian Centre for Inland Waters (CCIW) in Burlington, Ontario. This location is marked by a plus (+) symbol on the topographic map. The composite photo in Fig. 2.2 gives the "antenna's eye-view" of the bay area of interest.

The reflectors were attached to poles, approximately 2-3 meters above water level, and their angular position adjusted to provide a maximum cross-polar response on the HV-pol channel of the radar receiver. For details on the operation and proper installation of the twist-grid trihedral radar reflector, see Macikunas and Haykin [42]. Table 2.1 summarizes the experimental setup. The radar cross-section (RCS) given is the value theoretically calculated from the physical dimensions of the reflector. The given radar cell size values are calculated from the physical parameters of the radar, as summarized in Appendix A. These predicted values agree with the experimental measurements done in the field.

Over an extended period of operation, it was observed that the received cross-polarized return power from the reflector target varied over time. This was attributed to the changes in water level and surface roughness which in turn affect signal fading caused by destructive interference between two signal paths, the direct path and the one-bounce path from target to the water surface and the antenna. The common term used in describing such a destructive interference caused by the addition of signal path differences is multipath fading. There were no attempts made to compensate for multipath fading, since under normal operating conditions the radar operator would not be able to control reflector height. If the system was to be used in a confined waterway, it may be necessary to study the effect of target reflector location and height in order to determine the distribution of installed targets which would be most robust with respect to multipath, and the variations in multipath caused by changes in water height. For example, if a particular target reflector had a reduced response power due to a multipath fading condition, it would be desirable to have another reflector in different location which was not in a multipath fading null. It is recommended that a Monte Carlo simulation of target locations, and their sensitivity to water level and surface conditions be performed. However, the location of target reflectors is primarily an

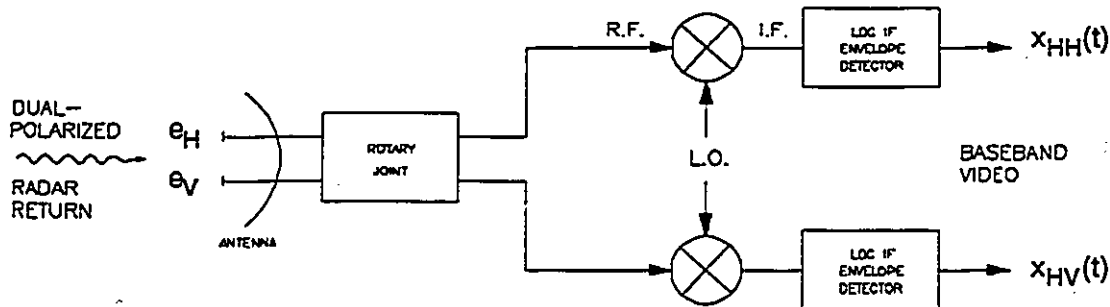


Figure 2.3: Diagram of the dual-polar non-coherent radar receiver.

implementational concern, and no further investigation is done here.

## 2.2 System description

The experimental system consists of three major hardware components: the radar system (including the reflectors), the digital data acquisition system, and the data recovery system.

### 2.2.1 Radar system

The experimental radar system was assembled at the Communications Research Laboratory (CRL), mostly from standard subsystems available commercially. The radar system components were commercially available marine radars, chosen to be representative of the radars currently used by ships. The PRAN system was originally conceived as a low cost add-on, in hopes that this would make the system financially more attractive to the marine community. The radar receivers were modified slightly to accommodate dual-channel operation, and to be able to respond to a higher dynamic range. Appendix A lists the relevant radar specifications. Fig. 2.3 shows the block diagram of the dual-polar incoherent radar receiver, with log video output for the HH-pol and HV-pol channels. The photo of the radar transceivers is shown in Fig. 2.4. The rotary joint and parabolic antenna are located directly above the radars, as suggested by the microwave waveguide feeds rising through the ceiling.

An analog PPI display was used in checking the radar's operation, but no signal processing built into the PPI display unit was used on the data prior to recording. The unadulterated raw video data from the radar's output was sent to the digital data acquisition system, along with the azimuthal position information.

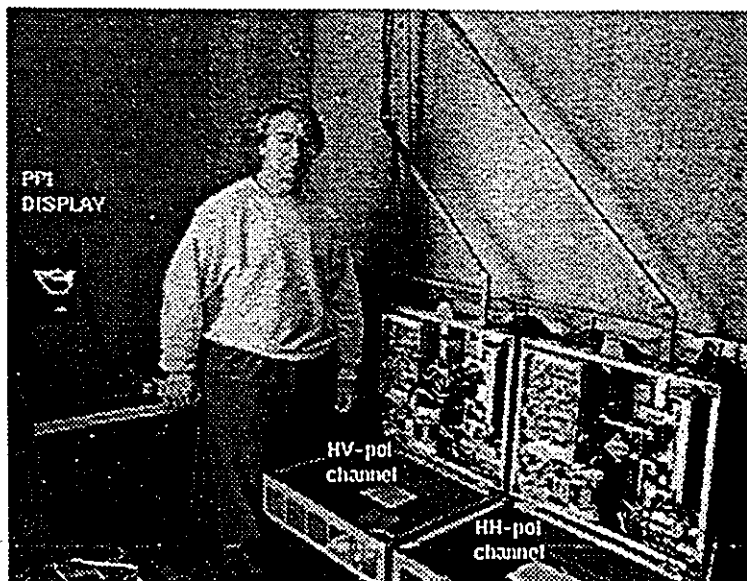


Figure 2.4: Experimental radar setup.



Figure 2.5: Experimental data acquisition setup.

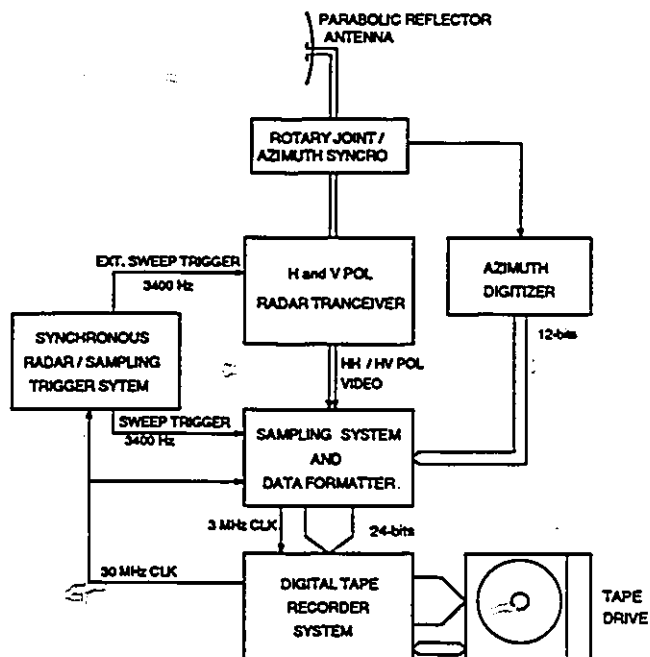


Figure 2.6: Block diagram of the experimental data acquisition setup.

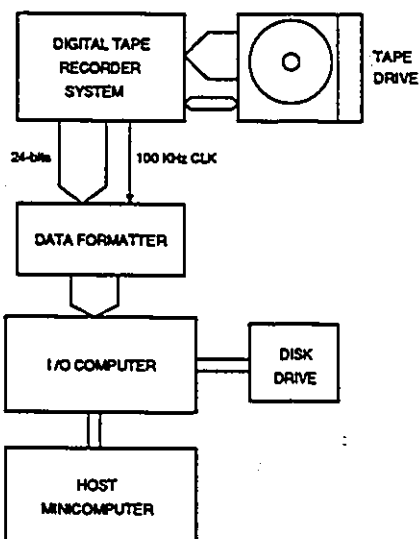


Figure 2.7: Block diagram of the experimental data recovery setup.

### 2.2.2 Data acquisition

The digital data acquisition system was assembled at CRL to record multiple radar video sweeps at a high sampling rate (30 MHz), along with azimuth and status information. A multi-channel sampling system, designed and constructed at CRL, was used to digitize the HH-pol and HV-pol analog video signals. In addition, a programmable synchronous radar and sampling system trigger system was designed and constructed to derive the necessary triggers from the master sampling clock provided by the digital tape recorder clock. The resultant digital data was formatted and recorded on a high-speed digital tape recorder. This experiment was the first successful digital format recording of live, full-scan radar video at McMaster University. Figure 2.5 is a photograph showing the digital data acquisition system in operation. The radar system is located on a stairway landing directly above.

### 2.2.3 Data recovery

After data recordings were brought back from the field, a data recovery system was set up as shown in Fig. 2.7. The data recovery system is used to play back the digital tape recordings at reduced speed. This is necessary in order for the computer system to be able to transfer the large quantities of data to memory, and then disk. The data were played back from the digital recorder into the I/O computer, which then double-buffered the data, and wrote it to a high-speed disk drive system. Many software tools were developed for the manipulation of the large data sets, including previewing, formatting and editing the raw data. After suitable scans were recovered from the tape, the formatted data were transferred to a workstation for further processing.

## 2.3 Preliminary data processing

### 2.3.1 System calibration

The digitally recorded data values are related to the signal power at the input of the radar system. Through careful calibration, the relationship between these two quantities can be measured. Appendix B describes in detail the procedure followed to determine a lookup chart, so that given a recorded digital value, the desired input signal power level is obtained in dBm.

### 2.3.2 Radar range normalization

Figure 2.8 shows a simple trigonometric model of the radar experiment in the height-range plane. The radar is located at the top of a building approximately 41.1 m above the lake water. The ranges  $R_1$  and  $R_2$  give the approximate start and end of the radar range data collected. The radar range can be determined from the time delay between the transmitted pulse and the received pulse. If  $n$  is the sample number of the sweep, with a sampling

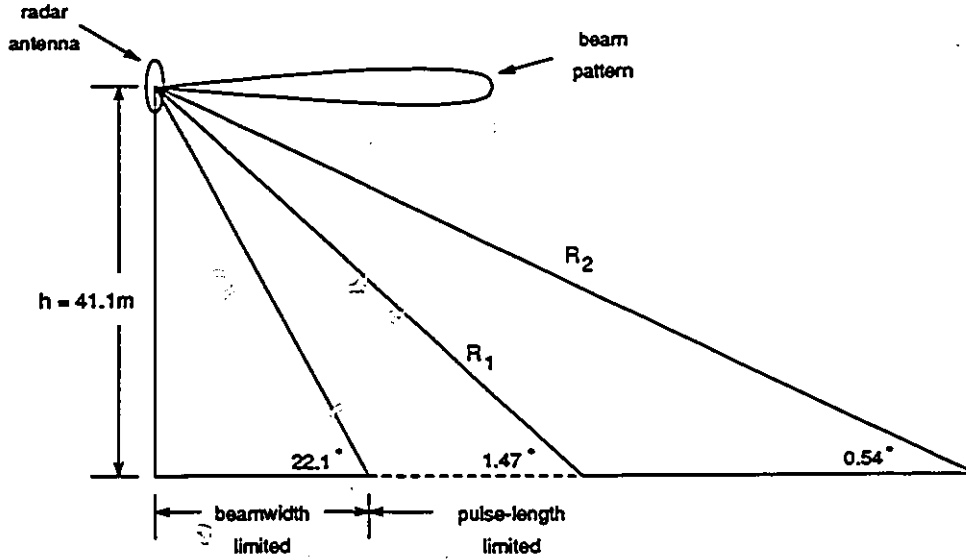


Figure 2.8: Simple trigonometric model of the radar's height-range plane.

frequency of  $f_c$  (30 MHz), the range can be determined in meters from the relationship

$$R = \frac{cT}{2} = \frac{cn}{2f_c} = 5 \cdot n \text{ (m)}, \quad (2.1)$$

where  $c$  is the speed of light ( $3 \times 10^8 \text{ m/s}$ ), and  $T$  is the measured delay time that is equal to  $n/f_c$ .

The radar range equation describes the changes in range that occur, and how they are taken into consideration. Under typical marine radar operating conditions, a sensitivity-time control (STC) circuit is used to compensate for variations in received power with range. For the purposes of this experiment, the STC circuit was disabled in the radar receiver. The compensation is applied numerically, calculated from the radar range equation.

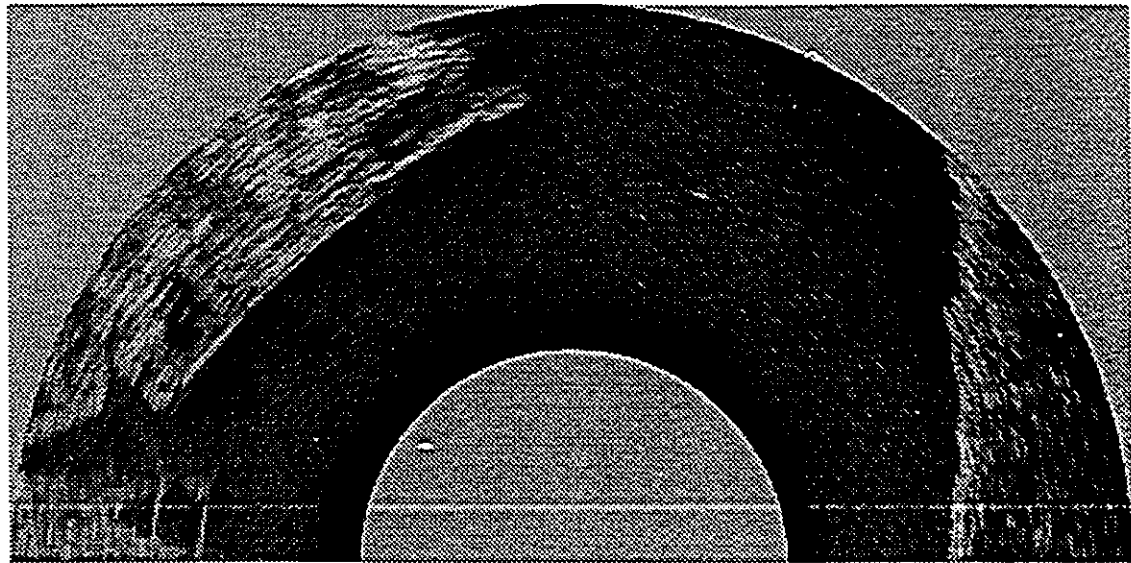
The target of interest falls in the class of a point target. The radar range equation for a point target is defined by [62]

$$P_r = P_t \frac{G_a^2 \cdot \sigma_R \cdot \lambda^2}{(4\pi)^3 \cdot R^4}, \quad (2.2)$$

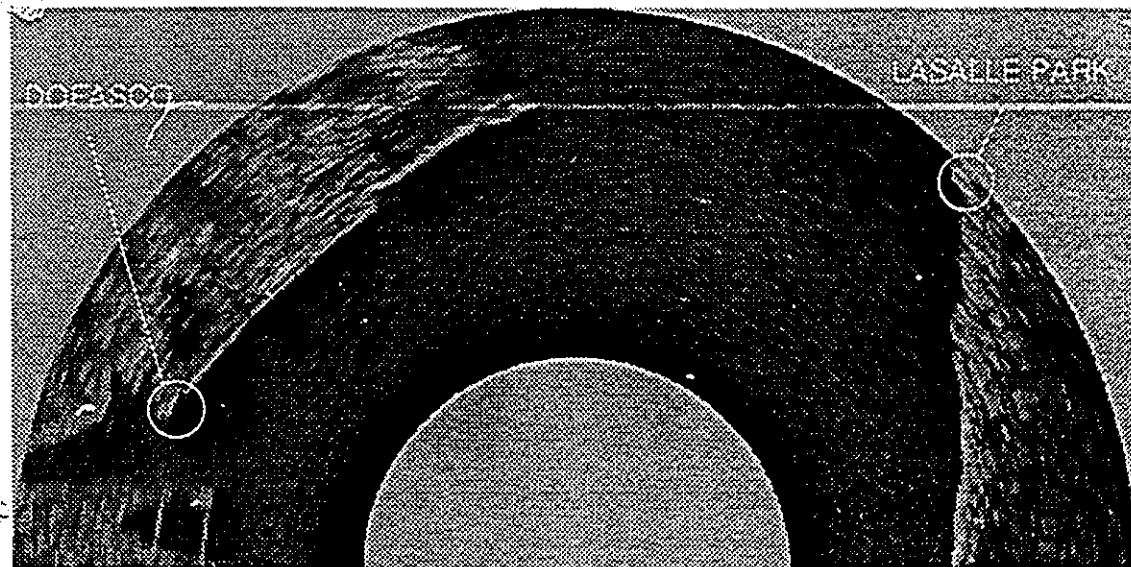
where  $P_t$  is the power transmitted,  $G_a$  is the antenna gain,  $\sigma_R$  is the radar cross section (RCS) of the target,  $\lambda$  is the wavelength of the transmitted pulse, and  $R$  is the range (in meters) to the target. The RCS of the target is the parameter of interest. Rearranging the radar range equation yields

$$\sigma_R = \frac{(4\pi)^3 \cdot R^4}{P_r \cdot P_t \cdot G_a^2 \cdot \lambda^2}. \quad (2.3)$$





HH-pol



HV-pol

Figure 2.9: PPI images of HH-pol and HV-pol digitized video of the bay area.

	Dofasco	La Salle Park
target ( $\hat{\mu}_t, \hat{\sigma}_t$ )	(16.4, 0.3) dBm	(19.4, 0.6) dBm
clutter ( $\hat{\mu}_c, \hat{\sigma}_c$ )	(2.2, 1.2) dBm	(-3.2, 3.9) dBm
TCR	14.2 dBm	22.6 dBm
normalized TCR	12	6

Table 2.2: Estimated parameters of unprocessed HV-pol sub-images.

The radar equation in Eq. 2.3 can be rewritten in logarithmic terms, so that

$$\sigma_R = P_r - P_t + 40 \log_{10}(R) + 30 \log_{10}(4\pi) - 20 \log_{10}(\lambda) \quad (2.4)$$

$$-20 \log_{10}(G_a) - L_{\text{misc}} \text{ (dBm} \cdot \text{m}^2/\text{m}^2), \quad (2.5)$$

where  $L_{\text{misc}}$  denotes miscellaneous losses in the system that haven't been accounted for, e.g. insertion loss of rotary joint and feeds, and VSWR mismatch. Since these values are relatively small (total 1-2 dB effect), they are ignored here. To compensate for these effects, a calibration sphere of known RCS would need to be used to determine  $L_{\text{misc}}$ , and hence the absolute power returned. Since our interest is only in the relative visibility of the target, absolute calibration is unnecessary. Therefore, without loss of generality, it is assumed that  $L_{\text{misc}} = 0$  dB for the purposes of this study.

### 2.3.3 Example images

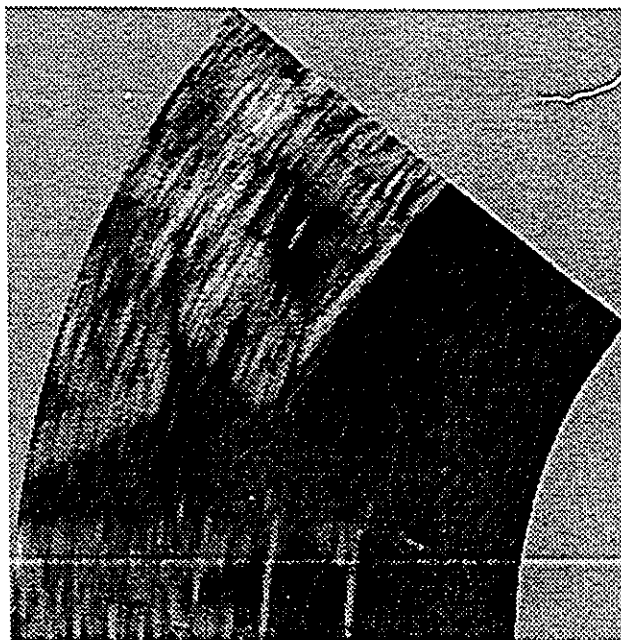
Figure 2.9 shows the PPI images of an example half-scan of digitized video for the HH-pol and HV-pol radar returns, respectively. For the purposes of display, the images are normalized in amplitude, so that the largest valued pixels in the image are mapped to white, and likewise the smallest valued pixels in the image are mapped to black.

The orientation of the PPI images is such that top of the display is in the westerly direction; the left part of the image contains the Dofasco site, and the right part of the image is in Burlington and contains the La Salle Park site. The reflectors are annotated on the HV-pol PPI image.

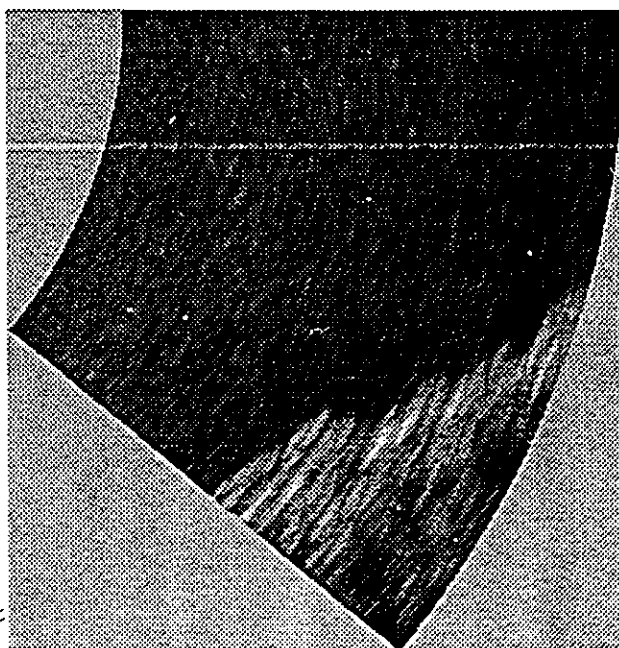
## 2.4 Traditional processing

In this section the performance of traditional processing techniques is evaluated. Only the HV-pol image data is used to enhance the reflector target visibility. These results provide a benchmark by which to gauge the performance of the more sophisticated joint HH-pol and HV-pol processing techniques described in subsequent chapters.

In total, 28 half-scans (equivalent to 1 minute's worth) of radar data were recovered from a recording dated November 23, 1987, and preprocessed according to the methods described above. This same data set was used throughout the study. The example sub-images shown in Fig. 2.10 and Fig. 2.11 are the basis for the visual and numerical comparison of the

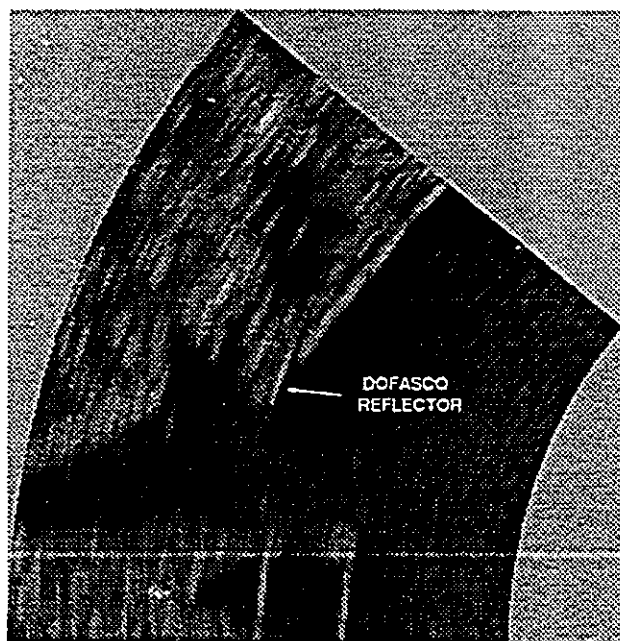


Dofasco

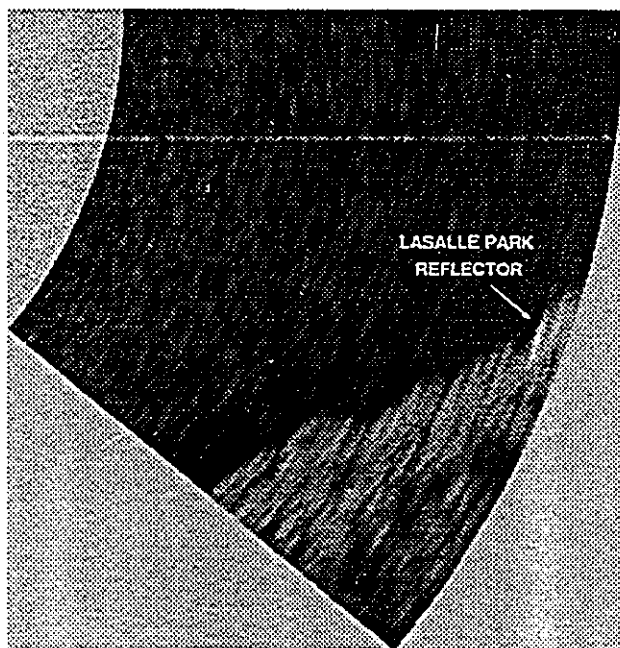


La Salle Park

Figure 2.10: The HH-pol sub-images of interest.



Dofasco



La Salle Park

Figure 2.11: The HV-pol sub-images with the locations of the reflectors marked.

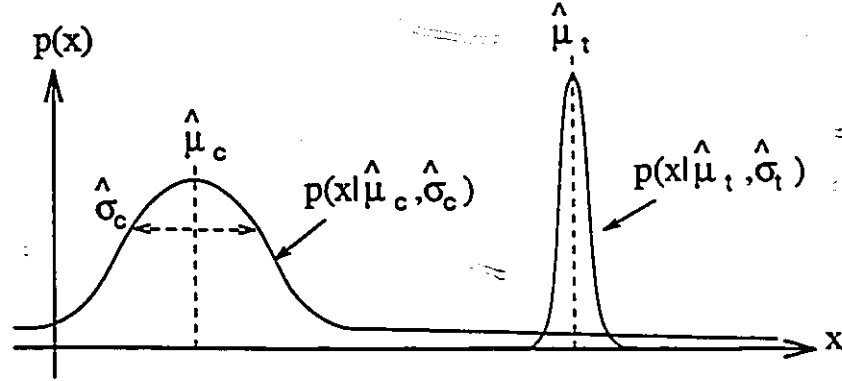


Figure 2.12: The target and clutter densities and the associated parameters used in calculating the normalized TCR figure of merit.

various joint signal processing techniques. It is assumed that a ship's tracking algorithm window would be initialized to an area of similar (or smaller) size to acquire and track the reflector target position. The sub-images chosen are  $800 \times 420$  samples, corresponding to a physical area of approximately  $2100 \times 2100 = 4,410,000 \text{ m}^2$ .

The target-to-clutter (TCR) estimate is given by the ratio of target power to clutter power. Since we are dealing with a log receiver with the output calibrated in dBm, the TCR is given by

$$\text{TCR} = \hat{\mu}_t - \hat{\mu}_c \text{ dBm} , \quad (2.6)$$

where  $\hat{\mu}_t$  is the estimated mean target response, and  $\hat{\mu}_c$  is the estimated mean clutter response. Figure 2.12 shows diagrammatically the probability density functions (pdfs) and the estimated parameters for the corresponding target and clutter densities.

Unfortunately, the TCR estimate does not provide a good measure of target enhancement or visibility. Various signal processing methods can scale the logarithmic data, resulting in a meaningless estimate of the TCR. For example, simply by scaling the data by a factor of 2, the TCR value would also double, without any true enhancement to the target. To overcome this problem, a dimensionless measure based on the TCR is proposed as a figure of merit by which to judge the various processing methods. The normalized TCR (NTCR) is given as

$$\text{NTCR} = \frac{\hat{\mu}_t - \hat{\mu}_c}{\hat{\sigma}_c} , \quad (2.7)$$

where  $\hat{\sigma}_c$  is the estimated standard deviation of the clutter power in dBm. If we assume that the pdf's are Gaussian, the NTCR is equivalent to the threshold used to calculate the probability of false alarm ( $P_{FA}$ ) for this model, where

$$P_{FA} = Q(\text{NTCR}) = \frac{1}{2} \text{erfc} \left( \frac{\text{NTCR}}{\sqrt{2}} \right) , \quad (2.8)$$

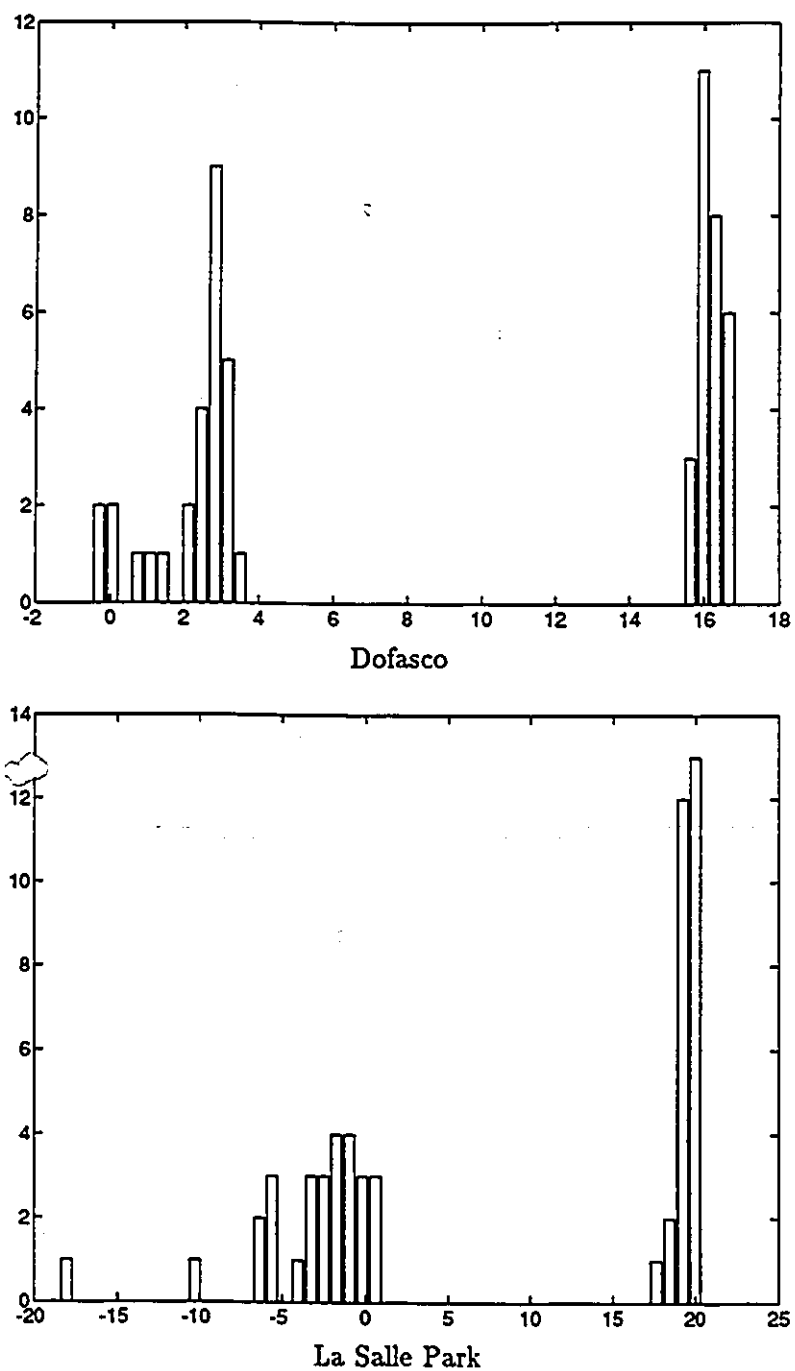


Figure 2.13: Estimated histograms of peak target and average clutter of unprocessed data.

Dofasco site clutter region    La Salle Park site clutter region  
(180x20 pixels)                      (180x20 pixels)



Figure 2.14: Representative patches of HV-pol clutter from the corresponding Dofasco and La Salle Park areas.

where the  $Q$  function is itself defined by

$$Q(x) \triangleq \frac{1}{\sqrt{2\pi}} \int_x^{\infty} e^{-y^2/2} dy, \quad (2.9)$$

and  $\text{erfc}(\cdot)$  is the complementary error function [72].

The target and clutter estimates are summarized in Table 2.2 for the HV-pol sub-images. The estimates are computed from the corresponding histograms shown in Fig. 2.13. The graphs show the histogram of the average clutter (in a representative area), and the histogram of peak target values. The clutter patches shown in Fig. 2.14 were chosen to provide representative areas of clutter from both sites. The clutter patch within the Dofasco site is approximately 572 m in azimuth and 100 m in range, and the corresponding La Salle Park clutter patch is approximately 528 m in azimuth by 100 m in range. To make the estimate, the average clutter response within the patch areas is averaged, and then averaged over all the scans to estimate a mean clutter level. The mean of the peak reflector target value is estimated by averaging the peak response within the reflector target cell area over the 28 scans.

#### 2.4.1 CFAR processing

The constant false alarm rate (CFAR) processor is commonly used in radar systems. It prevents saturation of the detector due to increases in clutter or noise by adapting the detection threshold in step with the changing clutter or noise conditions. Likewise, in the case that the clutter or noise decreases, it lowers the threshold thereby increasing the detectability of weaker targets which otherwise would be missed. The operation of CFAR

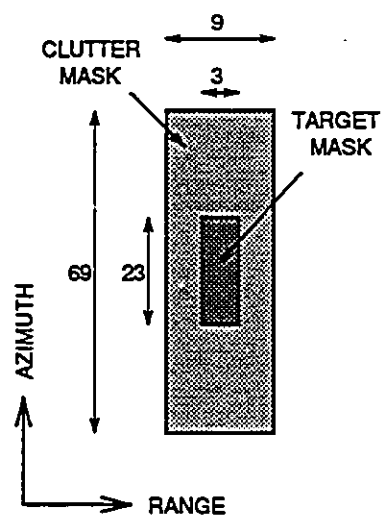
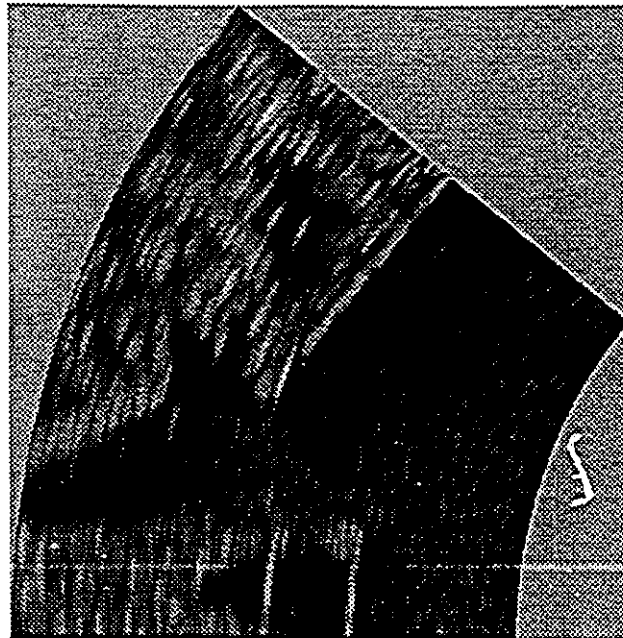


Figure 2.15: Target and clutter masks used in CFAR processing.

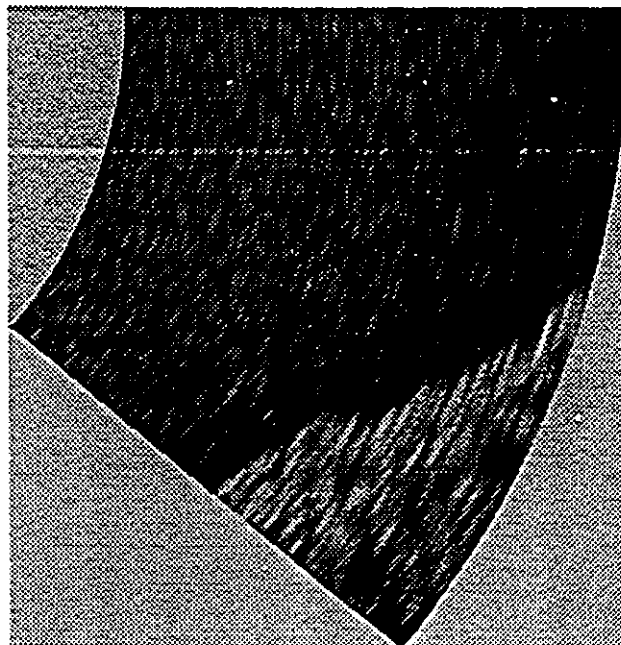
	Dofasco	La Salle Park
target ( $\hat{\mu}_t, \hat{\sigma}_t$ )	(22.9, 0.3) dBm	(24.0, 0.9) dBm
clutter ( $\hat{\mu}_c, \hat{\sigma}_c$ )	(2.8, 1.2) dBm	(-2.0, 3.7) dBm
TCR	20.1 dBm	26.0 dBm
normalized TCR	16	7

Table 2.3: Estimated parameters for CA-CFAR processed HV-pol sub-images.





Dofasco



La Salle Park

Figure 2.16: Sub-images of the CFAR processing, prior to detection.

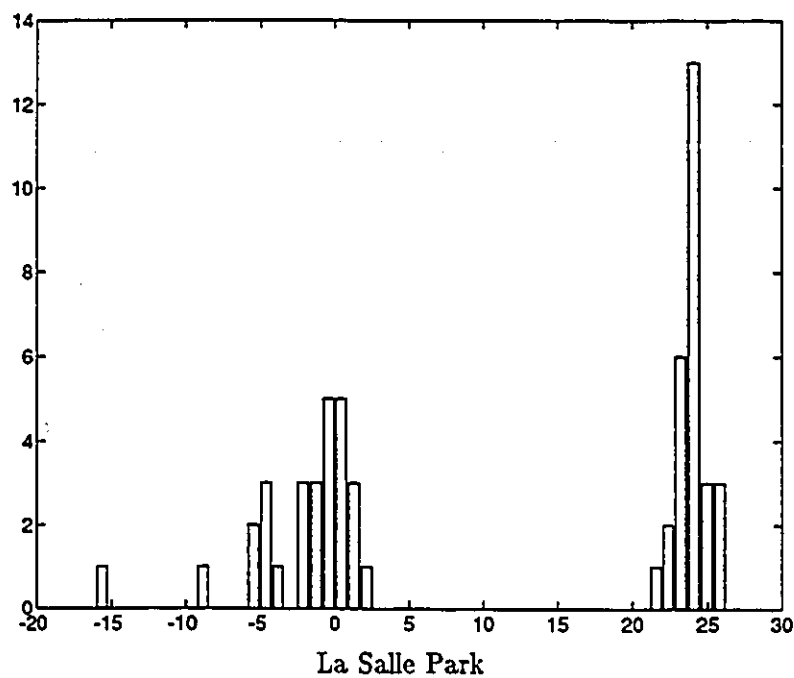
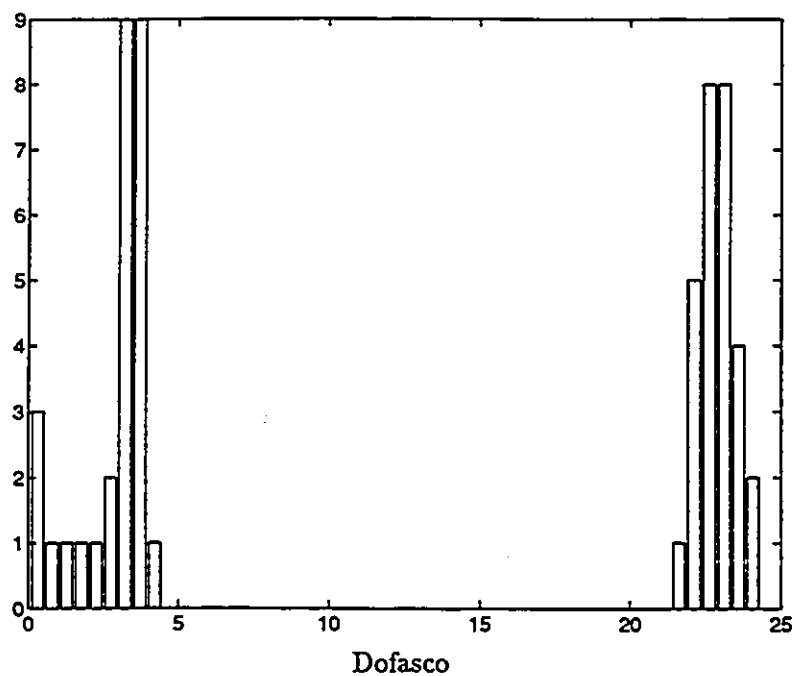


Figure 2.17: Estimated histograms of peak target and average clutter for CA-CFAR processed result.

systems has been widely studied [18, 48, 52, 62]. The basic idea is to estimate a sufficient statistic of the clutter, and to use this estimate to control a detection threshold so that a constant false alarm rate results.

The CFAR processor is now derived. For the purposes of this study, the clutter process is assumed to be Rayleigh distributed. The Rayleigh probability density function is given by

$$p(x) = \frac{2x}{\sigma^2} \exp\left(-\frac{x^2}{\sigma^2}\right), \quad x > 0, \quad (2.10)$$

where  $x$  is the voltage amplitude, and  $\sigma^2$  is the variance. The ideal logarithmic receiver is described by the function

$$y = a \log(bx), \quad (2.11)$$

where  $a$  and  $b$  are scale factors. Under these assumptions, Cronev [6] shows that the theoretical variance of the output is

$$\sigma_y^2 = \frac{a^2 \pi^2}{24}, \quad (2.12)$$

which is independent of the input signal. The logarithmic receiver therefore has a CFAR-like operation, in the sense that clutter described by Rayleigh distribution results in a constant variance in the output. The mean level of the clutter, however, is a function of the input power, and can be removed either by using a high-pass filter, or by using averaging to estimate the mean level and subtracting it. The cell-averaging CFAR (CA-CFAR) model assumes that the clutter in the neighborhood of a cell under test is a stationary statistical process, with independent samples, and is representative of the clutter in the test cell. In practice, these statistical assumptions are often not consistent with the operating environment, resulting in a loss in performance.

To implement the desired cell-averaging operation, two-dimensional target masks and clutter masks are used. Two masks are defined: a 23x3 pixel mask for the target, and a 69x9 pixel mask for the surrounding clutter. The target mask size was chosen to reflect the approximate size of the reflector target, and the clutter mask size was chosen to be large enough so as to provide a fair estimate of the clutter power, while at the same time being small enough so as to be in a stationary region of clutter. This is a trade-off in CA-CFAR processing. The two masks are co-located, centered on the same pixel, the clutter mask having zero response where the target mask coincides with it. Figure 2.15 shows the configuration graphically. The pixels in the mask are all equally weighted, although this need not be the case. For example, if there is *a priori* information about the clutter pdf characteristics, or location of the target within the clutter, a particular weighting configuration could have better performance. No such assumptions are made here. The masks are convolved with the image; the clutter-convolved result is subtracted from the target-convolved result. For a particular location in the image, the function can be expressed as

$$y = \sum_i^{N_t} w_i^t t_i - \sum_i^{N_c} w_i^c c_i, \quad (2.13)$$

were  $y$  is the output, the  $t_i$  is the set of target pixels, the  $c_i$  are the set of surrounding clutter pixels, the  $w_i^t$  are the set of target-pixel weightings, and the  $w_i^c$  are the set of clutter-pixel weightings. For the purposes of this study, no *a priori* information is used about the clutter orientation or distribution. The set of weights in the clutter mask are assigned the equal values  $\{w_i^c = 1/N_c, \text{ for all } i\}$ . Likewise, the set of weights in the target mask are assigned the equal values  $w_i^t = 1/N_t$ . The resultant image formed by the CA-CFAR possesses a greater target visibility as demonstrated by the example sub-images shown in Fig. 2.16. To improve the contrast of the printed half-tone sub-images, the lower 8% of the image values are mapped to black for all CFAR processed images (as estimated from the estimated histogram).

The enhanced target visibility should be reflected in higher NTCR values. Comparing results, the normalized TCR values in Table 2.3 show an improvement over the corresponding NTCR values for the unprocessed HV-pol images in Table 2.2. Figure 2.17 shows the histograms of the CA-CFAR processed target and clutter data.

The detector stage after the CA-CFAR processing performs a threshold function, which produces a binary result such that

$$\begin{aligned} y &> \alpha, \quad z = 1, \quad \text{target present} \\ y &\leq \alpha, \quad z = 0, \quad \text{target absent} \end{aligned} \quad (2.14)$$

The constant  $\alpha$  controls the false alarm rate.

## 2.5 Summary

The radar experiment, located in Hamilton Bay, is described in detail. In total, 28 scans of dual-polarized radar data were collected from this area, and used throughout the thesis. The targets of interest are twist-grid reflectors located in the Dofasco area and the La Salle Park area. The PPI sub-images of these areas of interest are used throughout the thesis to subjectively estimate the enhancement performance of the suggested signal processing technique.

The operational parameters of the radar system, data acquisition system and data recovery system were outlined, as well as preliminary data processing techniques to calibrate the radar system and normalize for radar range variations.

Next, traditional radar signal processing techniques were investigated and figure of merits defined to serve as a benchmark by which the advanced signal processing methods may be compared against. The method of measuring NTCR was defined and shown to be a dimensionless, objective measure of performance. The traditional CA-CFAR technique was described and used to process the sub-images of interest. The improvement over the original preprocessed HV-pol image could be observed both subjectively, from the displayed sub-images, and objectively from the histograms and the NTCR values.

## Chapter 3

# Adaptive cross-polar interference canceller

In this chapter we address an adaptive signal processing solution that accounts for the non-stationary nature of the clutter process. With each new radar sweep, the clutter background will vary from sea clutter to various forms of land clutter, including large like-polar point targets in surroundings such as the Dofasco site that has many large metal buildings and machineries. The signal processor is designed to track these variations in clutter, removing the correlated portion of the HH-pol clutter from the HV-pol information. The result is an enhanced cross-polar target response. However, to be successful, the adaptive canceller must be tuned to the nature of the reflector, and must operate in a robust fashion.

### 3.1 Principle of adaptive interference cancellation

A schematic diagram of the single-tap adaptive interference canceller is shown in Fig. 3.1 for a sampled range (or equivalently, time) series. The canceller processes the HH-pol and HV-pol radar returns along the range dimension, as they are received, removing a weighted version of the HH-pol return (interference signal) from the HV-pol return (desired signal). Various adaptive algorithms have been developed to adjust the tap weight in some type of optimal fashion [24].

From Wiener filter theory [23], it is known that the optimum tap-weight solution under conditions of stationarity and a zero-mean Gaussian process is

$$w_{\text{opt}} = \frac{R_{\text{HH,HV}}(0)}{R_{\text{HH,HH}}(0)}, \quad (3.1)$$

where  $R_{\text{HH,HV}}(0)$  is the zero-lag cross-correlation between the two channels, and  $R_{\text{HH,HH}}(0)$  is the zero-lag autocorrelation of the HH-pol channel.

For a detailed discussion of the operation of adaptive filter algorithms and noise cancellation, the reader is referred to [24, 71, 70].

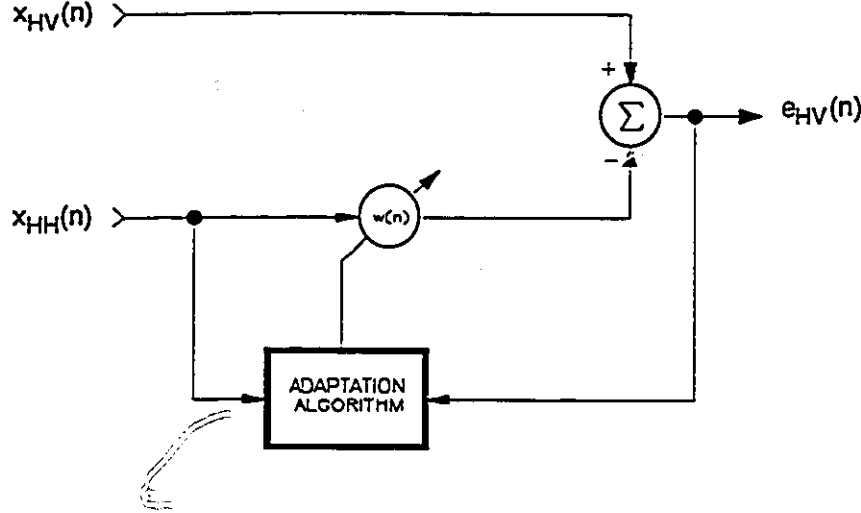


Figure 3.1: Discrete time cross-polar interference canceller

## 3.2 Discrete-time adaptation algorithms

There are two broad types of learning algorithms commonly used for adaptive filtering: the least-mean-square (LMS) and recursive-least-squares (RLS) algorithms. Both are presented here, and a link between the algorithms is developed. A transient response analysis of the LMS filter suggests a method for tuning the adaptive operation to improve reflector response. Finally, the theoretical performance is evaluated, showing the bounds on the cancellation performance as a function of the correlation between the HH-pol and HV-pol radar returns.

### 3.2.1 The LMS algorithm

The desired response in the following equations is set to be the HV-pol range sweep, and the disturbance to be the HH-pol range sweep, as shown by the block diagram in Fig. 3.1. The LMS update equations for the one-tap-weight case are therefore

$$\hat{e}_{HV}(n) = x_{HV}(n) - \hat{w}(n)x_{HH}(n), \quad n = 0, \dots, N-1, \quad (3.2)$$

$$\hat{w}(n+1) = \hat{w}(n) + \mu x_{HH}(n)\hat{e}_{HV}(n), \quad w(0) = 0, \quad (3.3)$$

where  $\hat{e}_{HV}(n)$  is the estimated *a posteriori* error at time  $n$ ,  $x_{HV}(n)$  is the signal containing the desired response,  $x_{HH}(n)$  is the interference that is correlated to  $x_{HV}(n)$ ,  $\hat{w}(n)$  is the estimated tap weight,  $\mu$  is the step-size parameter, and  $N$  is the total number of samples. The weight update algorithm is stable for  $\mu$  in the range

$$0 < \mu < \frac{2}{\sigma_{x_{HH}}^2}, \quad (3.4)$$

where  $\sigma_{x_{HH}}^2$  is the variance of the input  $x_{HH}(n)$ .

### 3.2.2 The RLS algorithm

The RLS algorithm is similar. The corresponding update equations for the one-tap weight case are

$$\hat{\alpha}_{HV}(n) = x_{HV}(n) - \hat{w}(n-1)x_{HH}(n), \quad (3.5)$$

$$\hat{w}(n) = \hat{w}(n-1) + k(n)\alpha_{HV}(n), \quad (3.6)$$

$$v(n) = \frac{1}{\lambda}P(n-1)x_{HH}(n), \quad (3.7)$$

$$k(n) = \frac{v(n)}{1 + x_{HH}(n)v(n)} \quad (3.8)$$

$$P(n) = \frac{1}{\lambda}P(n-1) - k(n)v(n), \quad (3.9)$$

where, in addition to the previous definitions,  $\hat{\alpha}_{HV}(n)$  is the estimated *a priori* error at time  $n$ ,  $k(n)$  is the gain,  $P(n) = 1/\hat{\sigma}_{x_{HH}}^2(n)$  is the inverse of the recursive variance estimate, and  $\lambda$  is the exponential weighting factor.

To gain insights into the operation of these different algorithms, the RLS algorithm is reinterpreted as a version of the LMS algorithm with a time-varying adaptive step-size parameter. Note the similarity between LMS weight update Eq. 3.3 and the RLS weight update Eq. 3.6. Rewriting Eq. 3.8 and substituting  $v(n)$ ,

$$k(n) = \frac{\frac{1}{\lambda}P(n-1)x_{HH}(n)}{1 + \frac{1}{\lambda}P(n-1)x_{HH}^2(n)} = \left( \frac{1}{\lambda/P(n-1) + x_{HH}^2(n)} \right) x_{HH}(n). \quad (3.10)$$

Now substituting  $\hat{\sigma}_{x_{HH}}^2(n-1)$  for  $1/P(n-1)$ , we have

$$k(n) = \left( \frac{1}{\lambda\hat{\sigma}_{x_{HH}}^2(n-1) + x_{HH}^2(n)} \right) x_{HH}(n) \Leftrightarrow \mu x_{HH}(n). \quad (3.11)$$

The  $\mu$  term on the right-hand side of Eq. 3.11 is comparable to the corresponding term in the RLS adaptive gain  $k(n)$ . It is observed that by adding a recursive variance estimate, the LMS algorithm can be converted to an RLS algorithm (for the one tap-weight case). An LMS algorithm modified in this fashion is referred to as being normalized [24]. The RLS is the more powerful algorithm since its convergence can be shown to be independent of the eigenvalues of the autocorrelation function of the disturbance, however, from now on the emphasis is on the LMS version of the adaptation algorithm since its implementation in hardware is simpler.

### Transient response

In the LMS algorithm, the step-size parameter  $\mu$  determines the adaptive interference canceller transient performance in a nonstationary environment. By studying the impulse response behaviour of the LMS algorithm, a reasonable choice for  $\mu$  can be made. Since the LMS weight update is data-dependent, some assumptions have to be made to make the analysis mathematically tractable. It is assumed that  $x_{HH}(n) = a$ , a constant. The weight update equation then becomes

$$\hat{w}(n+1) = \hat{w}(n) + \mu a \hat{e}_{HV}(n), \quad (3.12)$$

and in the  $z$ -transform domain,

$$(z-1)W(z) = \mu a E_{HV}(z), \quad (3.13)$$

$$E_{HV}(z) = X_{HV}(z) - X_{HH}(z) * W(z) = X_{HV}(z) - aW(z). \quad (3.14)$$

Now substituting for  $E_{HV}(z)$  and  $X_{HV}(z)$  in  $H(z)$ ,

$$H(z) = \frac{E_{HV}(z)}{X_{HV}(z)} = \frac{X_{HV}(z) - \mu a^2 E_{HV}(z)/(z-1)}{X_{HV}(z)} = 1 - \frac{\mu a^2}{(z-1)} H(z). \quad (3.15)$$

Rearranging,

$$H(z) = \frac{1}{1 + \mu a^2/(z-1)} = \frac{1 - z^{-1}}{1 - (1 - \mu a^2)z^{-1}}, \quad |z| > 1 - \mu a^2. \quad (3.16)$$

The  $z$ -transform pair

$$\left\{ \frac{1}{1 - e^{-\beta T} z^{-1}} \longleftrightarrow e^{-\beta n T} \right\} \quad (3.17)$$

defines a time constant  $\tau = 1/\beta$ . Finally, solving for the time constant in Eq. 3.16, it is found that

$$\tau = -\frac{T}{\ln(1 - \mu a^2)}. \quad (3.18)$$

The step response of  $H(z)$  is therefore determined to be a decaying exponential with time constant  $\tau$ .

Since the twist-grid reflector can be simplistically interpreted as causing a step-change in the cross-polar radar sweep, we can use this result to choose a reasonable  $\tau$  for the adaptive cross-polar clutter canceller. The pulse width of the radar transmitter fundamentally determines the length, or response duration of a point target. A good choice for  $\tau$  would be to allow the speed of adaptation to be as high as possible, but long enough so that the reflector response is not affected. Choosing a time constant that is too fast would cause the filter to start adapting to the reflector, and degrade the target-to-clutter ratio on the output. Choosing a time constant that is too long would impede the ability of the filter to adapt to changing clutter conditions and allow more clutter than necessary in the output. This result can also be used to choose a value of  $\lambda$  for the RLS algorithm, assuming that a reasonable estimate of the return power,  $\sigma_{x_{HH}}^2$ , can be made.



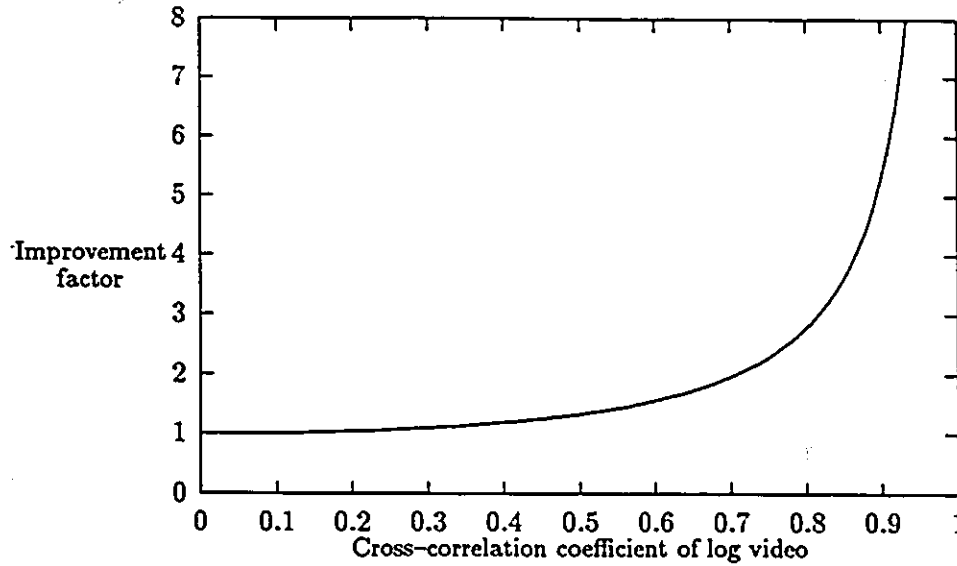


Figure 3.2: Ideal cancellation performance

### 3.2.3 Adaptive canceller performance

There is a common principle of operation for the aforementioned adaptive algorithms. The weight in the adaptive canceller is adjusted so as to reduce the correlation between the output  $\hat{e}_{HV}$  and the disturbance  $x_{HH}$ . This signal processing idea assumes that the desired signal,  $x_{HV}$ , has an unwanted component which is correlated to the disturbance,  $x_{HH}$ , and therefore can be removed. Adaptive cancellation will only work if the clutter between the cross-polarization channels is correlated.

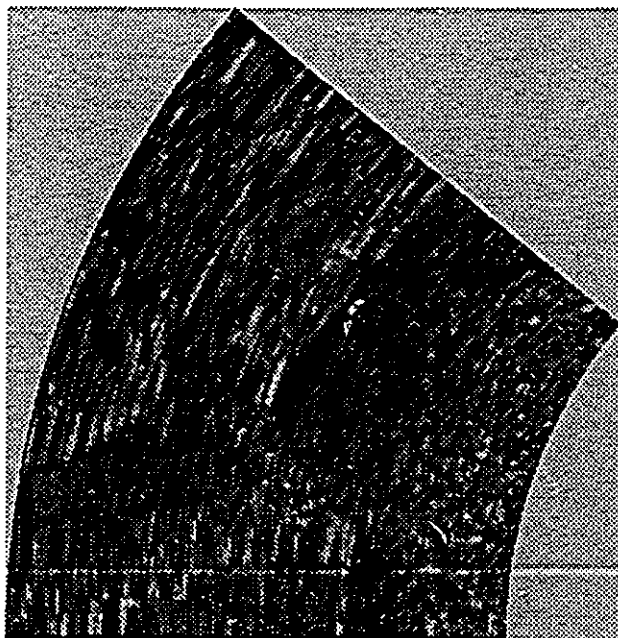
The cross-correlation coefficient between the HH-pol and HV-pol received signal is defined to be

$$\rho_{HH,HV} = \frac{E[x_{HH}x_{HV}]}{\sqrt{E(x_{HH}^2)E(x_{HV}^2)}} = \frac{R_{HH,HV}(0)}{\sqrt{R_{HH,HH}(0)R_{HV,HV}(0)}} \quad (3.19)$$

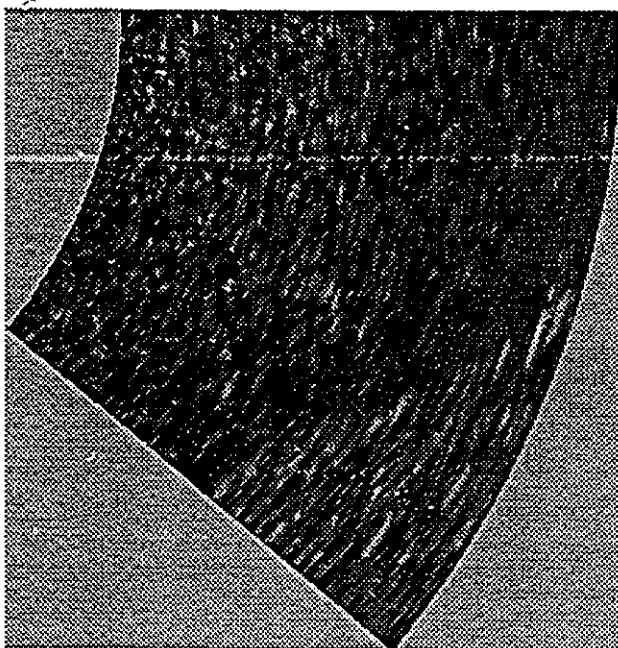
Assuming that the canceller is operating under stationary conditions and has converged to the optimum weight value, the reduction in clutter variance in the output is derived to be equal to

$$\frac{\sigma_{\hat{e}_{HV}}^2}{\sigma_{x_{HV}}^2} = 1 - \rho_{HH,HV}^2 \quad (3.20)$$

Fig. 3.2 is a graph of the ideal cancellation performance, showing the factor by which the normalized target-to-clutter ratio can be improved, versus the correlation coefficient between the  $x_{HV}$  and  $x_{HH}$  log video channels. This performance curve cannot be realized in practice, but it is useful as an indication of the possible bound on the expected performance.



Dofasco



La Salle Park

Figure 3.3: Sub-images of ACPIC processed data.

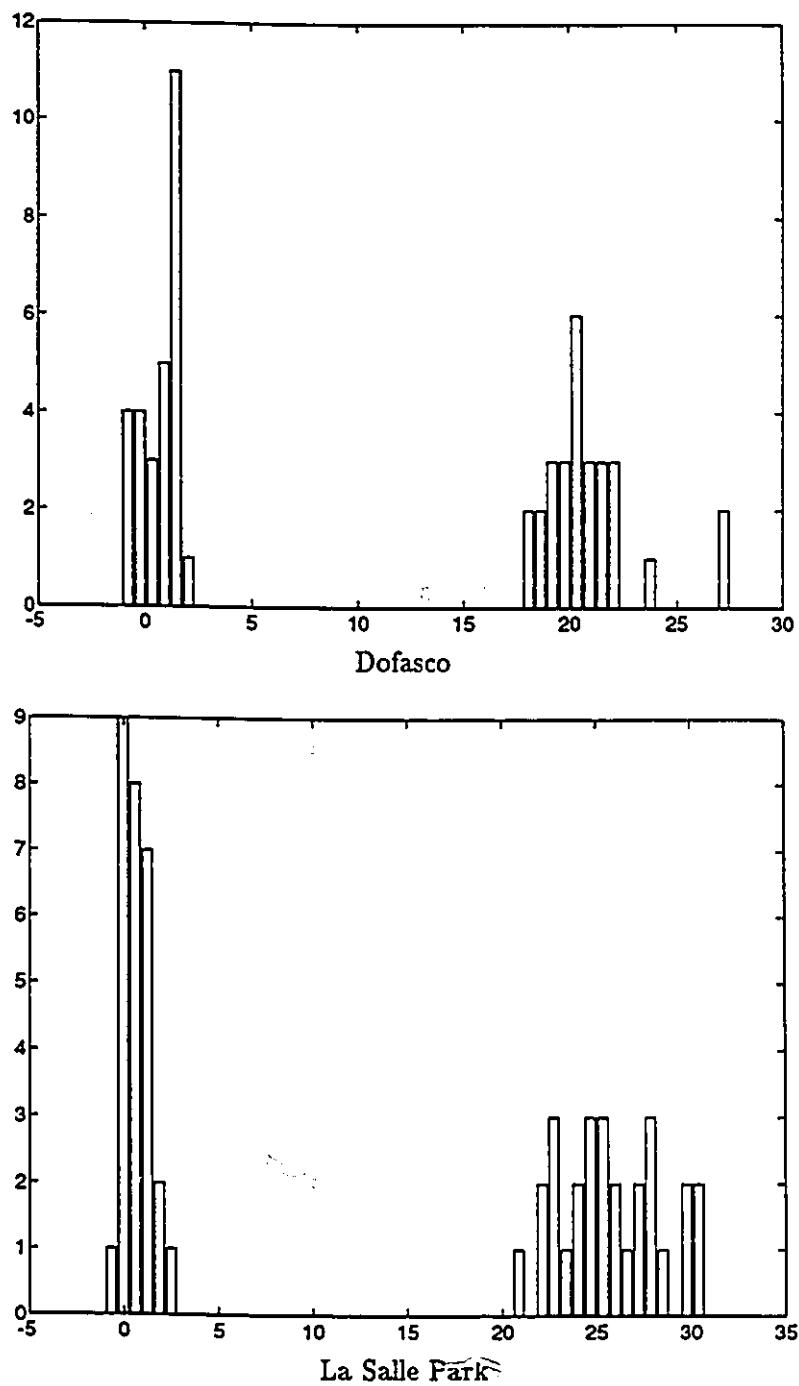


Figure 3.4: Estimated histograms of peak target and average clutter for ACPIC result.

	Dofasco	La Salle Park
target ( $\hat{\mu}_t, \hat{\sigma}_t$ )	(20.8, 2.2) dBm	(25.8, 2.6) dBm
clutter ( $\hat{\mu}_t, \hat{\sigma}_t$ )	(-0.4, 0.6) dBm	(1.3, 0.8) dBm
TCR	21.2 dBm	24.5 dBm
normalized TCR	35	29

Table 3.1: TCR estimate for ACPIC / CA-CFAR processed sub-images.

### 3.3 Discussion of results

The discrete LMS adaptive cross-polar interference canceller is used to process along the range sweep for each azimuth sampling of the scanning antenna. The processing is independent from sweep to sweep, and therefore does not take advantage of correlations that may exist in the azimuthal direction. A reasonable setting for the adaptation constant  $\mu$  was experimentally determined to be  $10^{-4}$ . This is confirmed by the transient response analysis. Using Eq. 3.16 and assuming  $\alpha = -30$  dBm, the time constant of the adaptive canceller is found to be approximately  $10.6T$ , where  $T$  is the sample time. The target width is approximate  $2 - 3T$ , so therefore the time constant meets the requirement of being short enough to adapt quickly to changing clutter conditions, and yet long enough so that the target is not adapted out.

The sub-images shown in Fig. 3.3 were processed with the adaptive interference canceller algorithm, then followed by the CA-CFAR processing. As is easily observed from the images, both the Dofasco and La Salle Park reflectors show greatly improved visibility. Table 3.1 summarizes the factor of improvement for the adaptive cross-polar clutter canceller output. The NTCR values exceed that of the CA-CFAR only processed images by nearly 20, indicating that the correlation between HH-pol and HV-pol radar sweeps is high. This is also reflected in the good separation between clutter and target histograms, as shown in Fig. 3.4.

A performance limitation of the canceller is generally observable along the edge of the sea and land clutter boundary. It takes a finite period of time (proportional to the  $\tau$  of the adaptive algorithm) for the canceller to respond to a different clutter region, in this case, land clutter. During this time an increase in clutter power can appear at the output.

### 3.4 Analog implementation

An analog version of the adaptive interference canceller is now presented. For the video bandwidth analog implementation of the adaptive cross-polar interference canceller, Haykin and Ukrainec successfully obtained Canadian and U.S. patents [27, 26]. A simplified block diagram of the analog canceller is shown in Fig. 3.5.

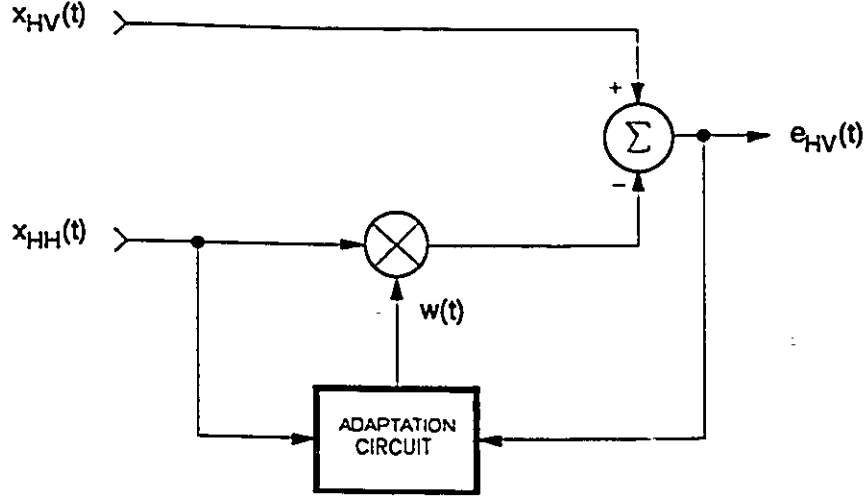


Figure 3.5: Continuous time cross-polar interference canceller.

#### 3.4.1 Continuous-time adaptation algorithm

The update equations are stated here, and the reader is referred to [33] for a more thorough analysis of the continuous-time LMS adaptive filter. The single tap-weight update equations are

$$\hat{e}_{HV}(t) = x_{HV}(t) - \hat{w}(t)x_{HH}(t), \quad t = 0, \dots, \infty, \quad (3.21)$$

$$w(t) = \rho \int_0^t x_{HH}(s)\hat{e}_{HV}(s)ds + w(0), \quad w(0) = 0. \quad (3.22)$$

The definition of the symbols is analogous to the discrete case, except for the introduction of the adaptive gain parameter  $\rho$ . It is important to differentiate between  $\rho$  and  $\mu$ . It is shown in [33] that the stable range of choice for  $\rho$  is not bounded. This result holds for a stationary, bounded input. In the discrete case the step-size parameter  $\mu$  is bounded, as stated in Eq. 3.4. These update equations can be extended to include the RLS case by using a continuous version of the result shown in Eq. 3.11. The only continuous-time analog adaptation algorithm considered here is the LMS version.

Figure 3.6 shows a block diagram of the analog hardware implementation of the adaptive cross-polar interference canceller using the LMS algorithm. Basic analog components, namely summers, multipliers and integrators are used, and attention is paid to the bandwidth necessary to operate with video signals. A wide-bandwidth prototype design was constructed and tested in the laboratory. The corresponding schematic diagram is shown in Fig 3.7. Testing with simulated signals, the canceller was found to operate as expected, up to a bandwidth of approximately 12 MHz.

A notable advantage of the adaptive interference canceller is its robust operation. It deals with changing conditions of operation, such as gain drifts in the radar set, magnetron

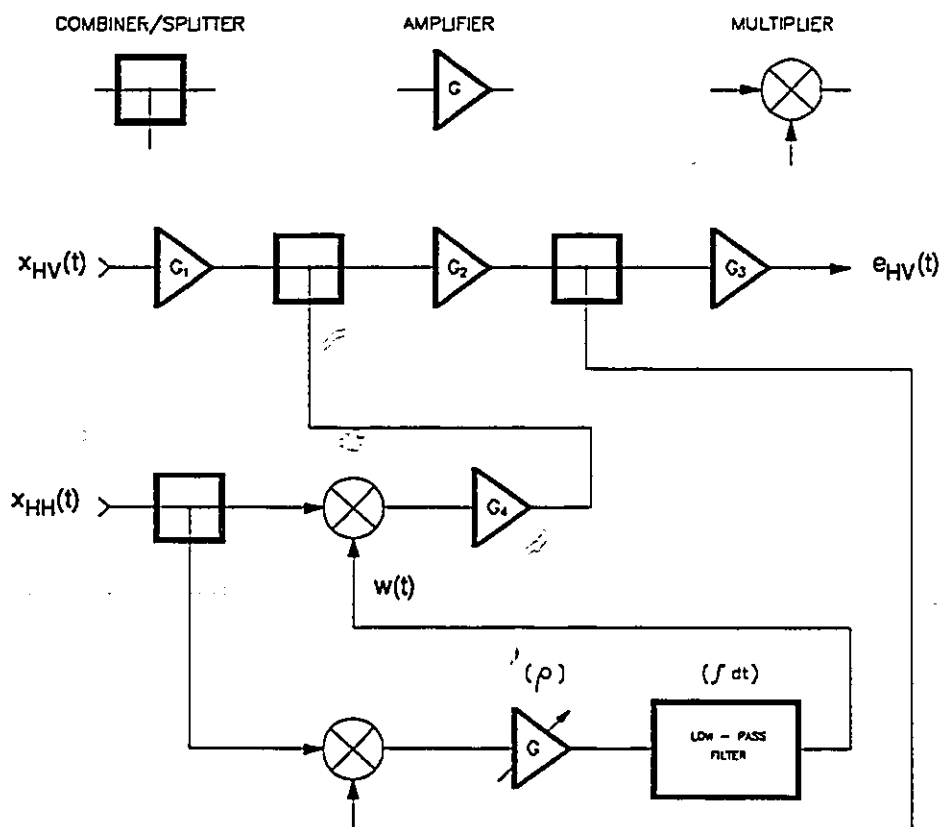


Figure 3.6: Block diagram of analog implementation.

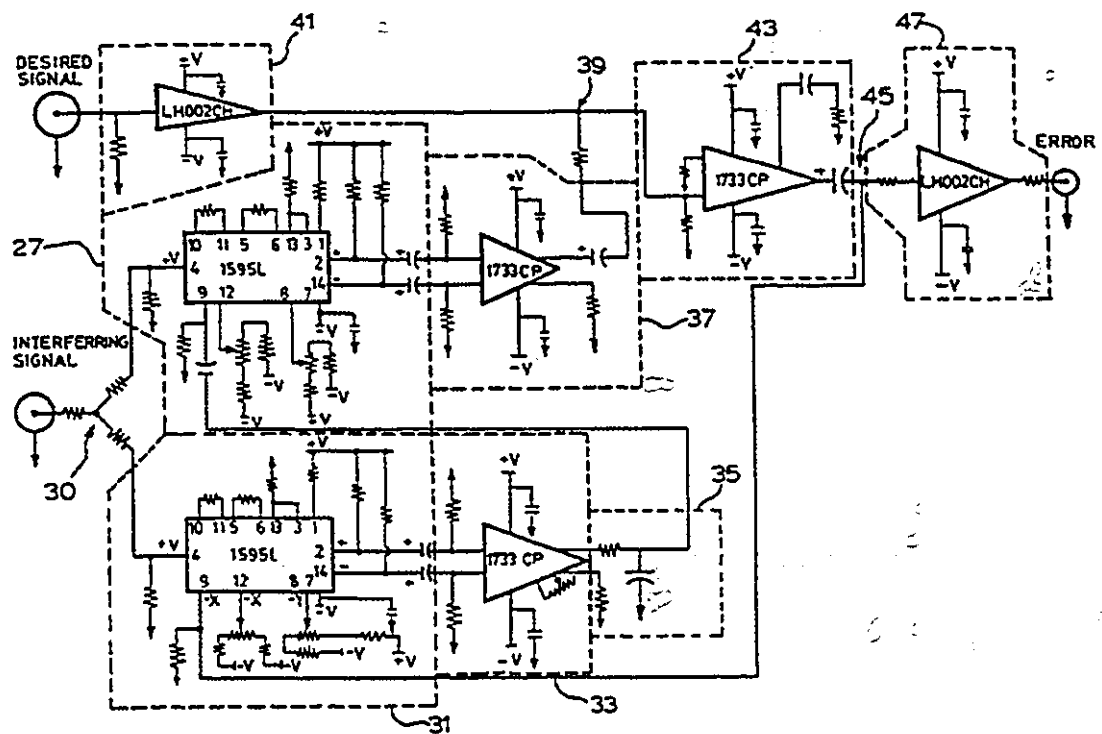


Figure 3.7: Schematic of analog cross-polar interference canceller. From the U.S. patent [26].

transmitter power fluctuations, or multipath fading. Adjustment of the response of the adaptive canceller customizes its response to that of the reflectors expected signature. These qualities make it an excellent processor for the detection of trihedral twist-grid reflectors.

### 3.5 Summary

One method of joint processing both HH-pol and HV-pol radar returns to enhance target visibility is given by the adaptive cross-polar interference canceller. The canceller is designed to remove the correlated clutter between the two polarization channels. As a result of the adaptive nature of the canceller, it is able to operate in the nonstationary clutter environment.

The theory of operation for the discrete LMS and RLS algorithms was derived. The design issues with regards to tuning the transient response to match the reflector and stationary performance limits were discussed.

The radar sweeps were processed using the LMS version of the discrete LMS canceller, and the resultant enhanced sub-images shown. The NTCR values and histograms reflect what the eye can see, namely the high level of clutter suppression and target enhancement achieved using this processing method in both the Dofasco and La Salle Park areas.

An analog implementation of the LMS-version of the ACPIC was suggested as a inexpensive and robust practical signal processing solution. A video bandwidth version of the canceller was designed, constructed, and tested. Based on this successful hardware implementation, Canadian and U.S. patents were granted.



## Chapter 4

# Mutual information networks

Gilbert stated that “Information will be a measure of time or cost of a sort which is of particular use to the engineer in his role of designer of an experiment” [15]. In this chapter, the statistical measures of information theory are used as cost functions in the unsupervised learning of neural networks. The desire is to process the HH-pol and HV-pol signals jointly such that the mutual information between the outputs is minimized, under the constraint that the output variance stays equal to that of the input. The expectation is that the cross-polar reflector target response energy should be maximized in one of the outputs.

### 4.1 Information-theoretic principles

A few definitions are presented first. The differential entropy of a continuous random variable may be written as [5]

$$H(X) = \int_S f(x) \log \left( \frac{1}{f(x)} \right) dx = - \int_S f(x) \log f(x) dx, \quad (4.1)$$

where  $f(x)$  is the probability density function (pdf) and  $S$  is defined as the support set, the set of values where  $f(x) > 0$ . The relative entropy, or as it is sometimes called, the Kullback–Leibler distance, is defined as

$$D(f_1 \parallel f_2) = \int f_1(x) \log \left( \frac{f_1(x)}{f_2(x)} \right) dx, \quad (4.2)$$

where the support set of  $f_1(x)$  contains the support of  $f_2(x)$  for the measure to be finite. The measure can be thought of as an oriented measure of distance between two probability density functions. A special case exists when the relative entropy between the joint probability density function  $f_{XY}(x, y)$  and the independent function of its respective probability density functions  $f_X(x)$  and  $f_Y(y)$  is considered. The mutual information between two random variables is defined to be

$$I(X; Y) = D(f_{XY}(x, y) \parallel f_X(x)f_Y(y)) = \iint f_{XY}(x, y) \log \left( \frac{f_{XY}(x, y)}{f_X(x)f_Y(y)} \right) dx dy. \quad (4.3)$$

Equivalently, in terms of differential entropies,

$$I(X; Y) = H(X) - H(X|Y) = H(Y) - H(Y|X) , \quad (4.4)$$

where  $H(X)$  is the differential entropy of  $X$ , and  $H(X|Y)$  is the conditional entropy of  $X$  given  $Y$ . The entropies  $H(Y)$  and  $H(Y|X)$  are similarly defined. In communications theory the mutual information is often used to measure the information capacity between the input and output of a noisy, band-limited channel.

The specific case of Gaussian pdf is now considered. The differential entropy of a zero-mean, multivariate Gaussian distribution is found to be

$$H_G(X_1, X_2, \dots, X_n) = H_G(\mathbf{X}) = \frac{1}{2} \log(2\pi e)^n |\mathbf{R}| , \quad (4.5)$$

where  $\mathbf{R} = E(\mathbf{X}\mathbf{X}^T)$  is the autocorrelation matrix of dimension  $n \times n$ . This also gives the upper bound on the differential entropy of continuous variables in that

$$H(\mathbf{X}) \leq H_G(\mathbf{X}) , \quad (4.6)$$

for  $\mathbf{X}$  zero-mean, given the same autocorrelation matrix [5]. Assuming that the joint distribution is a bivariate Gaussian pdf, the mutual information is found to be equal to [34]

$$I(X; Y) = -\frac{1}{2} \log(1 - \rho^2) , \quad (4.7)$$

where  $\rho$  is the correlation coefficient between  $x$  and  $y$ . In the Gaussian case, minimizing the mutual information is equivalent to driving the outputs to being statistically uncorrelated.

Some properties that are useful to computing information-related quantities in network architectures are now presented. The mutual information is equal to

$$I(X; Y) = 0 , \quad (4.8)$$

if and only if  $X$  is independent of  $Y$ . The entropy of a random variable remains unchanged after translation,  $Y = X + k$ , so that

$$H(Y) = H(X + k) = H(X) . \quad (4.9)$$

Under the linear transformation  $\mathbf{Y} = \mathbf{W}\mathbf{X}$ , the entropy change is increased, such that

$$H(\mathbf{Y}) = H(\mathbf{W}\mathbf{X}) = H(\mathbf{X}) + \log(|\mathbf{W}|) . \quad (4.10)$$

For any continuous transformation of a random variable  $\mathbf{Y} = F(\mathbf{X})$ , the entropy is equal to [69]

$$H(\mathbf{Y}) = H(\mathbf{X}) - E[\log(|J_F(\mathbf{X})|)] , \quad (4.11)$$

where  $J_F(\mathbf{X})$  is the Jacobian of the transformation.

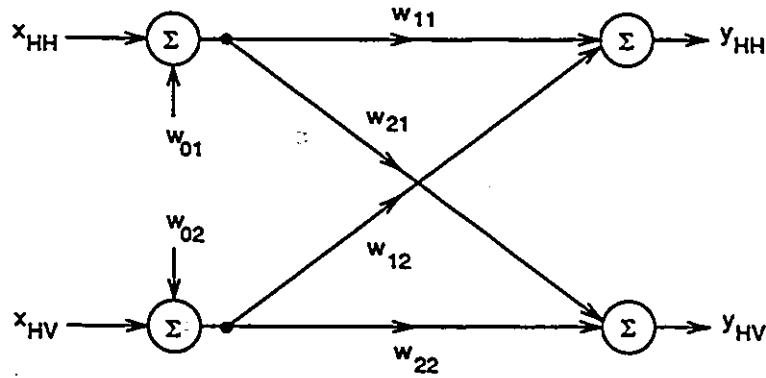


Figure 4.1: Linear neural network architecture.

## 4.2 Unsupervised learning of neural networks

Two types of networks are considered: a linear network, and a non-linear radial basis function (RBF) network. The linear network is easily trained and implemented, and is optimum in the case that a Gaussian pdf describes the data. The nonlinear RBF network is more difficult to train, however; it has more degrees of freedom to find nonlinear mappings that satisfy the optimization conditions. Both networks are static after they are trained; once the transformation is learned, the parameters are not changed during normal feed-forward operation.

### 4.2.1 Linear network

The linear network architecture is shown in Fig. 4.1. The transformation may be written as

$$Y = WX + w_0, \quad (4.12)$$

where  $X = [x_{HH} \mid x_{HV}]$  is the original data,  $Y = [y_{HH} \mid y_{HV}]$  is the output of the network, and  $W$  is the matrix of weights, and  $w_0$  is a constant bias vector. The desired mapping can be learned by finding the solution to a variational problem with constraints [13]. The weight solution is given by finding the solution to the gradient vector equation

$$\nabla_w I + \lambda \nabla_w J = 0, \quad (4.13)$$

where  $I$  is the mutual information cost function, and  $J$  is the constraint function that prevents trivial solutions (e.g. all weights equal to zero). The mutual information cost function that is to be minimized is therefore

$$C(W) = I(Y_{HH}; Y_{HV}) + \lambda ||WW^T| - 1|. \quad (4.14)$$

The  $w_0$  is set equal to the negative of the mean, and therefore does not appear in the cost function. The constraint term is introduced to ensure that the output covariance is

constant, and equal to the input covariance. This is easily verified. From the properties of determinants, it is known that

$$|YY^T| = |WXX^TW| = |WW^T||XX^T|. \quad (4.15)$$

The property given in Eq. 4.10 shows that this is equivalent to keeping the input and output entropy constant, as long as the determinant of the transformation is kept constant, no change in entropy occurs from input to output.

The linear transformation is restricted to effect first- and second- order statistics only. As a direct consequence of this fact, the best result that can be expected is to decorrelate the data. This is not as strong a condition as statistical independence. Independence implies uncorrelated behaviour, but uncorrelated behaviour does not imply independence, except for the case of Gaussian variates. From Eq. 4.7 it is known that the mutual information between two Gaussian variates achieves a minimum when they are uncorrelated. The task can therefore be reduced to finding an orthogonal transformation to decorrelate the output. A well-known statistical technique based on eigenvector decomposition is called principal components analysis (PCA) projection [31]. The PCA projection is a data-dependent transformation that applies a linear, orthogonal rotation to the original data, so as to remove the correlation between the dependent variables. Writing the equivalent equations,

$$Y = \widehat{W}X + \hat{w}_0, \quad \text{such that} \quad E[YY^T] = R_y, \quad (4.16)$$

where

$$R_y^{ii} = \sigma_i^2, \quad R_y^{ij} = 0, \quad i \neq j. \quad (4.17)$$

The weights are then determined from the eigenvector decomposition

$$R_x = UDU^T, \quad D = \text{diag}(d_{ii}), \quad i = 1, \dots, n. \quad (4.18)$$

The weight matrix is therefore set equal to the eigenvector matrix,  $U$ , and the  $w_0$  vector is set equal to the mean of the input data. A singular value decomposition (SVD) may also be used [19].

The PCA approach has been cast into a connectionist framework, using a Hebbian learning rule to achieve optimal (in the linear sense) unsupervised learning. Oja [55], Sanger [61] and others have demonstrated online versions of the PCA algorithm. The linear network has the advantage of being guaranteed (under reasonable conditions) to converge to a single, global maximum. Kung [35] provides an extensive survey of PCA learning techniques for neural networks. The Oja learning algorithm,

$$\hat{w}(n+1) = \hat{w}(n) + \beta [x(n)y(n) - \hat{w}(n)y(n)^2], \quad (4.19)$$

was used to find the principal component [35]. The parameter  $\beta$  is the learning rate. The orthogonal component to the estimated principal component is

$$\hat{w}_\perp = [-\hat{w}(2) \quad \hat{w}(1)]. \quad (4.20)$$

The complete weight matrix is therefore

$$\widehat{W} = \begin{bmatrix} \hat{w} \\ \hat{w}_\perp \end{bmatrix} \quad (4.21)$$

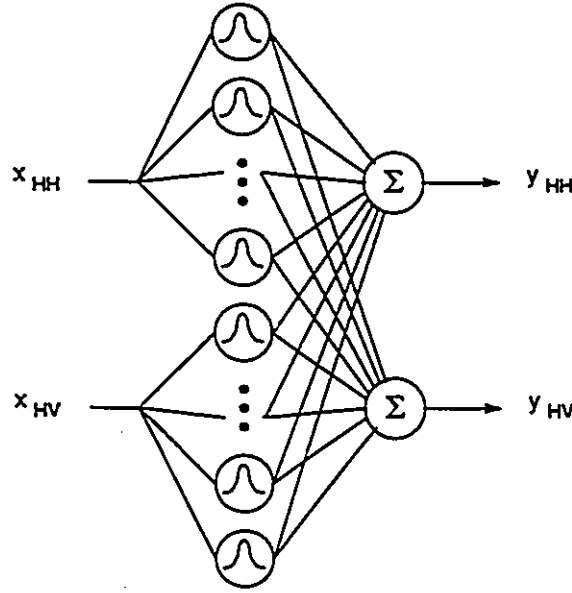


Figure 4.2: The radial basis function neural network architecture.

#### 4.2.2 Radial basis function neural network

An early work study by Ukrainec and Haykin showed that a multilayer perceptron neural network was able to perform difficult signal processing tasks, such as prediction on a nonlinear time series [65, 22]. Radial basis function (RBF) neural networks have also been successfully used by several researchers to solve difficult problems in signal processing [2, 3, 32, 40, 39, 50, 49, 60, 22]. The RBF network architecture used here is presented in Fig. 4.2. The inputs connect to a nonlinear hidden layer. The hidden layer, in turn, is connected to the output by a linear layer. The hidden layer nonlinear functions are of a type called radially symmetric basis functions. These functions can be chosen to be one of many different forms possible. Here only the Gaussian form will be used. The nonlinear functionals in the hidden layer are given by

$$\phi_j(\mathbf{x}) = e^{-\frac{1}{2}(\mathbf{x}-\mathbf{c}_j)^T \mathbf{S}_j (\mathbf{x}-\mathbf{c}_j)} = e^{-\frac{1}{2}\|\mathbf{x}-\mathbf{c}_j\|_M^2} \quad (4.22)$$

where  $\mathbf{x} \stackrel{\text{def}}{=} (x_1, \dots, x_{n_x})^T$ ,  $\phi_j(\mathbf{x})$  is the  $j^{\text{th}}$  radial basis function evaluated at the input vector  $\mathbf{x}$ ,  $\mathbf{c}_j$  is the  $j^{\text{th}}$  RBF center, and  $\mathbf{S}_j$  is the  $j^{\text{th}}$  multidimensional width, or spread. The term in the exponential is known as the Mahalanobis metric, or weighted Euclidean metric. The functional form of the RBF network is therefore given by

$$y_i = \sum_{j=1}^{n_h} w_j \phi_j(\mathbf{x}) + w_0 \quad (4.23)$$

where  $y_i$  is the  $i^{th}$  output function evaluated for the input vector  $\mathbf{x}$ , and  $w_j$  is the linear output weight corresponding to the  $j^{th}$  hidden unit. The hidden layer has a total of  $n_h$  radial basis functions. The weight  $w_0$  is the bias term. Given a set of input data vectors and output data,  $\{\mathbf{x}_i, y_i^j \mid i = 1, \dots, n, j = 1, \dots, n_o\}$ ,

$$\mathbf{X} = \begin{pmatrix} \mathbf{x}_1 \\ \mathbf{x}_2 \\ \vdots \\ \mathbf{x}_n \end{pmatrix}, \quad \Phi = \begin{pmatrix} 1 & \phi_1(\mathbf{x}_1) & \phi_2(\mathbf{x}_1) & \cdots & \phi_{n_h}(\mathbf{x}_1) \\ 1 & \phi_1(\mathbf{x}_2) & \phi_2(\mathbf{x}_2) & \cdots & \phi_{n_h}(\mathbf{x}_2) \\ \vdots & \vdots & \vdots & \ddots & \vdots \\ 1 & \phi_1(\mathbf{x}_n) & \phi_2(\mathbf{x}_n) & \cdots & \phi_{n_h}(\mathbf{x}_n) \end{pmatrix}, \quad \mathbf{Y} = \begin{pmatrix} y_1^1 & y_1^2 & \cdots & y_1^{n_o} \\ y_2^1 & y_2^2 & \cdots & y_2^{n_o} \\ \vdots & \vdots & \ddots & \vdots \\ y_n^1 & y_n^2 & \cdots & y_n^{n_o} \end{pmatrix}$$

where  $n_o$  is the number of outputs. Rewriting Eq. 4.23 in matrix form,

$$\mathbf{Y} = \Phi(\mathbf{X})\mathbf{W}. \quad (4.24)$$

### Network design strategies

The determination of the hidden layer parameters is a challenging task. Various procedures have been experimented with to learn the centres and widths (or spread) of the hidden layer of RBF units.

Several non-adaptive strategies have been used to determine the RBF centres and spread. The most straightforward choice for the location of the centres is to place them on an evenly spaced grid, spanning the input space. Unfortunately, a very large number of RBF units may be needed, since the number of units required grows exponentially with the dimensionality of the input space. As the dimensionality of the input grows, most of the input space becomes devoid of samples, and therefore a large percentage of the centres lie in an area where there are no data. Another more effective choice for the RBF centres is to set the centres equal to a random sampling of the input data. This strategy ensures that centres are located only in areas where there are data. It has been shown that as long as a sufficiently large number of centres are used, good prediction performance on a chaotic time series is achieved[2]. In either case, the RBF spreads are chosen using some heuristic method.

Supervised adaptation of the RBF centres, spreads, and output weights using optimization techniques have been used [40, 50]. This strategy can give a minimal RBF network configuration. Some of disadvantages with using optimization techniques are considerable computational cost, poor scaling of learning as network complexity grows, and the presence of sub-optimal local minimum solutions. Lowe[40] points out that the same final error performance can be achieved with a network with a larger number of non-adaptive centres, with the same generalization performance.

The investigations of hybridized unsupervised/supervised training schemes have shown promise [50, 49, 60, 54]. Some of the advantages are computational efficiency, good scaling of learning as network size grows, and faster convergence. The hybrid procedure consists of two stages of learning: an unsupervised clustering algorithm is used to determine the parameters of the hidden layer, followed by a supervised least-squares solution to the linear output weights. Moody and Darken[50, 49] suggest the use of the k-means clustering algorithm

to find suitable positions for the centres. As a result, a smaller number of RBF units are required. After clustering, heuristic methods are used to choose the spreads of the RBF units. The k-means algorithm is an approximate version of the maximum likelihood (M-L) solution for determining the location of the means of a mixture density of component densities. The expectation maximization (EM) algorithm can be used to find the exact M-L solution for the means and covariances of the density. A comparison of these two learning strategies on a classification problem was done by Nowlan[54, 53], with the EM algorithm shown to be superior. Saha and Keeler also studied the use of the k-means clustering for the adjustment of RBF centres, and suggested an approach which they termed as *extended metric clustering*[60], where clustering is done in an augmented input-output space. Once learning is complete, the cluster locations are projected back onto the input space, and used as the RBF unit centres. In recent studies by Ukrainec and Haykin [67, 22] the hybrid training was applied successfully to signal processing functions. It was shown that a combination of EM training and extended metric clustering, named EMX clustering, gave the best overall performance in the example prediction and cancellation signal processing problems.

This same concept of projecting the parameters onto a lower dimensional space is used here to learn the hidden layer RBF parameters. The EM learning is performed on the 2-dimensional input space, and then the parameters are projected down onto two 1-dimensional hidden layers. The linear layer then combines the localized representations to provide the desired mapping.

### Unsupervised clustering algorithm

The expectation maximization (EM) algorithm is a general approach to iteratively computing the maximum-likelihood (ML) estimate of parameters of mixture density problems. This algorithm has had broad application in the areas of study of ML estimates from incomplete data [8], estimating mixture densities [57], and unsupervised clustering [10]. Here we will concentrate on the application of the EM algorithm for unsupervised clustering, to learn the RBF centres and spreads.

A mixture distribution of Gaussian pdf's is given by

$$p(\mathbf{x}_k|\theta) = \sum_{j=1}^{n_h} P(j)p(\mathbf{x}_k|j, \theta_j) \quad (4.25)$$

$$p(\mathbf{x}_k|j, \theta_j) = \frac{1}{(2\pi)^{d/2}|\Sigma_j|^{1/2}} e^{-\frac{1}{2}(\mathbf{x}_k - \mu_j)^T \Sigma_j^{-1} (\mathbf{x}_k - \mu_j)} \quad (4.26)$$

where  $\theta = (\theta_1, \dots, \theta_{n_h})$  is the vector of parameters (means and covariances) to be estimated,  $d$  is the dimensionality of the multivariate Gaussian density,  $\mu_j$  is the mean, and  $\Sigma_j$  is the covariance. The EM algorithm iteratively converges to a maximum of the likelihood function, yielding an estimate of the parameters of the component densities. Although the algorithm is guaranteed to converge, there is no guarantee that it will converge to a global

maximum. The update equations are given as follows:

$$\hat{P}(i) = \frac{1}{n} \sum_{k=1}^n \hat{P}(i|\mathbf{x}_k, \hat{\theta}) \quad (4.27)$$

$$\hat{\mu}_i = \frac{\sum_{k=1}^n \hat{P}(i|\mathbf{x}_k, \hat{\theta}) \mathbf{x}_k}{\sum_{k=1}^n \hat{P}(i|\mathbf{x}_k, \hat{\theta})} \quad (4.28)$$

$$\hat{\Sigma}_i = \frac{\sum_{k=1}^n \hat{P}(i|\mathbf{x}_k, \hat{\theta}) (\mathbf{x}_k - \hat{\mu}_i)(\mathbf{x}_k - \hat{\mu}_i)^T}{\sum_{k=1}^n \hat{P}(i|\mathbf{x}_k, \hat{\theta})} \quad (4.29)$$

$$\hat{P}(i|\mathbf{x}_k, \hat{\theta}) = \frac{\hat{P}(i)p(\mathbf{x}_k|i, \hat{\theta}_i)}{\sum_{j=1}^n \hat{P}(j)p(\mathbf{x}_k|j, \hat{\theta}_j)} \quad (4.30)$$

An additional step was added to these standard update equations to ensure that the algorithm learned localized representations. The test

$$\hat{\Sigma}_i^{jj} = \Sigma_i^{jj}, \quad \text{if } \hat{\Sigma}_i^{jj} > \Sigma_i^{jj}, \quad (4.31)$$

ensures that the spread is limited to a maximum given by  $\Sigma_1$ . Without this extra step, the algorithm may converge to solutions where one or more of the components of the mixture distribution span a large area of the sample space, overlapping other components. Although these are valid solutions, they are not desirable when the parameters are to be transferred to a RBF network that presupposes localized representations.

The equations describe a batch processing algorithm, where all the data are used for each iteration. An on-line version of the EM algorithm was suggested by Nowlan [53], where the density parameters can be continuously updated as new data become available. This may have application if the input space is slowly changing, and the representations need to be fine tuned. For the purposes of this study, the batch update algorithm is used exclusively.

It is evident that the RBF given in Eq. (4.22) and the Gaussian component density in Eq. (4.26) have almost the same form. It is hypothesized that the individually learned  $\hat{\mu}_j$  of the component densities should give a good location for the centres of the RBF units. Likewise, the estimated covariances can give the required spread of the RBF units.

The hybrid learning procedure is therefore given as follows:

1. choose the number of RBF units (and hence the number of component densities);
2. initialize the density parameters;
3. iterate the EM algorithm until convergence;
4. transplant the estimated parameters of the component densities into the RBF units, so that  $\mathbf{c}_j \leftarrow \hat{\mu}_j$ ,  $\mathbf{S}_j \leftarrow \alpha \hat{\Sigma}_j^{-1}$ , where  $0 < \alpha \leq 1$ ;
5. forward-propagate the input data to the output of the RBF hidden layer;
6. compute solution to linear weight layer.



The factor  $\alpha$  is introduced to increase the spreads in order to smooth the interpolation performance of the network. As shown by Ukrainec and Haykin [67], the performance increases as  $\alpha$  is decreased, although localization of response decreases.

### Minimum mutual information learning

The mutual information cost function for the RBF network is similar to that of the linear network. The objective is to minimize the mutual information between the outputs, while keeping the output entropy fixed. Once the basis functions are trained using the unsupervised method described in the previous section, they are fixed and only the output layer of weights need to be learned. The cost function is therefore

$$C(W) = I(Y_{HH}; Y_{HV}) + \lambda |H(Y) - H(X)|. \quad (4.32)$$

The constraint term explicitly ensures that the output entropy is constant, and equal to the total input entropy. The advantage in using a nonlinear network over the linear network is in the increased degrees of freedom in the mapping. The entropy of the output is given by

$$H(Y) = H(X) - E[\log(|J_R(X)|)] + \log(|W|), \quad (4.33)$$

where  $J_R(X)$  is the Jacobian of the hidden layer transformation. The RBF network has an advantage here over other neural networks, such as the multilayer perceptron, in the sense that it has a set of fixed basis functions, or in other words, a non-adaptive hidden layer.

The numerical estimation of  $I(Y_{HH}; Y_{HV})$  requires either a *a priori* assumed distribution model or a model-free estimate. A model-free estimate is possible but is computationally expensive (order  $N \log N$  [14]), and must be recomputed on every iteration of the optimization routine used to minimize the cost function. Previous researchers Becker [1] and Zemel [73] have used the Gaussian distribution model assumption when attempting to estimate mutual information. Preliminary studies done by Ukrainec and Haykin [66, 68] have shown that it is possible to use the Gaussian-based mutual information measure given in Eq. 4.7 as an estimate of the mutual information. The advantage is that it is easy to compute. However, since the distribution is known to be non-Gaussian, it is also inaccurate. At best, this is an upper bound on the mutual information, since we know that by the property in Eq. 4.6 that for a given autocorrelation function, the differential entropy is upper bounded by the Gaussian distribution.

The cost function that is used is therefore

$$C(W) = -\frac{1}{2} \log(1 - \rho_{HH,HV}^2) + \lambda ||YY^T| - |XX^T| + J_{\text{misc}}|. \quad (4.34)$$

Through experimentation it was found that putting additional constraints on the output mean, variance, and skew improved convergence and helped to avoid undesirable local minima. The additional terms of  $J_{\text{misc}}$  are

$$|\hat{\mu}_{yHH}| + |\hat{\mu}_{yHV}|, \quad (4.35)$$

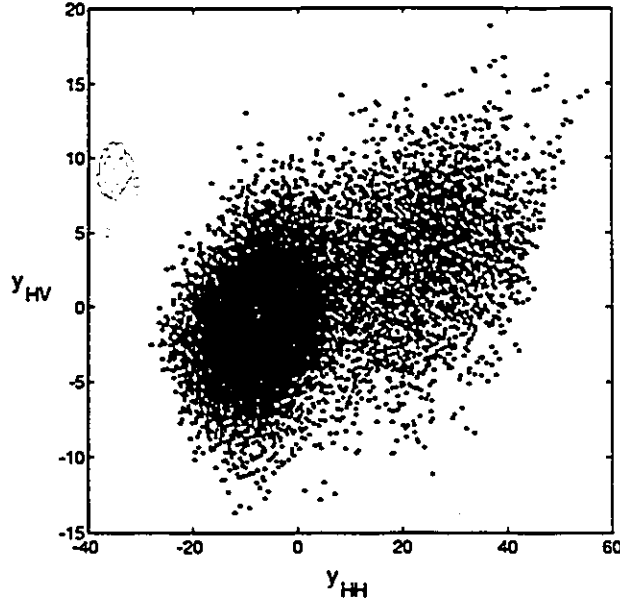


Figure 4.3: Scatter plot of the output of the linear network.

to insure zero-mean output. An equal output variance term,

$$|\hat{\sigma}_{y_{HH}} - \hat{\sigma}_{y_{HV}}|, \quad (4.36)$$

is introduced to encourage a circularly symmetric distribution. Finally, the third-order moment, or skew, is constrained. The additional penalty term is

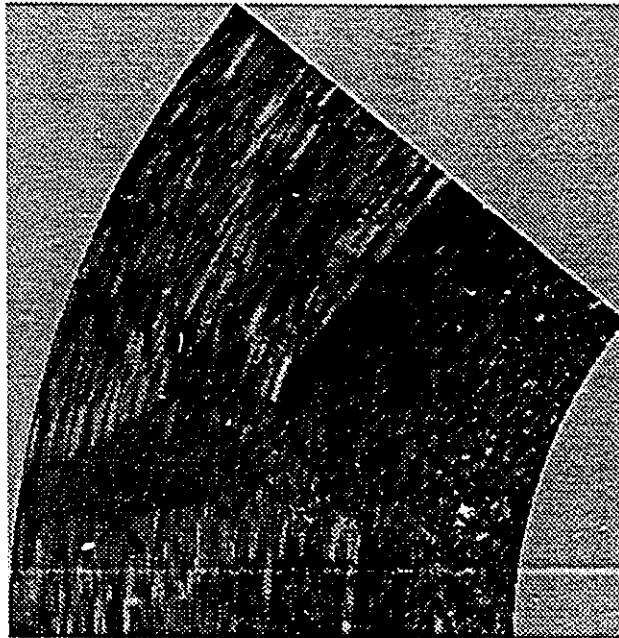
$$|\hat{\gamma}_{y_{HH}}| + |\hat{\gamma}_{y_{HV}}| \quad (4.37)$$

The quantity is normalized for the Gaussian distribution so that zero skew is equal to the skew of a Gaussian distribution, which has maximum entropy. In summary, constraints are introduced on the moments of the output so as to force the output to approximate a Gaussian pdf. A constrained optimization routine is used to minimize the cost function.

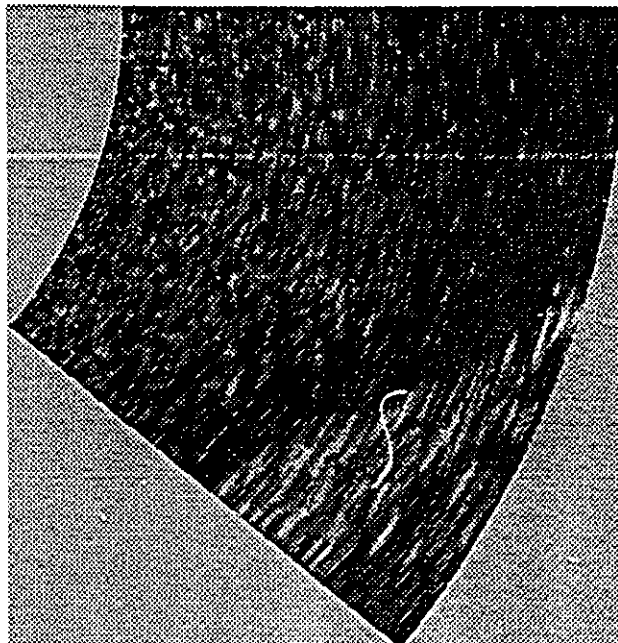
## 4.3 Experimental results

### 4.3.1 Linear network

PCA trained linear networks have been used in the past to enhance the contrast and target-to-clutter ratio of polarization targets [63, 37]. The principal component is the vector direction that has the largest variance when the data are projected onto it. It is assumed that this projection will contain most of the like-polarized clutter energy, and that the



Dofasco



La Salle Park

Figure 4.4: Sub-images of linear network processed data.

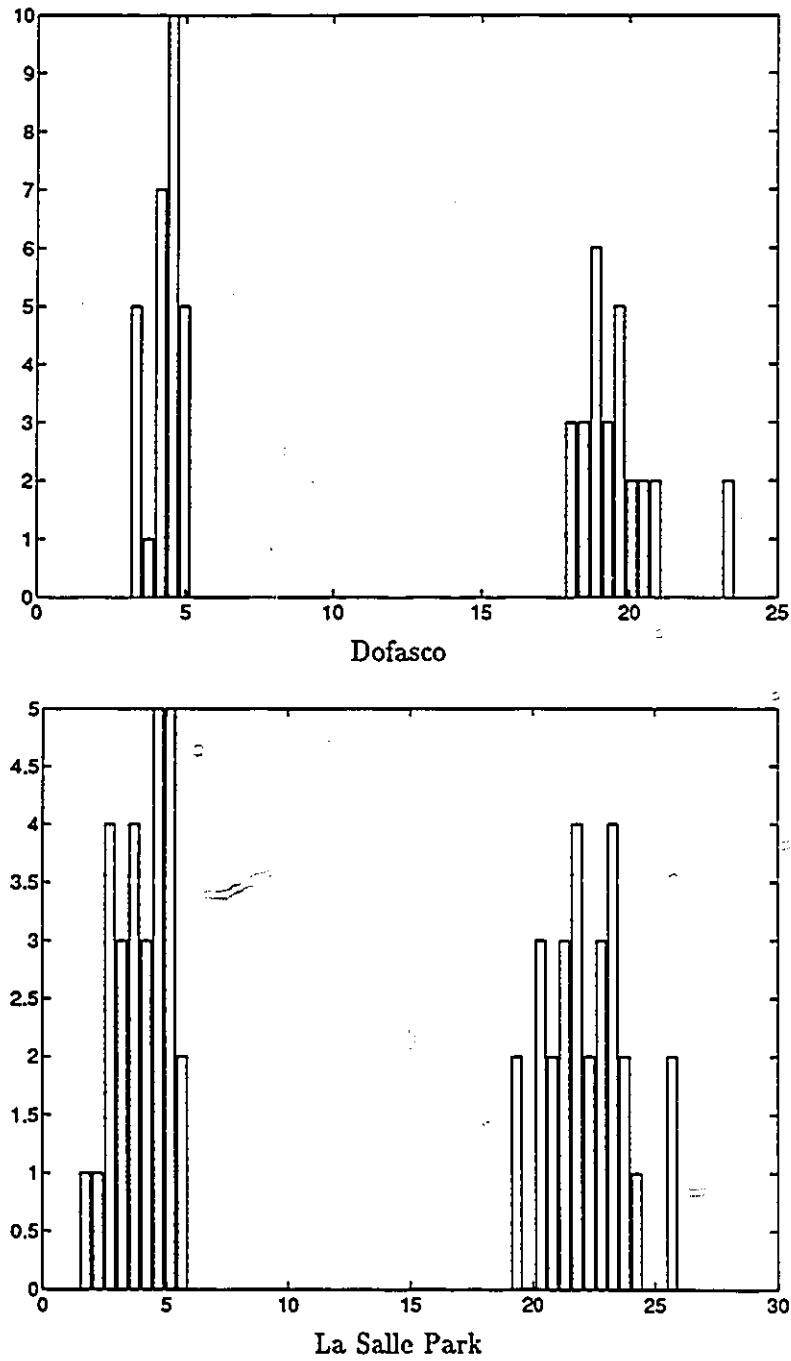


Figure 4.5: Estimated histograms of peak target and average clutter for linear network result.

	Dofasco	La Salle Park
target ( $\hat{\mu}_t, \hat{\sigma}_t$ )	(19.6, 1.38)	(22.2, 1.65)
clutter ( $\hat{\mu}_c, \hat{\sigma}_c$ )	(4.26, 0.553)	(4.01, 1.08)
TCR	15.3	18.2
normalized TCR	28	17

Table 4.1: Estimated parameters of linear network processed sub-images.

projection onto the direction orthogonal to the principal component,  $w_1$  will contain the desired reflector target response.

A representative  $200 \times 200$  pixel training sub-image was chosen that did not overlap either Dofasco or La Salle Park sub-images. After mean removal, the Oja algorithm was used to estimate the weight matrix. The sub-images of interest were then processed by the linear network and viewed. The resultant orthogonal images did not contain an enhanced reflector target, but rather had a much enhanced sea clutter component. After observing the scatter plot of the output of the linear network, it was obvious that this is a result of the non-Gaussian nature of the distribution. The sea clutter data values are more densely represented than the land clutter values, and therefore the orthogonal transformation was biased in the direction of the sea clutter. To overcome this problem, the orthogonal projection was biased so that a residual correlation remained. The scatter plot of the resulting output is shown in Fig. 4.3. This biased projection results in a residual correlation coefficient of approximately 0.53 in the output data, corresponding to a mutual information rate of approximately 0.1 bits.

Figure 4.4 shows the processed sub-images of interest, after the additional CFAR processing. The images show an enhanced target, although not nearly as prominently visible against the clutter background as that of the adaptive interference canceller. This is reflected in the estimated histograms in Fig. 4.5 and the normalized TCR results in Table 4.1. The NTCR values show that by comparison with the adaptive interference canceller, the performance is poorer. This is attributed to the adaptive nature of the canceller processing. In general, PCA techniques are applied against a single type of clutter background. The clutter process in these sub-images can be thought of as a mixture distribution, where the differing regions of clutter require a different projection.

#### 4.3.2 The RBF network

After initial explorations, a mixture density is learned using the EM algorithm, as described in Sec. 4.2.2. Again, the same  $200 \times 200$  clutter region is used for training. The scatter plot of the combined Dofasco and La Salle Park input data is shown in Fig. 4.7, with the learned ellipsoidal standard deviations of the components of the mixture of Gaussian densities superimposed. The number of components in the density used to model the clutter is chosen to be 7, with 2 extra units introduced to represent the reflectors. These extra

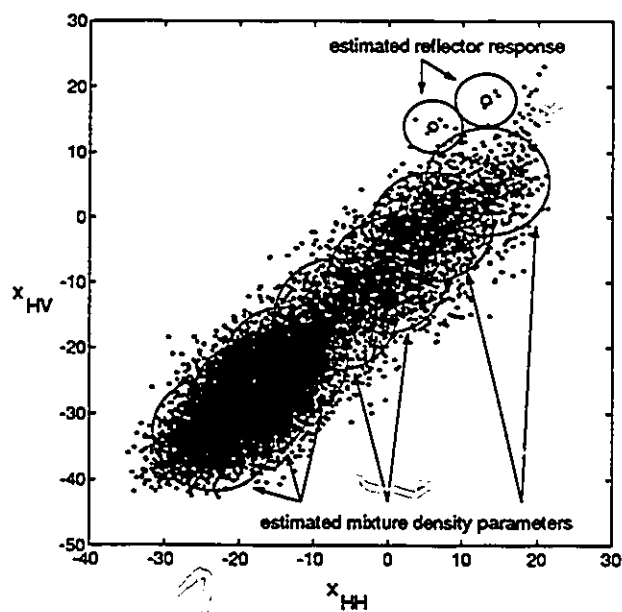


Figure 4.6: Scatter plot of training data. The components of the estimated mixture densities are superimposed.

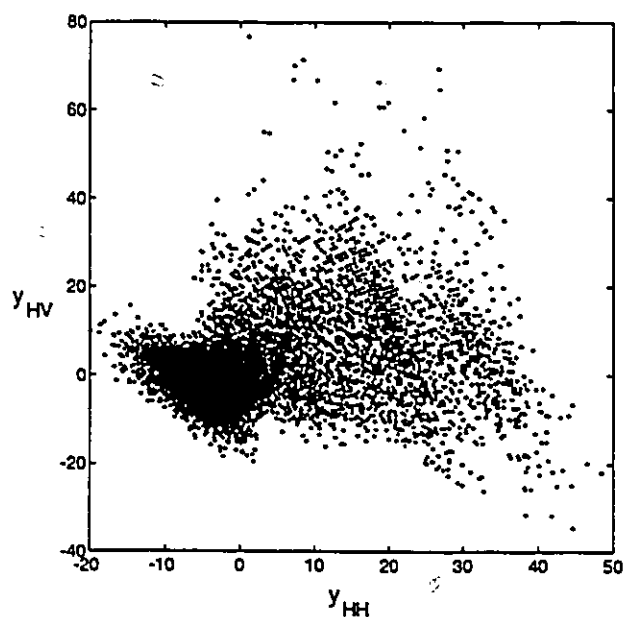


Figure 4.7: Scatter plot of output of RBF network.

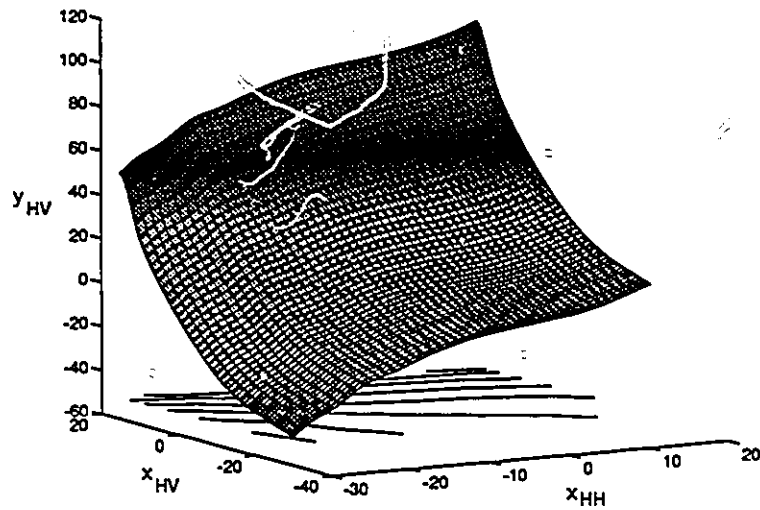
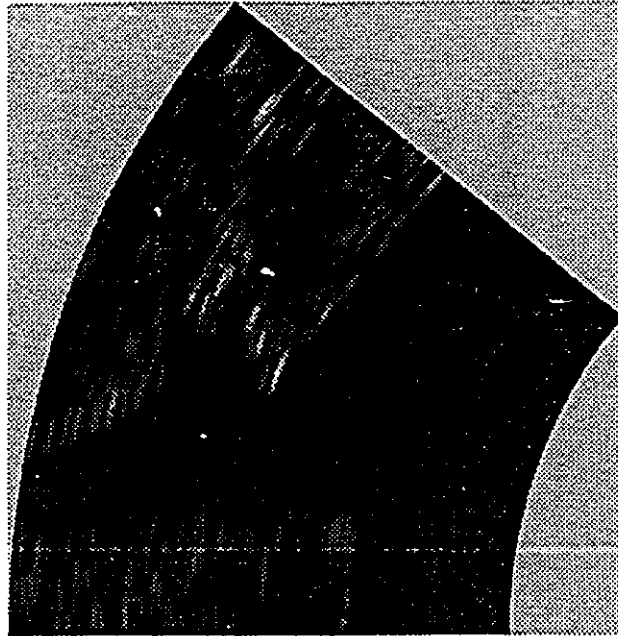


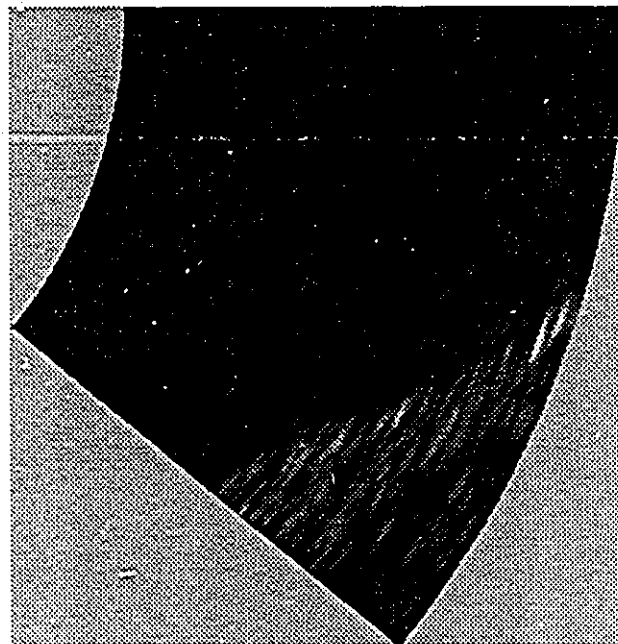
Figure 4.8: Surface plot of nonlinear transformation learned by the RBF network.

	Dofasco	La Salle park
target ( $\hat{\mu}_t, \hat{\sigma}_t$ )	(84.4, 4.09)	(93.1, 6.22)
clutter ( $\hat{\mu}_c, \hat{\sigma}_c$ )	(11.1, 1.58)	(10.7, 2.74)
TCR	80.4	82.4
normalized TCR	46	30

Table 4.2: Estimated parameters of RBF network processed sub-images.



Dofasco



La Salle Park

Figure 4.9: Sub-images of the RBF network processed data.



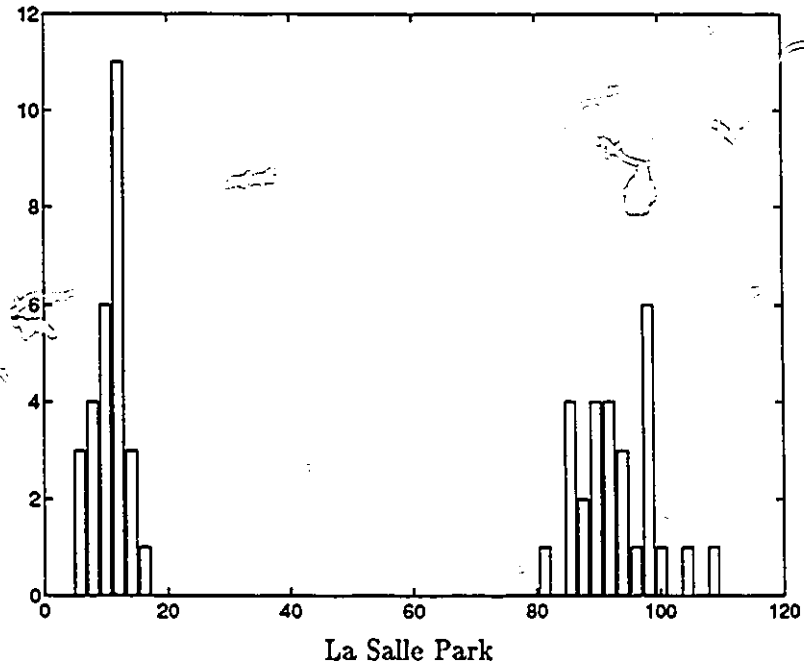
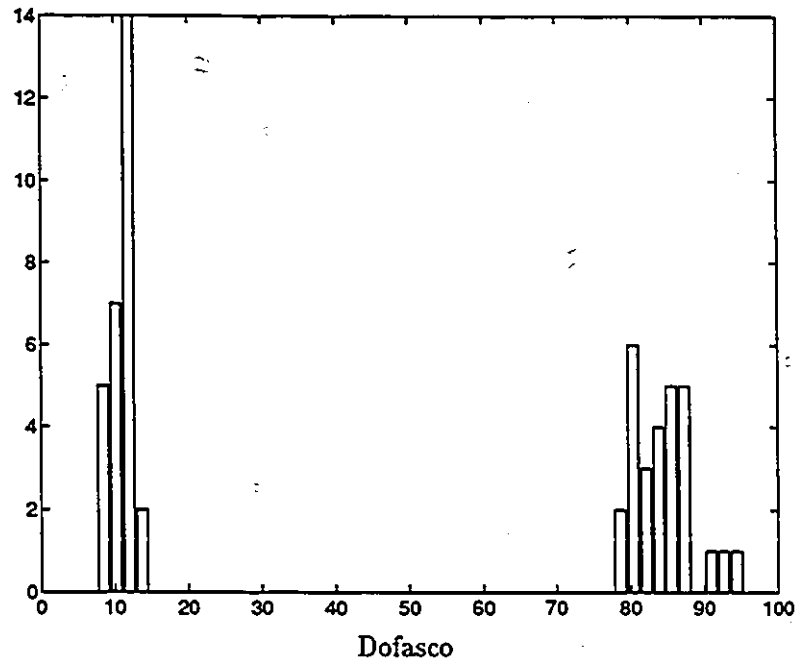


Figure 4.10: Estimated histograms of peak target and average clutter for RBF network result.

units were introduced manually in order to have a response from the target as well as the clutter. The manual introduction was necessary since the number of target samples is under-represented in the available data; a statistical learning method gives the target samples little weight, leaving the targets unrepresented. The locations of the centres is approximated from scatter plots of the target samples, and set equal to (13,18) and (6,14). The covariances are chosen to be circular, equal to  $\Sigma = \text{diag}(4, 4)$ , with a standard deviation of approximately 25% size of the clutter densities. Having adequately modeled the clutter and targets, the parameters of the two-dimensional mixture representations are projected onto both HH-pol and HV-pol axes, resulting in 18 one-dimensional RBF units. To improve the interpolation quality of the network, a factor of  $\alpha = 0.01$  is applied to the clutter spread parameters.

The next step is the mutual information training to learn the weights. A subsampled data set from Dofasco and La Salle park regions is used. The data set is the same as shown in the scatter plots, with the same area coverage as the sub-images, except subsampled in range by a factor of 4 and in azimuth by a factor of 10. The weights are initialized to give the same mapping as the linear network. The constrained optimization routine is used to minimize the cost function given by Eq. 4.34 subject to the constraints. After convergence, the residual mutual information is estimated to be equal to approximately 0.036 bits. The scatter plot of the output of the network is shown in Fig. 4.7. As can be observed, the data distribution is more clustered around a single point, rather than distributed over a large range, as in the scatter plot of the input data. Figure 4.8 shows the resultant nonlinear mapping learned by the RBF network. The inputs are along the x- and y-axes, and the z-axis height is the  $y_{HV}$  output.

The output of the network is processed by the CA-CFAR algorithm, as in the previous processing cases. The resultant sub-images in Fig 4.9 show much enhanced target visibility, in both Dofasco and La Salle park areas. The clutter is generally well suppressed. However, some false targets are visible as well. The histogram data in Fig. 4.10 show good separation between target and clutter distributions. The statistics in Table 4.1 verify the higher visibility of the target. The normalized TCR values are the highest of all the individual methods considered thus far, for both Dofasco and La Salle Park areas.

#### 4.4 Summary

The unsupervised training of linear and nonlinear networks with information-theoretical measures is investigated. The principle of minimizing mutual information between the outputs is used to separate the clutter from the desired targets in a non-Gaussian pdf. For the case of a linear network, it is shown that this condition is equivalent to decorrelating the output using PCA techniques. A nonlinear RBF network was proposed as a method by which to improve the mapping in the non-Gaussian clutter environment. The RBF network is trained using a novel hybrid method, where the hidden layer is determined using a mixture density modeling technique, and the output linear layer is learned by minimizing the mutual information cost function that is based on a Gaussian pdf assumption. Both linear and RBF networks are static once trained.

The PCA-trained linear network solution was found to be inadequate. By biasing the solution and thereby leaving a residual correlation in the data, the NTCR result is improved, but is still less than that of the ACPIC result. Next, the RBF hidden layer was trained on clutter data, and RBF functionals were added to represent the target response as well. A constrained optimization routine was then used to train the output linear layer to minimize the mutual information functional, resulting in a residual mutual information of 0.036 bits. The sub-images show an enhanced target and reduced clutter, which is verified by high NTCR values.

A disadvantage of using the RBF network, and nonlinear networks in general, is the manifestation of local minima. With linear networks, there is a guarantee of a single, global maxima or minima. Not so with nonlinear networks. The experience gained training these networks has shown that the more *a priori* information is used to design and train the network, the less the probability of converging to a local minima solution.



## Chapter 5

# Modular neural network

In the previous two chapters, various adaptive and neural network solutions have been proposed to combine the HH-pol and HV-pol radar images in order to enhance the cross-polar performance of a precise radar navigation system. The solutions employ learning network parameters from training samples, based on unsupervised principles. In this chapter, a non-learning modular network approach is presented that combines the two learning-based networks to produce a result that is better than either network used on its own. A non-learning method is defined as a method that uses information other than that contained in the training samples [28].

### 5.1 Network design

For a modular network to perform better than its parts, each sub-network must provide some independent information. Two processing methods discussed in previous chapters which meet this criterion are the adaptive cross-polar interference canceller and the RBF network. The ACPIC is a linear network, capable of adapting to the cross-polar variations in the clutter environment. It functions well under conditions of varying clutter power; however, it does not suppress clutter as well the RBF network. The RBF network, on the other hand, provides a stationary nonlinear mapping that enhances the cross-polar performance. It provides an excellent enhancement of cross-polar reflectors; however, it also enhances naturally occurring cross-polar clutter point targets. Judging from a subjective inspection of the two radar images produced by these two methods, and their operation, it is hypothesized that a modular network should capture the desirable characteristics of both these networks.

Figure 5.1 is a diagram of the modular network. After the data is processed by the respective methods, the results are normalized (based on the estimated histogram) making the data ranges approximately the same. The normalization is such that

$$\sum_{i=1}^N \tilde{n}(i) = N_t, \quad (5.1)$$

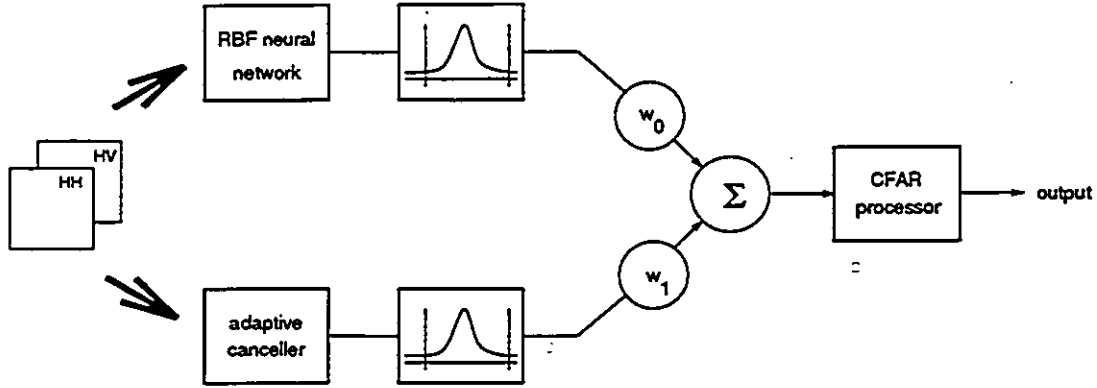


Figure 5.1: Modular neural network.

	Dofasco	La Salle park
target ( $\hat{\mu}_t, \hat{\sigma}_t$ )	(2.06, 0.10)	(2.68, 0.18)
clutter ( $\hat{\mu}_c, \hat{\sigma}_c$ )	(0.522, 0.034)	(0.556, 0.067)
TCR	1.54	2.12
normalized TCR	46	32

Table 5.1: Estimated parameters of modular network processed sub-images.

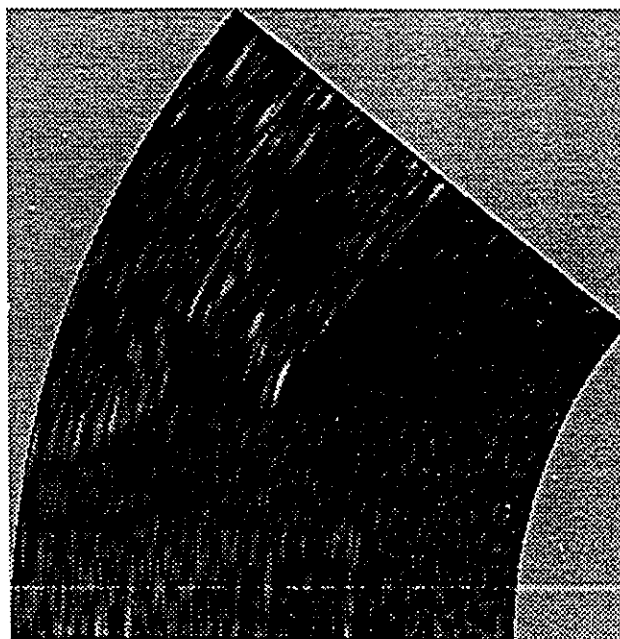
$$\sum_{i=1}^{n_b} \hat{n}(i)/N_t \simeq 0.02, \quad (5.2)$$

$$\sum_{i=n_w}^N \hat{n}(i)/N_t \simeq 0.02, \quad (5.3)$$

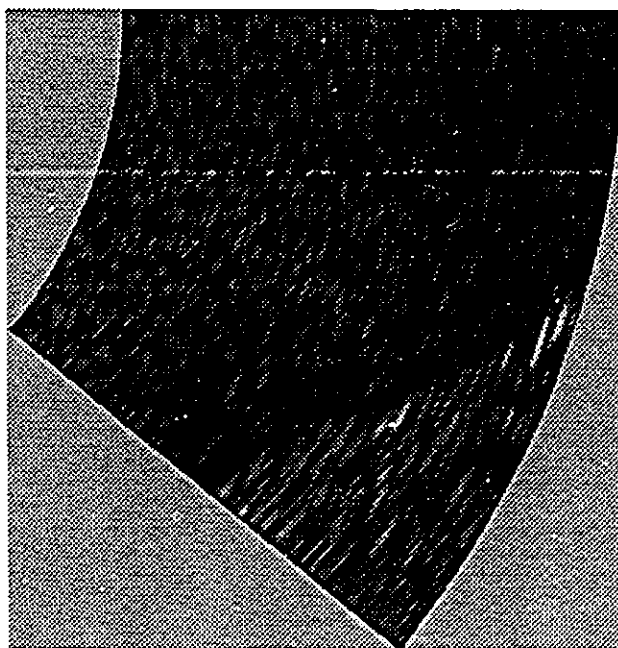
where  $\hat{n}(i)$  is the estimated histogram,  $N$  is the total number of histogram bins,  $n_b$  is the lower (black) 2% bin, and  $n_w$  is the higher 2% bin (white) bin. Based on the  $n_b$  and the  $n_w$  values, the data are scaled to the  $[0,1]$  interval. The normalized data is then weighted and summed together, and the result processed by the CA-CFAR algorithm. The un-informed choice for the weights is to set them to be equal, and so they are both set to a value of 0.5.

## 5.2 Experimental results

The sub-images in Fig. 5.2 show an example of the resultant output from the modular network. The images retain desirable characteristics of both the individual processing techniques, suppressing both average and peak clutter while enhancing the target. Figure 5.3 shows the corresponding histograms of the average clutter and peak target over the 28 scans. The estimated normalized TCR in Table 5.1 shows an improvement for the La



Dofasco



La Salle Park

Figure 5.2: Sub-images of modular network processed data.

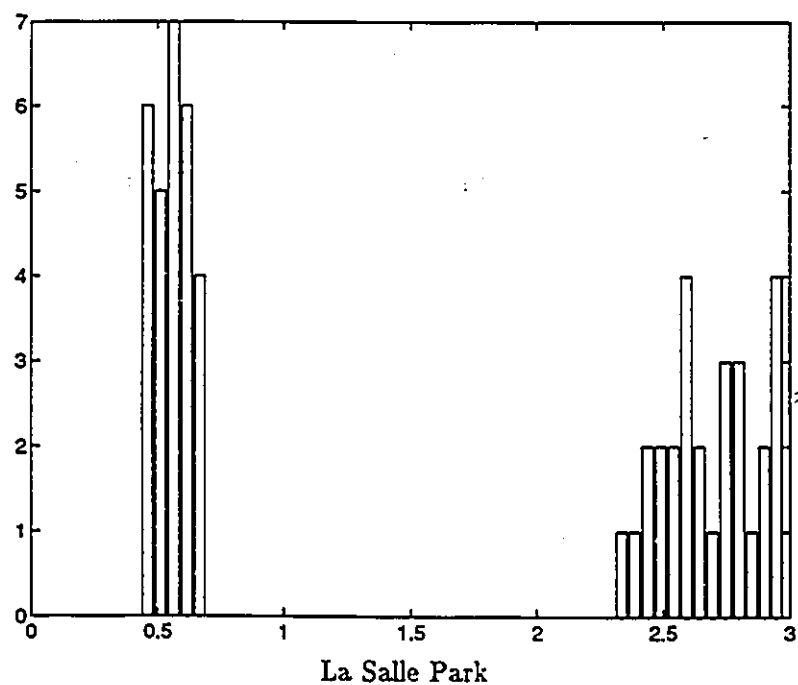
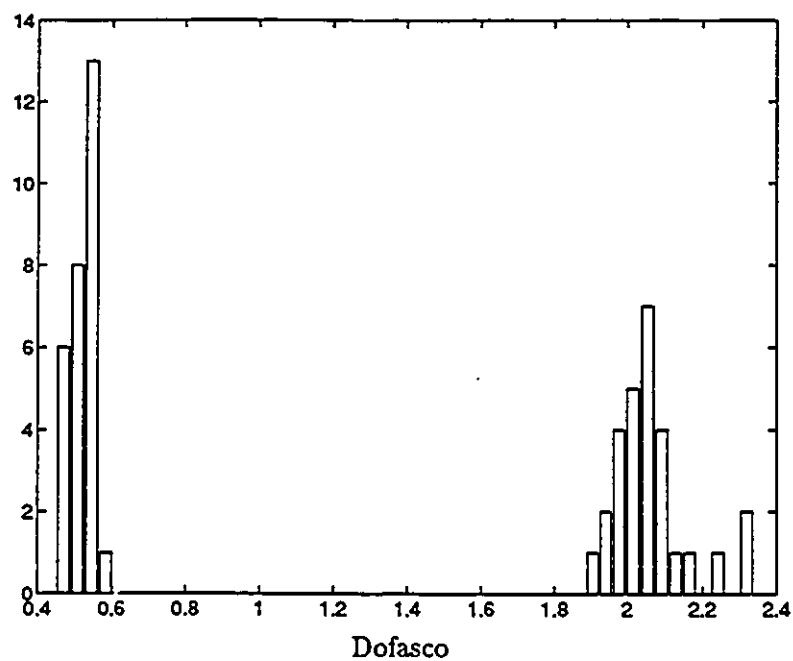
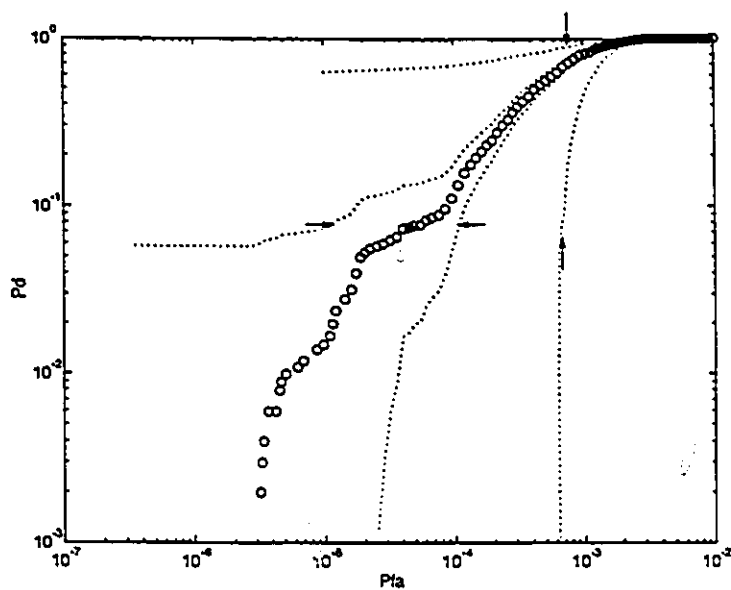
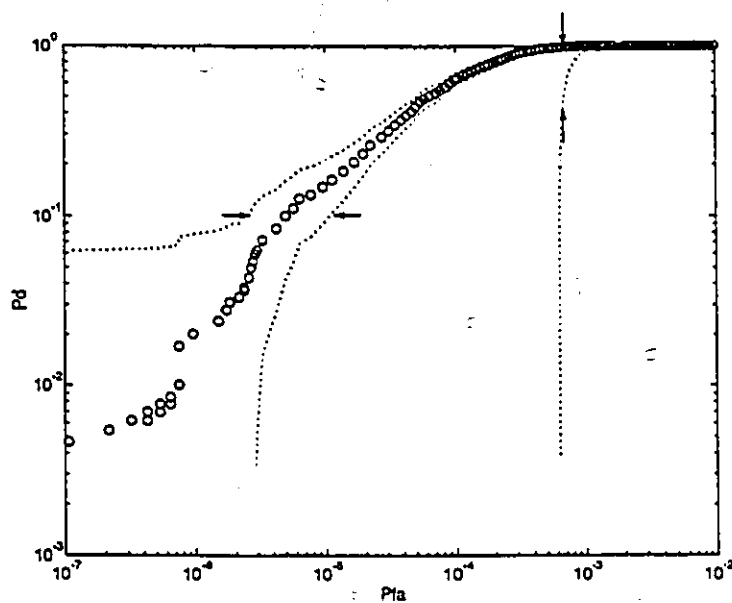


Figure 5.3: Estimated histograms of peak target and average clutter of the modular network processed data.



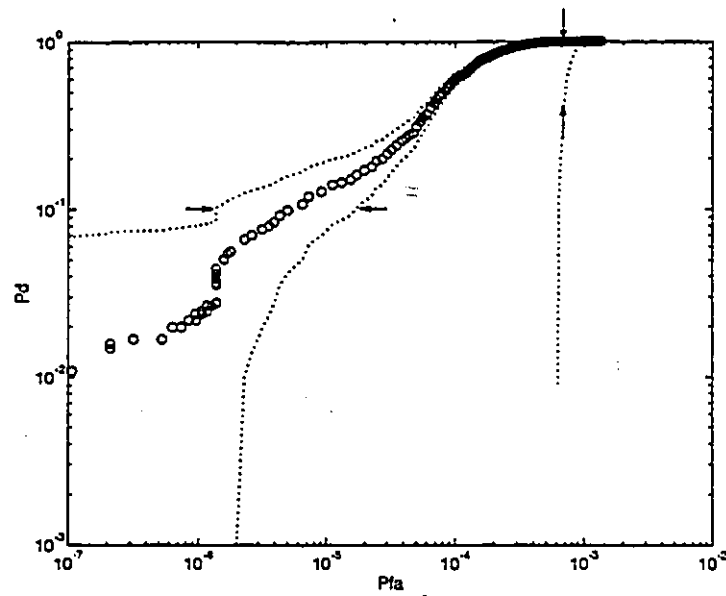


Dofasco

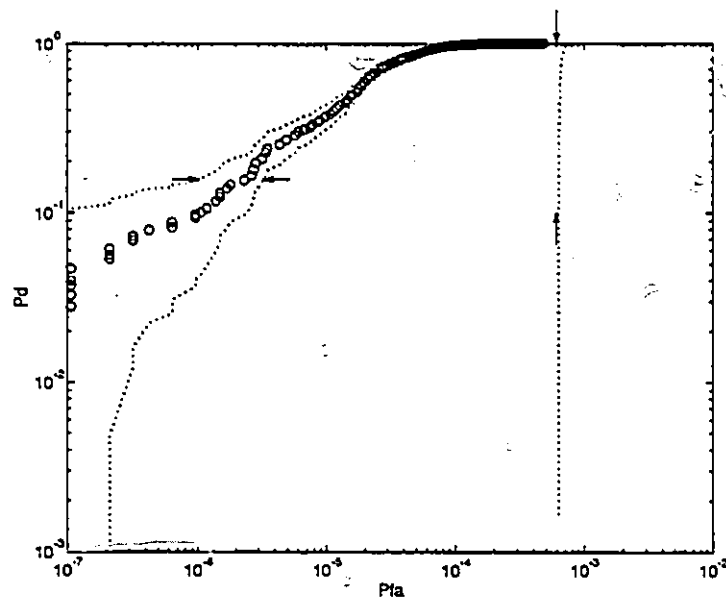


La Salle Park

Figure 5.4: Estimated receiver operation curves for the adaptive interference canceller network output.

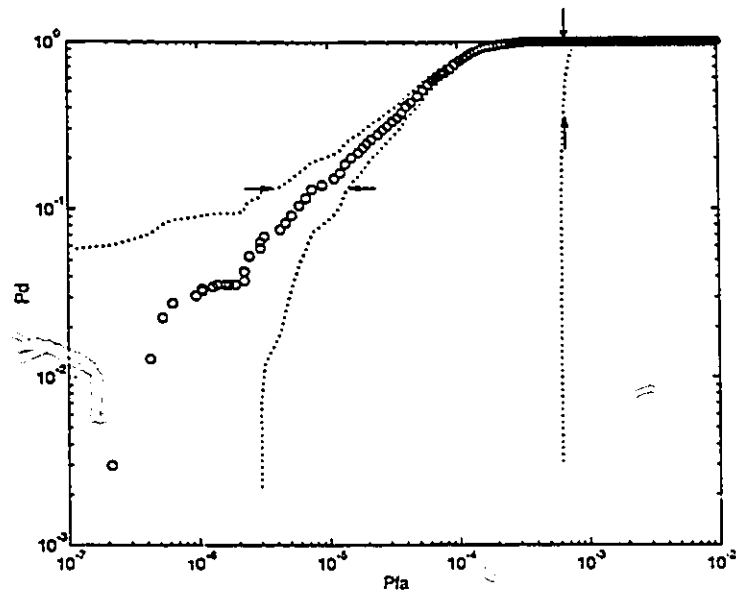


Dofasco

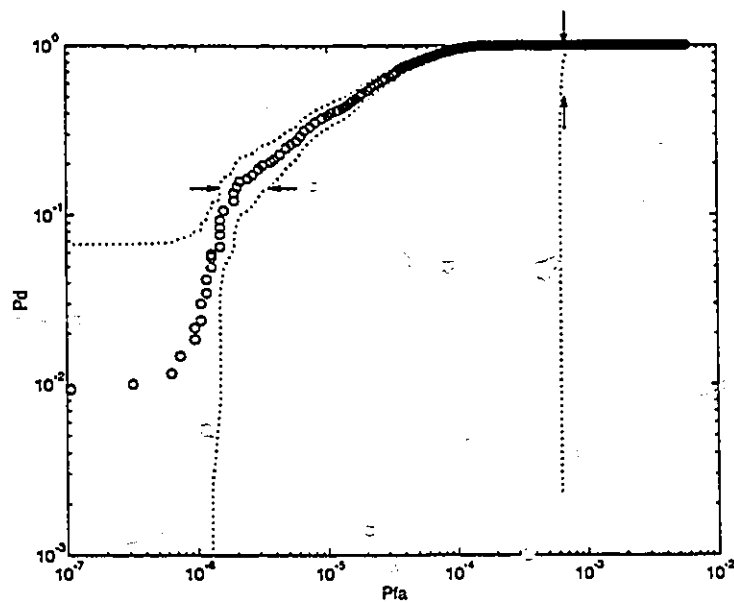


La Salle Park

Figure 5.5: Estimated receiver operation curves for RBF network output.



Dofasco



La Salle Park

Figure 5.6: Estimated receiver operation curves for modular network result.

Salle Park area, while the value for the Dofasco area stayed essentially constant. It is likely that no further improvement is possible in the Dofasco area in terms of the average clutter performance.

The normalized TCR was introduced as a measure useful for quantifying the visibility of the target against the average background clutter. A new measure is now introduced, namely the estimate of the receiver operating characteristic (ROC), which plots the estimated probability of detection against the estimated probability of false alarm for a particular processor. The ROC is reflective of the suppression of peak clutter phenomenon, which drives the false alarm rate. A thorough statistical analysis for estimating the ROC requires many independent data sets containing target and clutter. Unfortunately, this experiment limits the analysis to a single scene averaged over 28 scans. Proceeding with this limitation in mind, the ROC's are plotted for the adaptive interference canceller network in Fig. 5.4, for the RBF network in Fig. 5.5, and for the modular network shown in Fig. 5.6. The dotted lines show the 90% confidence intervals for the estimated probability of detection, and false alarm. The computation of these confidence intervals is described in Appendix C. The number of target samples is low; accordingly the graph to the left of the dotted line is regarded as not statistically significant. However, the overall trends indicated in the graph still provide useful information.

As can be observed from these plots, the ROC for the modular network shows an improvement for the Dofasco area, yet no improvement is noted for the La Salle Park area. This is in contrast to the NTCR estimates which indicated improvement in the La Salle Park area but not in the Dofasco area. The average visibility is increased in the case of the La Salle Park area, and the peak clutter that is responsible for false alarms is reduced in the Dofasco area (as suggested by the ROC plots). This shows that the modular network is able to integrate the performance aspects of both networks to give an improved overall result.

### 5.3 Summary and discussion

A non-learning modular neural network is presented. From the above analysis it is clear that the modular network is able to integrate the desirable qualities from the ACPIC and RBF network methods to achieve an overall enhanced reflector result that is superior to either network alone. The estimated NTCR values and ROC plots verify that the overall average and peak clutter suppression performance has been improved. As a side benefit, the modular network should also be more robust in operation, since the network would continue to function even if there was a complete failure of one of the network sub-modules.

In this presentation the modular network was described as non-learning, and a knowledge-based heuristic argument was given to justify summing of the individual network module outputs. Modular network weights can also be learned by minimizing a cost function, as is commonly used in feature extraction tasks. For example, weights computed from a principal component analysis (PCA) could be used to combine the outputs to produce a maximum (or minimum) variance projection of the data.

Finally, rather than summing the outputs of the individual network modules, another

option is to choose the network result with minimum output. This operation is related to the fuzzy set intersection operator, where the fuzzy intersection between two fuzzy sets is the minimum value between the two fuzzy measurement functions [64]. In practice, it was found that the result of using the minimum operation was similar to that of using the simpler summing function. The use of minimum (or maximum) operators is mentioned here since a competitive learning algorithm could be constructed based on which module provided the best operation for a particular type of training input.



## Chapter 6

# Post-detection processing

### 6.1 Motivation for post-detection processing

The radar environment contains various forms of clutter, both natural and man-made, which may have high cross-polar radar returns. This type of clutter causes false alarms, reducing the overall performance of the detection system. Up to this point, the processing has not made use of any *a priori* information about the target location. *A priori* information about the target position will now be used in a post-detection processor to reduce the false alarm rate to a very small number.

There is one observation that can be readily made about the location of a reflector target. The reflector must be visible to ships navigating the confined waterway, and is therefore assumed to be located near an unobstructed water-land interface. Although other choices further inland are possible, natural and man-made obstructions are more likely to limit target visibility, and therefore make these locations a poor choice, in general. It is assumed that the reflector will always be located at a preferred location near the water-land interface, and therefore detections which are distant from this boundary can be discounted as likely to be false alarms.

Another observation about the reflector target position is that the locations chosen for the reflectors would not be adjacent to an area containing clutter with high cross-polar radar returns. It is perceived to be an easy task to ensure that the reflectors are located in an area where cross-polar clutter is minimal, since this is under the control of the installers of the navigational system.

The post-detection processor described in this chapter is designed to combine *a priori* location information along with the primary detection results, thus giving an improved final detection result. In this manner, false alarms can be virtually eliminated.

### 6.2 Description of the approach

Figure 6.1 is a block diagram of the stages in the post-detection process. The output of the HH-pol and HV-pol modular network processing stage is presented to a threshold detector.

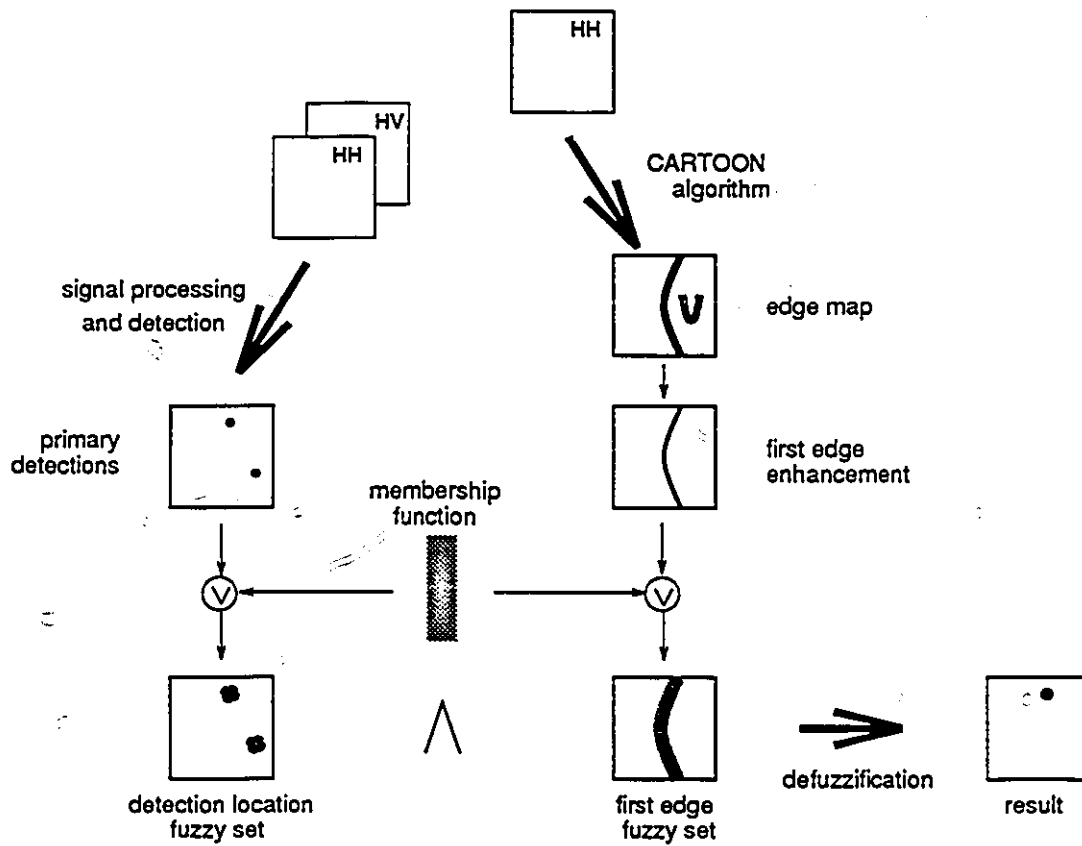


Figure 6.1: Block diagram of post-detection processing.



The output of the threshold detector is a binary map of the location of the detections. If the threshold is set sufficiently low, both targets and false alarms are included in the set of detections. The water-land interface of interest is determined automatically using a vision-based edge detection algorithm, known as the CARTOON algorithm [58]. The algorithm is tuned to the radar environment, accepting the HH-pol radar image as input and producing an edge map at the output.

### 6.2.1 The CARTOON algorithm

A block diagram of the CARTOON algorithm is shown in Figure 6.2. The basis of the algorithm is the detection of zero-crossings of an image after being filtered by the Laplacian operator

$$\nabla^2 G(x, y), \quad G(x, y) = e^{-\frac{1}{2}(x^2/\sigma_x^2 + y^2/\sigma_y^2)}. \quad (6.1)$$

The location of the zero-crossings correspond to edges in the image. This Laplacian operator is discussed in detail by Marr[46]. In general, the operator is chosen to be circularly symmetric. The algorithm was generalized in this particular application to use elliptically symmetric Gaussian operators, since the resolution of the radar image is generally different in range and in azimuth. The Laplacian of the Gaussian operator (normalized) is therefore

$$\nabla^2 G_n(r) = (1 - \frac{r^2}{2})e^{-\frac{1}{2}r^2}, \quad r^2 = \frac{x^2}{\sigma_x^2} + \frac{y^2}{\sigma_y^2} \quad (6.2)$$

The parameters of the CARTOON algorithm need to be adjusted to match the resolution of the radar system, and the scale of the desired edge map. The masks need to be chosen to be fine enough to preserve the desired detail in the edges, yet coarse enough so that noise and small objects do not get recognized as edges. The scale was purposefully chosen so that small objects, such as ships, do not get detected as edges. For the fine mask, parameters  $\sigma_x = 6$  and  $\sigma_y = 24$ , and for the coarse mask, parameters  $\sigma_x = 12$  and  $\sigma_y = 48$  are used. The Gaussian smoothing mask used is chosen to be half the size of the fine mask, so that  $\sigma_x = 3$  and  $\sigma_y = 12$  for the operator.

The CARTOON algorithm makes use of the fine and coarse operator masks to achieve a robust edge map. After filtering with the masks, the positive and negative bitmaps are AND'ed together, and then smoothed by a Gaussian mask. The smoothed bitmaps are then AND'ed together. Only edges that are common to both fine and coarse filtered bitmaps appear in the final output.

Figure 6.3 shows the results for the scenes of interest. Note the false edge artifacts found in the La Salle Park image. These are due to the finite support of the image, and do not pose a serious problem. They can simply be ignored since the the likelihood of false alarms as a result of sea clutter in a confined waterway is extremely low. In practice, we need only choose an image slightly larger than that required to avoid these artifacts.

Since we are only interested in the first water-land interface, the edge map produced by the CARTOON algorithm is presented to a "first-edge" detector, which responds to the first edge it finds along each radar sweep; the resulting edge map is shown in Fig. 6.4.

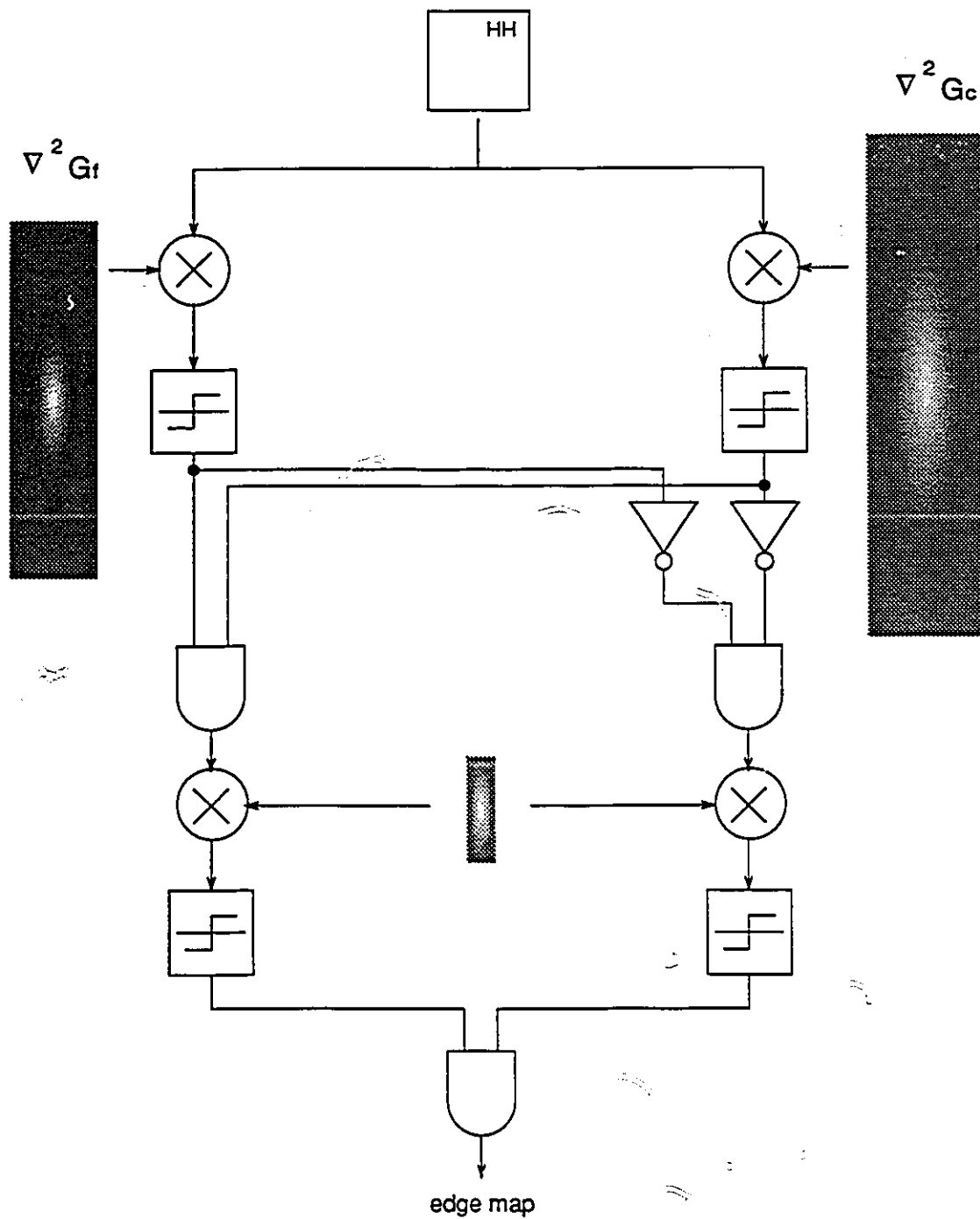


Figure 6.2: Block diagram of the CARTOON algorithm.

### 6.2.2 Fuzzy detection processing

Fuzzy set theory is next used to combine the two pieces of information, specifically, that of detection locations and first-edge locations. The intersection of these two fuzzy sets effectively combines the detections with the edge information, resulting in a greatly reduced false alarm rate.

The crisp set of primary detections is fuzzified by choosing a Gaussian form for the measurement function of the location of the detection. In a similar fashion, a Gaussian form for the measurement function is used to specify the degree of "edginess" at a particular location in the radar image. This is done by superimposing a Gaussian function at each pixel in the corresponding detection and edge images. The two dimensional Gaussian measurement function is centred on each white pixel. Since adjacent pixels will cause the measurement functions to overlap, the fuzzy union operator is used to combine these subsets. Explicitly, we have

$$\mu_G(x, y) = \vee_i \mu_F(x - x_i, y - y_i), \quad (6.3)$$

where  $x_i$  and  $y_i$  are the locations of the non-zero pixels in the radar images, and the fuzzy union operator

$$\vee_i \mu_F(x_i, y_i) = \max_i \mu_F(x_i, y_i) \quad (6.4)$$

is defined as being equivalent to finding the maximum value over the set of overlapping measurement functions at the image location  $(x, y)$  [64].

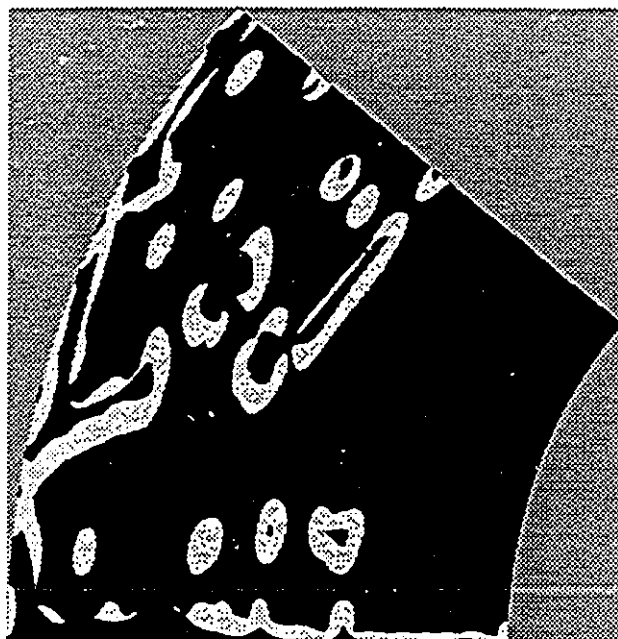
We are interested in the case where a detection is the vicinity of an edge, or in other words, when a target and an edge are present together. It follows that the desired resultant set can be found by taking the intersection of the fuzzy set of detections with the fuzzy set of image edginess, such that

$$\mu_H(x, y) = \mu_{Gd}(x, y) \wedge \mu_{Ge}(x, y), \quad (6.5)$$

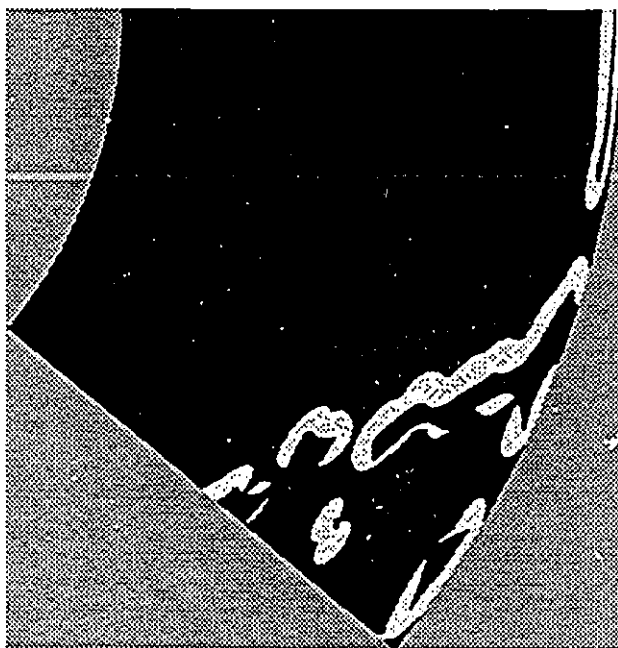
which is equivalent to determining the minimum value between the two sets at each  $(x, y)$  location [64]. Finally, since we are interested in a binary result, we need to defuzzify the set. A threshold is chosen in order to make the set of post-detections crisp, or in other words, binary valued. The final binary result contains only detections that are near edges, which should be our reflector targets. Since edges (as defined in this section) generally occupy a small percentage of the total area of interest, this post-detection processor greatly reduces the probability of false alarm.

## 6.3 Example of post-detection processing

To demonstrate the operation of the post-detection processor, a threshold level was chosen for the primary detection stage such that the false alarms would be present in the output. The fuzzified detections and edges are shown in Figs. 6.5 and 6.6, respectively. The final post-detection results after fuzzy processing are shown in Fig. 6.7, where they are superimposed on a reduced intensity HH-pol image as a guide to the location of the



Dofasco



La Salle Park

Figure 6.3: Binary edge maps produced by the CARTOON algorithm.



Dofasco



La Salle Park

Figure 6.4: Result after radially processed first edge detection.

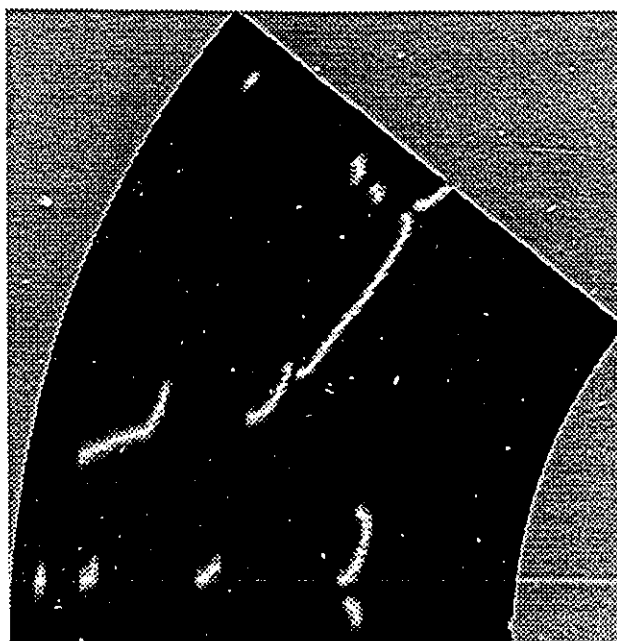


Dofasco



La Salle Park

Figure 6.5: Gaussian measurement function applied to detections.



Dofasco

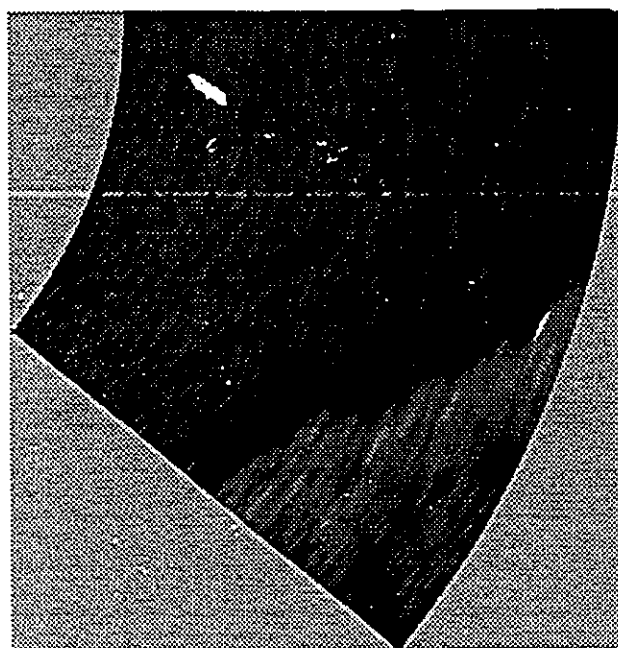


La Salle Park

Figure 6.6: Gaussian measurement function applied to edges.



Dofasco



La Salle Park

Figure 6.7: Final post-detection result. The original HH-pol image is superimposed as a visual aid.



detections. The false alarms present after primary detection have been effectively removed, leaving only the targets of interest; this is a significant engineering accomplishment.

Only the first-edge areas are considered suitable locations for the reflector targets. As long as this assumption holds true, it is obvious that the false alarm rate is reduced by the factor of first edge area over the total area of interest. Since the first-edge areas are estimated to be approximately 10% of the total sub-image land clutter area, the false alarm is reduced by a factor of 10 or more.

## 6.4 Implementational issues

The entire post-detection process can be implemented using a neural network architecture, consisting of radial basis functions, tapped-delay lines, weights, and simple thresholding devices.

The CARTOON algorithm requires 2-dimensional convolvers, threshold devices, and logic devices arranged in the fashion described in Fig. 6.2. A 2-dimensional convolver may be constructed from parallel tapped-delay lines, with the weights programmed with the desired mask values. It has been shown that the Laplacian operator can be approximated by a difference of Gaussians (DOGs) [46]. Therefore, a 2-unit RBF network can be used to implement the DOG. Likewise, the Gaussian mask used for smoothing can also be constructed using single RBF function. The simple AND and inverting logic functions are easily constructed using appropriate weights and a threshold unit.

As shown by Jang and Sun [29], a fuzzy decision system can be implemented by an RBF neural network. The measurement functions can be constructed using a single RBF unit. Minimum and maximum functions have been constructed using neural networks with feedback connections. A simple threshold device can perform the defuzzification, by mapping the fuzzy values to a crisp binary value.

The intent here is not to give a detailed implementation, but merely to point out that it is indeed feasible to implement the post-detection processor using simple analog components in a neural network type of architecture. This is an advantage in radar signal processing, since high bandwidths and data rates limit the amount of digital signal processing that can be accomplished.

## 6.5 Summary

A post-detection processor was described that makes use of *a priori* information about the reflector target locations to reduce the false alarm rate significantly. This is accomplished by combining primary detection results with the location of the water-land boundary, where it is known that the reflectors should be located. The location of the water land boundary is determined automatically using the CARTOON algorithm, modified to work in the radar environment.

An example scenario is described with each stage of the post-detection process displayed. After edge detection, a first-edge detector removes all edges except those at a water-land

boundary. A fuzzy set processor applies a Gaussian measure function to the edge and primary detections, and then combines the results with an intersection operator. After making the results crisp, it is shown that only the reflector locations remain. Since only the water-land boundary areas are considered valid locations for detectors, the false alarm rate is greatly reduced.

Finally, a neural network architecture is suggested for implementing the post-detection processor.

specially modified to perform with radar resolutions. The fuzzy set reasoning combines the edge information corresponding to the water-land boundary with primary detection results to remove false targets. A demonstration using example images successfully eliminates false targets from the image, leaving only the desired reflector target locations.

The entire signal processing and detection system is implementable with relatively simple analog processing elements. The novel analog hardware implementation of a wide bandwidth design of the adaptive cross-polar interference canceller was granted Canadian and U.S. patents.

## 7.2 Contributions of the thesis

- First direct digital data recording of full scan radar data in the field (dual-channel) at McMaster University, including the design and construction of support hardware to achieve the desired goal.
- Plan and design of a radar field experiment, including making special modifications to the commercial radar receiver to improve data integrity, and thereby increasing IF dynamic range.
- Development of real-time software to acquire data from a digital tape recorder to microcomputer.
- Canadian and U.S. patents obtained for the adaptive cross-polar interference canceller based on simple, robust, analog implementation; operation studied and quantified by digital simulation.
- Prior to the development of the ACPIC, no established methods existed for the enhancement of twist-grid retroreflectors.
- Demonstration of application of neural network techniques to nonlinear signal processing, representing one of the first publications of this fact.
- First dual-channel polarimetric processing documented using neural networks.
- Demonstration of superior modeling performance of extended metric expectation maximization algorithm clustering for choosing hidden layer parameters of an RBF neural network in signal processing problems, which is important for finding minimal configuration RBF networks.
- Development of novel neural network structure for the unsupervised learning of nonlinear projections, based on minimizing mutual information content of data.
- A unique modular network approach that successfully combines the desirable properties of various signal processing blocks to achieve a superior target enhancement.
- Vision-based image processing edge detector modified to work at radar resolutions.

## Chapter 7

# Conclusions

### 7.1 Summary of results

The objective of this thesis was to demonstrate the successful enhancement and detection of a cooperative cross-polar target. The estimated normalized target-to-clutter ratio results for the signal processing methods are summarized in Table 7.1. Each of the individual processing methods has a distinct character. The CA-CFAR processor uses a two dimensional local estimate of clutter to achieve a constant false alarm rate performance at the output. The ACPIC processor reduces clutter in a non-stationary clutter environment. The RBF network uses a nonlinear mapping to overcome the non-Gaussian nature of clutter statistics and provides a superior target enhancement. By integrating the desirable characteristics of these sub-network solutions into a modular network structure, a final average (and peak) clutter suppression performance is achieved that is better than any one of the methods used by itself. The resultant enhanced images are presented to the operator, as well as to the primary threshold detector.

The post-detection stage strives to imitate human reasoning. It successfully incorporates *a priori* information about the context of the waterway and the likely location of the radar reflectors. The solution involves a novel combination of a vision-based image processing technique and a fuzzy processor. The vision-based edge detection algorithm, CARTOON, is

Type of processor	NTCR	
	Dofasco	La Salle Park
CA-CFAR	16	7
ACPIC / CA-CFAR	35	29
RBF net / CA-CFAR	46	30
modular / CA-CFAR	46	32

Table 7.1: Summary of NTCR performance of signal processors.

- Introduction of a novel post-detection strategy incorporating *a priori* information about reflector locations along the water-land boundary of a waterway to reduce false alarms.



## Appendix A

# PRAN system specifications

### A.1 Radar system

#### Modified RACAL-DECCA RM1229 transceivers

Transmit frequency	9.488 GHz
Peak power	25 KW
Pulse width	50 nS
Pulse repetition frequency	3400 Hz
Receiver bandwidth	15 MHz

#### Kevlin 2204 2-channel rotary joint

Channel isolation	50 dB
-------------------	-------

#### Andrew PXL4-107ST 4-ft. dual-polarized parabolic antenna

Dual-polarized linear feed	
Beamwidth	1.6 degrees
Gain	38.5 dBi @ 9.4 GHz
Cross-polar discrimination	25 dB
Scan rate	28 RPM

## A.2 Sampling system

sampling frequency	30 MHz
quantization	linear, 8 bit
range offset	320 samples
range swath	520 samples
azimuth position encoder	12 bit



## Appendix B

# Calibration of radar system

Figure B.1 (a) shows a block diagram of the signal path from the X-band input of the radar receiver to the digital output of the sampling system. The 75-ohm attenuators were used to control the amplitude of the video signal before it entered the sampling system.

### B.1 Radar receiver modeling

To determine the relationship between input power and video voltage, a pulse modulated X-band signal of similar parameters to that of the transmitted radar pulse was injected into the input ports of the radar receiver, as shown in Fig. B.1 (b). The resultant video voltage was monitored on an oscilloscope, and the peak voltage recorded. This procedure was carried out on both polarization channels. Figure B.2 shows the measured data points, along with a fifth order polynomial curve that was fitted to the data. As can be observed from the graph, the middle section of the response is approximately linear, while both the low and high ends become increasingly nonlinear. The video response to a large input eventually saturates.

A model is needed to fit the response curve of the radar receiver. The behavioural model discussed by Rinehart [59] provides a good fit to the logarithmic receiver. The model is given as

$$a \log_{10} \left[ (p_r + p_n) \left[ \frac{p_s}{p_r + p_s} + b \right] \right] = V_{\text{video}} \quad (\text{B.1})$$

	HH-pol channel	HV-pol channel
$a$	-0.6217	-0.4330
$b$	-7.1234	-5.0271
$p_n$	$6.3322 \times 10^{-12}$	$9.5332 \times 10^{-12}$
$p_s$	$3.5301 \times 10^{-6}$	$9.7638 \times 10^{-6}$

Table B.1: Parameter estimates for behavioural model of radar receiver.

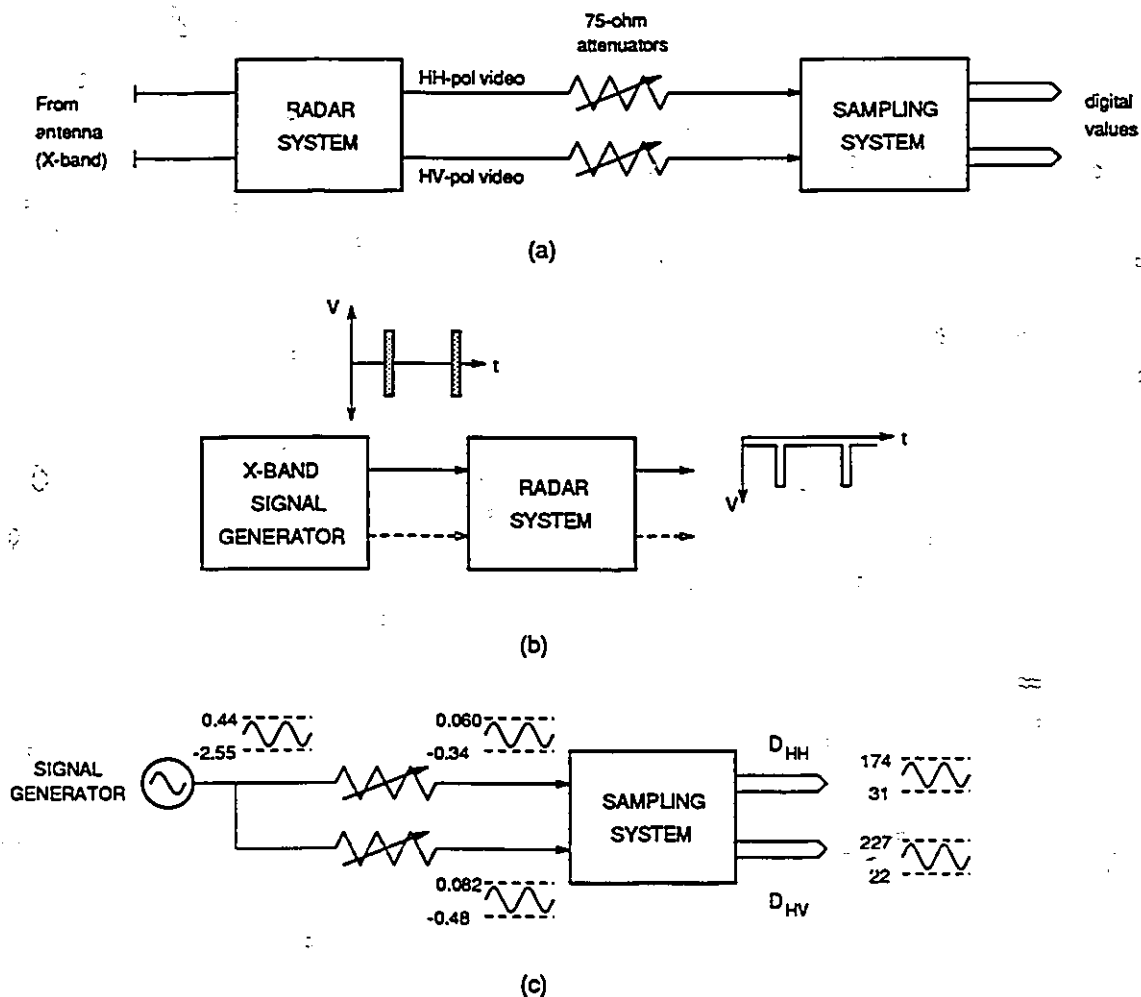


Figure B.1: (a) Block diagram of signal path in the system. (b) Radar receiver calibration. (c) Sampling system calibration.

	HH-pol channel	HV-pol channel
$m \cdot g$	-0.0208	-0.0147
$b$	1.0922	0.7701

Table B.2: Parameter estimates for linear model of the sampling system.

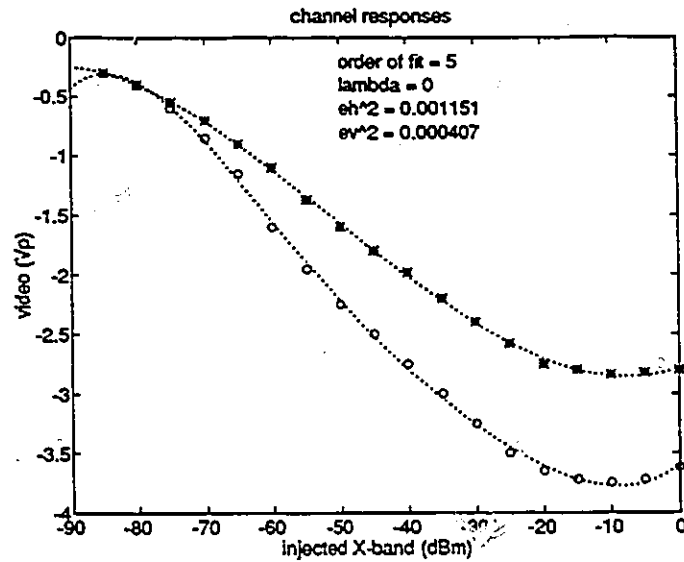


Figure B.2: Measured radar receiver calibration data.

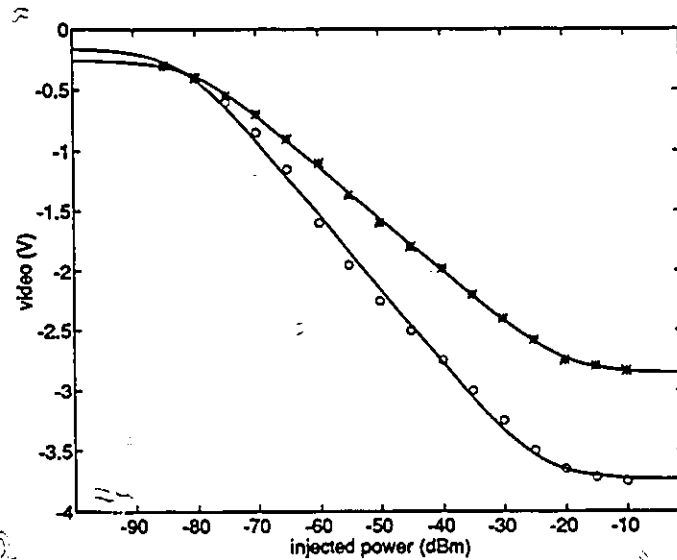


Figure B.3: Behavioural model fitted to measured radar characteristics.

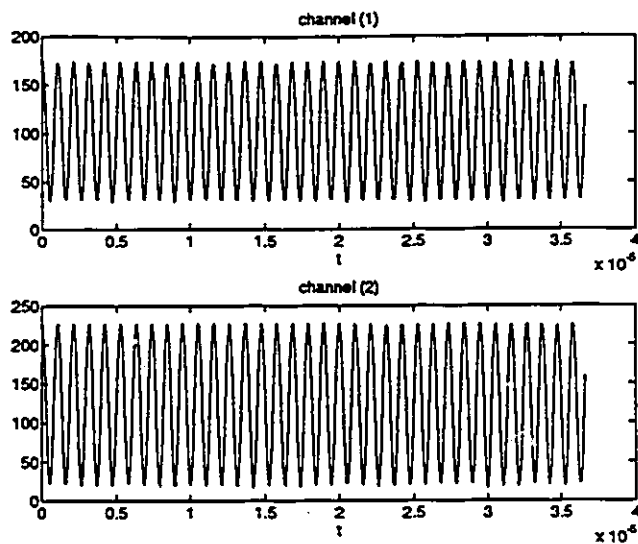


Figure B.4: Digitized sine waves used to calibrate gain.

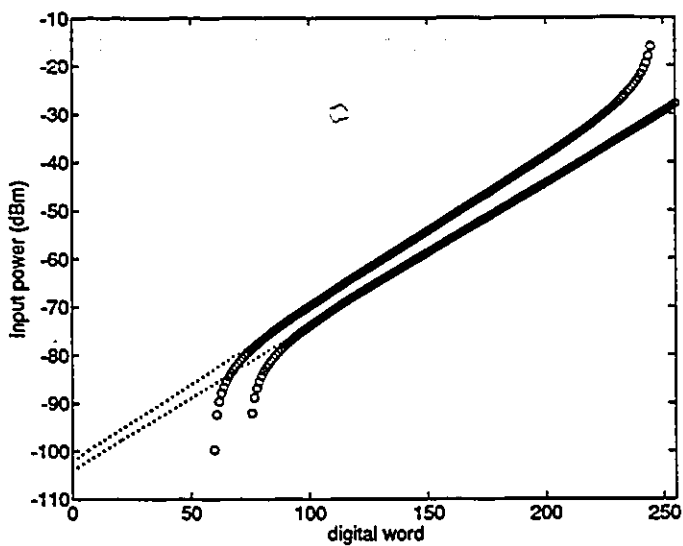


Figure B.5: Radar receiver calibration curve.

where  $p_r$  is the power input to the receiver,  $p_n$  is a noise power parameter,  $p_s$  is a saturation power parameter,  $a$  is a scaling parameter, and  $b$  is an offset parameter. The maximum likelihood (M-L) method was used to find the parameters of the model (a Gaussian density model for the noise is assumed). To achieve a good model fit, data values beyond the maximum power response point in Fig. B.2, are not used in the fitting procedure. These data points violate the monotonically increasing assumption in the model. This reduction in output voltage response with increasing input power is due to energy increasing in the harmonics of the test signal and the corresponding lessening of energy in the fundamental of the test signal. This is a common observation in systems that are driven into saturation, resulting in a decrease in output response with further increases in input. The resultant fitted curve is shown in Fig. B.3. The estimated parameters for both channels are summarized in Table B.1.

## B.2 Sampling system modeling

The block diagram in Fig. B.1 (c) shows the manner in which the sampling system was calibrated. A signal generator was used to generate sine waves with peak amplitudes as shown in Fig. B.1 (c), and with a frequency of approximately 1 MHz (946.4 KHz). The sine waves were injected into the sampling system and recorded onto tape so that a relationship could be determined between the input voltage and the digital value produced by the A/D converter. The data was recovered from tape into the computer, and a sine wave was fitted to the data using the M-L method. It is assumed that the sine wave is in additive white Gaussian noise (AWGN). The data and the resultant fitted sine wave are shown in Fig. B.4 for both channels. Channel 1 corresponds to the HH-pol channel, channel 2 to the HV-pol channel.

A linear relationship between video voltage and recorded data values is assumed. Therefore, the relationship is given as

$$D_{HH} = \text{fix}[(m_1 \cdot g_{HH})V_{HH} + b_1] \quad (\text{B.2})$$

$$D_{HV} = \text{fix}[(m_2 \cdot g_{HV})V_{HV} + b_2] , \quad (\text{B.3})$$

where  $D$  is the recorded 8-bit digital value,  $g$  is the attenuator gain,  $m$  is the sampling system scaling parameter,  $b$  is the sampling system offset parameter, and  $V$  is the video voltage. The fix operator truncates the data to an integer value. The estimated parameters are summarized in Table B.2. The sampling system gain and attenuator gain are combined into a single parameter.

### B.2.1 Resultant calibration curve

Finally, the overall model needs to be inverted, so that given a digital value, the corresponding input power is determined. Before this can be accomplished, a decision has to be made on how to deal with the two nonlinear regions, namely the noise floor region and the saturation region.

hex	HH-pol	HV-pol	hex	HH-pol	HV-pol	hex	HH-pol	HV-pol	hex	HH-pol	HV-pol
0	-103.6	-103.3	64	-81.4	-82.9	128	-59.4	-60.6	192	-37.7	-38.8
1	-103.3	-104.9	65	-81.1	-82.6	129	-59.0	-60.3	193	-37.4	-38.5
2	-102.9	-104.6	66	-80.7	-82.2	130	-58.7	-59.9	194	-37.0	-38.1
3	-102.6	-104.2	67	-80.4	-81.9	131	-58.4	-59.6	195	-36.7	-37.8
4	-102.2	-103.9	68	-80.0	-81.5	132	-58.0	-59.2	196	-36.3	-37.4
5	-101.9	-103.5	69	-79.7	-81.2	133	-57.7	-58.9	197	-36.0	-37.1
6	-101.5	-103.2	70	-79.3	-80.8	134	-57.3	-58.6	198	-35.6	-36.8
7	-101.2	-102.8	71	-79.0	-80.5	135	-57.0	-58.2	199	-35.2	-36.4
8	-100.8	-102.5	72	-78.6	-80.1	136	-56.7	-57.9	200	-34.9	-36.1
9	-100.5	-102.1	73	-78.3	-79.8	137	-56.3	-57.5	201	-34.5	-35.7
10	-100.1	-101.8	74	-77.9	-79.4	138	-56.0	-57.2	202	-34.1	-35.4
11	-99.8	-101.4	75	-77.6	-79.1	139	-55.7	-56.8	203	-33.8	-35.0
12	-99.4	-101.1	76	-77.2	-78.7	140	-55.3	-56.5	204	-33.4	-34.7
13	-99.1	-100.7	77	-76.9	-78.4	141	-55.0	-56.2	205	-33.0	-34.3
14	-98.7	-100.4	78	-76.5	-78.0	142	-54.7	-55.8	206	-32.6	-34.0
15	-98.4	-100.0	79	-76.2	-77.7	143	-54.3	-55.5	207	-32.2	-33.6
16	-98.1	-99.7	80	-75.8	-77.3	144	-54.0	-55.1	208	-31.8	-33.3
17	-97.7	-99.3	81	-75.5	-77.0	145	-53.7	-54.8	209	-31.4	-32.9
18	-97.4	-99.0	82	-75.2	-76.6	146	-53.3	-54.5	210	-31.0	-32.5
19	-97.0	-98.6	83	-74.8	-76.3	147	-53.0	-54.1	211	-30.6	-32.2
20	-96.7	-98.3	84	-74.5	-75.9	148	-52.7	-53.8	212	-30.2	-31.8
21	-96.3	-97.9	85	-74.1	-75.6	149	-52.3	-53.5	213	-29.8	-31.5
22	-96.0	-97.6	86	-73.8	-75.2	150	-52.0	-53.1	214	-29.3	-31.1
23	-95.6	-97.2	87	-73.4	-74.9	151	-51.6	-52.8	215	-28.9	-30.7
24	-95.3	-96.9	88	-73.1	-74.5	152	-51.3	-52.4	216	-28.4	-30.4
25	-94.9	-96.5	89	-72.7	-74.2	153	-51.0	-52.1	217	-27.9	-30.0
26	-94.6	-96.2	90	-72.4	-73.8	154	-50.6	-51.8	218	-27.5	-29.6
27	-94.2	-95.8	91	-72.0	-73.5	155	-50.3	-51.4	219	-26.9	-29.2
28	-93.9	-95.5	92	-71.7	-73.1	156	-50.0	-51.1	220	-26.4	-28.9
29	-93.5	-95.1	93	-71.3	-72.8	157	-49.6	-50.7	221	-25.8	-28.5
30	-93.2	-94.8	94	-71.0	-72.4	158	-49.3	-50.4	222	-25.2	-28.1
31	-92.8	-94.4	95	-70.6	-72.1	159	-49.0	-50.1	223	-24.6	-27.7
32	-92.5	-94.1	96	-70.3	-71.7	160	-48.6	-49.7	224	-23.9	-27.3
33	-92.2	-93.7	97	-70.0	-71.4	161	-48.3	-49.4	225	-23.1	-26.9
34	-91.8	-93.4	98	-69.6	-71.0	162	-48.0	-49.0	226	-22.3	-26.5
35	-91.5	-93.0	99	-69.3	-70.7	163	-47.6	-48.7	227	-21.4	-26.0
36	-91.1	-92.7	100	-68.9	-70.3	164	-47.3	-48.4	228	-20.2	-25.6
37	-90.8	-92.3	101	-68.6	-70.0	165	-46.9	-48.0	229	-18.8	-25.2
38	-90.4	-92.0	102	-68.2	-69.6	166	-46.6	-47.7	230	-17.0	-24.7
39	-90.1	-91.6	103	-67.9	-69.3	167	-46.3	-47.3	231	-17.0	-24.3
40	-89.7	-91.3	104	-67.5	-68.9	168	-45.9	-47.0	232	-17.0	-23.8
41	-89.4	-91.0	105	-67.2	-68.6	169	-45.6	-46.7	233	-17.0	-23.3
42	-89.0	-90.6	106	-66.8	-68.2	170	-45.3	-46.3	234	-17.0	-22.8
43	-88.7	-90.3	107	-66.5	-67.9	171	-44.9	-46.0	235	-17.0	-22.3
44	-88.3	-89.9	108	-66.1	-67.5	172	-44.6	-45.6	236	-17.0	-21.7
45	-88.0	-89.6	109	-65.8	-67.2	173	-44.2	-45.3	237	-17.0	-21.1
46	-87.6	-89.2	110	-65.5	-66.8	174	-43.9	-45.0	238	-17.0	-20.5
47	-87.3	-88.9	111	-65.1	-66.5	175	-43.6	-44.6	239	-17.0	-19.8
48	-87.0	-88.5	112	-64.8	-66.1	176	-43.2	-44.3	240	-17.0	-19.1
49	-86.6	-88.2	113	-64.4	-65.8	177	-42.9	-43.9	241	-17.0	-18.3
50	-86.3	-87.8	114	-64.1	-65.4	178	-42.6	-43.6	242	-17.0	-17.3
51	-85.9	-87.5	115	-63.8	-65.1	179	-42.2	-43.3	243	-17.0	-16.3
52	-85.6	-87.1	116	-63.4	-64.7	180	-41.9	-42.9	244	-17.0	-15.0
53	-85.2	-86.8	117	-63.1	-64.4	181	-41.5	-42.6	245	-17.0	-13.3
54	-84.9	-86.4	118	-62.7	-64.0	182	-41.2	-42.2	246	-17.0	-10.9
55	-84.5	-86.1	119	-62.4	-63.7	183	-40.8	-41.9	247	-17.0	-10.9
56	-84.2	-85.7	120	-62.1	-63.4	184	-40.5	-41.6	248	-17.0	-10.9
57	-83.8	-85.4	121	-61.7	-63.0	185	-40.2	-41.2	249	-17.0	-10.9
58	-83.5	-85.0	122	-61.4	-62.7	186	-39.8	-40.9	250	-17.0	-10.9
59	-83.1	-84.7	123	-61.0	-62.3	187	-39.5	-40.5	251	-17.0	-10.9
60	-82.8	-84.3	124	-60.7	-62.0	188	-39.1	-40.2	252	-17.0	-10.9
61	-82.4	-84.0	125	-60.4	-61.6	189	-38.8	-39.9	253	-17.0	-10.9
62	-82.1	-83.6	126	-60.0	-61.3	190	-38.4	-39.5	254	-17.0	-10.9
63	-81.7	-83.3	127	-59.7	-60.9	191	-38.1	-39.2	255	-17.0	-10.9

Table B.3: Look-up table relating digital values to input power in dBm.

The measurements made at low power levels are dominated by noise in the receiver, making signal measurements below this noise floor difficult. Since there are signal components (and hence digital data values) recorded below this noise floor, some extension to the model must be made. The noise floor at the low power end of the curve is removed by projecting a straight line from the linear region of the model, below the noise floor. This is accomplished by estimating the slope and intercept in the linear portion of the curve, as shown in Fig. B.5. This makes it possible to invert the response curve in the region below the noise floor.

The saturation region is dealt with as follows. If digital values occur which are larger than the maximum saturation power value given by the response curve (due to noise or data error), they are truncated to the maximum allowed value given by the response curve.

Using this modified model, a look-up table is constructed relating the recorded digital samples to the input power at the receiver. The table consists of the digital values 0 to 255, and the corresponding input power. A numerical estimation technique is used to invert the model for each digital data point, hence determining the corresponding power. Table B.3 is the resultant look-up table used.





## Appendix C

### Confidence of the estimator

The probability of detection and probability of false alarm estimators compare the desired output of the decision device with the known class value. The estimate of the probability becomes

$$\hat{p} = n(N)/N, \quad (\text{C.1})$$

where  $n$  is the counted number of events out of  $N$  trials. As  $N \rightarrow \infty$ , the estimated probability  $\hat{p}$  converges to the true probability  $p$ . Specifically, we are interested in

$$\hat{p}_D = n_D(N_D)/N_D, \quad \hat{p}_{FA} = n_{FA}(N_{FA})/N_{FA}, \quad (\text{C.2})$$

where  $n_D$  is the counted number of detections, and  $N_D$  is the total number of possible detections for the data set. Likewise,  $n_{FA}$  is the counted number of false alarms, and  $N_{FA}$  is the total number of possible false alarms for the data set.

The confidence interval for the estimated probabilities is found using the normal approximation to the binomial distributed  $n\hat{p}$  [30]. The confidence interval is equal to

$$P[y_+ \leq p \leq y_-] = 1 - \alpha, \quad (\text{C.3})$$

where  $p$  is the true value,  $1 - \alpha$  is the confidence, and the confidence interval  $(y_+, y_-)$  is given by

$$y_{\pm} = \frac{N}{N + d_{\alpha}^2} \left[ \hat{p} + \frac{d_{\alpha}^2}{2N} \mp d_{\alpha} \left( \frac{\hat{p}(1 - \hat{p})}{N} + \frac{d_{\alpha}^2}{2N} \right)^{1/2} \right]. \quad (\text{C.4})$$

The parameter  $d_{\alpha}$  is defined by

$$\frac{1}{(2\pi)^{1/2}} \int_{-d_{\alpha}}^{d_{\alpha}} e^{-t^2/2} dt = \text{erf} \left( \frac{d_{\alpha}}{\sqrt{2}} \right) = 1 - \alpha. \quad (\text{C.5})$$

Therefore,

$$d_{\alpha} = \sqrt{2} \text{erf}^{-1}(1 - \alpha). \quad (\text{C.6})$$



# Bibliography

- [1] Suzanna Becker and Geoffrey E. Hinton. Spatial coherence as an internal teacher for a neural network. Technical Report CRG-TR-89-7, Department of Computer Science, University of Toronto, Toronto, Ont, dec 1989.
- [2] D. S. Broomhead and David Lowe. Multivariable functional interpolation and adaptive networks. *Complex Systems*, 2:321-355, 1988.
- [3] Martin Casdagli. Nonlinear prediction of chaotic time series. *Physica D*, 35:335-356, 1989.
- [4] R. Cho, S. Haykin, and T. Greenlay. Polarimetric radar for precise navigation (pran): Study of an experimental system. Prepared for the Transportation Development Centre TP 7632E, Communications Research Laboratory, McMaster University, Hamilton, Ontario, April 1986.
- [5] Thomas M. Cover and Joy A. Thomas. *Elements of Information Theory*. John Wiley, New York, 1991.
- [6] J. Croney. Clutter on radar displays - reduction by use of logarithmic receivers. *Wireless Engineer*, 33(4):83-95, apr 1956. from Schleyer's book.
- [7] M. Gherardelli D. Giuli and E. Meese. Performance evaluation of some adaptive polarization techniques. In *RADAR '82 International Conference on Radar*, pages 76-81, London, U.K., 1982. IEE.
- [8] A. P. Dempster, N. M. Laird, and D. B. Rubin. Maximum likelihood from incomplete data via the em algorithm. *Proceedings of the Royal Statistical Society*, 39:1-38, 1977.
- [9] Dominion Marine Association. An evaluation of a precise radar navigation system. Technical Report TP 2800, Transport Development Centre, Ottawa, Ontario, October 1981.
- [10] Richard O. Duda and Peter E. Hart. *Pattern Classification and Scene Analysis*. John Wiley, New York, 1973.
- [11] R. Dunn. Radar set sensitive to target shape. United States Patent No. 4,106,014, August 1978.

- [12] Eric T. Fisher. Precise navigation system. Technical report, Transport Development Centre, Ottawa, Canada, March 1984.
- [13] L. E. Franks. *Signal Theory*. Dowden & Culver, Stroudsburg, PA, Revised edition, 1981.
- [14] Andrew M. Fraser and Harry L. Swinney. Independent coordinates for strange attractors from mutual information. *Physical Review A*, 33(2):1134-1140, February 1986.
- [15] E. N. Gilbert. An outline of information theory. *American Statistician*, 12:13-19, 1958.
- [16] D. Giuli. Polarization diversity in radars. *Proceedings of the IEEE*, 74(2):245-269, 1986.
- [17] D. Giuli, M. Gherardelli, and E. Dalle Mese. Performance evaluation of some adaptive polarization techniques. In *International Conference on Radar*, pages 76-81, London, U.K., 1982.
- [18] G. B. Goldstein. False-alarm regulation in log-normal and weibull clutter. *IEEE Transactions on Aerospace and Electronic Systems*, 9(1):84-92, January 1973.
- [19] Gene H. Golub and Charles F. Van Loan. *Matrix Computations*. The John Hopkins University Press, Baltimore, Maryland, 1983.
- [20] T. Greenlay and S. Haykin. On the design of passive retro-reflectors for use with precise radar navigation systems. Technical Report 117, Communications Research Laboratory, McMaster University, Hamilton, Ontario, April 1983.
- [21] S. Haykin. Polarimetric radar for accurate navigation. *Canadian Journal of Electrical and Computer Engineering*, 17(3):130-135, 1992.
- [22] S. Haykin and A. Ukrainec. Neural networks for adaptive signal processing. In N. Kalouptsidis and S. Theodoridis, editors, *Adaptive System Identification and Signal Processing Algorithms*. Prentice Hall, New York, 1993.
- [23] Simon Haykin. *Adaptive Filter Theory*. Prentice-Hall, Englewood Cliffs, N.J., 1st edition, 1986.
- [24] Simon Haykin. *Adaptive Filter Theory*. Prentice Hall, Englewood Cliffs, NJ, 2nd edition, 1991.
- [25] Simon Haykin. *Neural Networks: A Comprehensive Foundation*. Macmillan & IEEE Press, New York, 1994.
- [26] Simon Haykin and Andrew Ukrainec. Adaptive interference canceller. U.S. Patent Number 5,027,123, June 1991.
- [27] Simon Haykin and Andrew Ukrainec. Adaptive interference canceller. Canadian Patent Number 1,310,709, November 1992.

- [28] Tomas Hrycej. *Modular Learning in Neural Networks*. John Wiley & Sons, New York, 1992.
- [29] J.-S. Roger Jang and C.-T. Sun. Functional equivalence between radial basis function networks and fuzzy inference systems. *IEEE Transactions of Neural Networks*, 4(1):156-159, January 1993.
- [30] Michel C. Jeruchim, Philip Balaban, and K. Sam Shanmugan. *Simulation of Communication Systems*. Plenum Press, New York, 1992.
- [31] I. T. Jolliffe. *Principal Components Analysis*. Springer-Verlag, New York, 1986.
- [32] R. D. Jones, Y. C. Lee, C. W. Barnes, G. W. Flake, K. Lee, P. S. Lewis, and S. Qian. Function approximation and time series prediction with neural networks. Technical report, Los Alamos National Laboratory, Los Alamos, New Mexico, December 1989.
- [33] S. Karni and G. Zeng. The analysis of the continuous-time lms algorithm. *IEEE Transactions on ASSP*, 37(4), April 1989.
- [34] Solomon Kullback. *Information Theory and Statistics*. Dover Publications, 1968.
- [35] S. Y. Kung. *Digital Neural Networks*. Prentice Hall, Englewood Cliffs, NJ, 1993.
- [36] Edward K. Lee. *PARALLEL IMPLEMENTATIONS OF THE KALMAN FILTER FOR TRACKING APPLICATIONS*. Ph.D. thesis, McMaster University, Hamilton, Ontario, Canada, 1990.
- [37] Ed Lewis, Brian Currie, and Simon Haykin. *Detection and Classification of Ice*. Research Studies Press, Letchworth, U.K., 1987.
- [38] M. Long. New type land and sea clutter suppressor. In *IEEE International Radar Conference*, pages 62-66, 1980.
- [39] D. Lowe and A. Webb. Adaptive networks, dynamical systems, and the predictive analysis of time series. In *First IEE International Conference on Artificial Neural Networks*, pages 95-99, 1989.
- [40] David Lowe. Adaptive radial basis function nonlinearities, and the problem of generalization. In *First IEE International Conference on Artificial Neural Networks*, pages 171-175, 1989.
- [41] A. Macikunas and S. Haykin. Trihedral twist-grid polarimetric reflector. *IEE PROCEEDINGS-F*, 140(4):216-222, August 1993.
- [42] Arunas Macikunas, Simon Haykin, and Terry Greenlay. Trihedral radar reflector. Canadian Patent No. 1,238,400, November 1984.
- [43] Arunas Macikunas, Simon Haykin, and Terry Greenlay. Trihedral radar reflector. U.S. Patent No. 4,843,396, June 1988.

- [44] Arunas Gabriel Macikunas. Passive polarimetric reflector for precise radar navigation. Master's thesis, McMaster University, 1985.
- [45] Arunas Gabriel Macikunas. *POLARIMETRIC RADAR FOR DETECTION OF CO-OPERATIVE TARGETS IN CLUTTER*. Ph.D. thesis, McMaster University, 1991.
- [46] David Marr. *Vision*. W. H. Freeman, New York, 1982.
- [47] D. G. Michelson. Use of circular polarization in a marine radar positioning system. In *Proceedings IGARSS'89*, volume 2, pages 932-935, Vancouver, BC, 1989.
- [48] G. Minkler and J. Minkler. *CFAR*. Magellan Book Company, Baltimore, MD, 1990.
- [49] John Moody and Christian Darken. Learning with localized receptive fields. In David Touretzky, Geoffrey Hinton, and Terrence Sejnowski, editors, *Proceedings of the 1988 Connectionist Models Summer School*, pages 133-143, San Mateo, CA, 1989. Morgan Kaufmann.
- [50] John Moody and Christian J. Darken. Fast learning in networks of locally-tuned processing units. *Neural Computation*, 1(3):281-294, 1989.
- [51] F. E. Nathanson. Adaptive circular polarization. In *Proceedings of the IEEE International Radar Conference*, pages 210-214, Arlington, VA, April 1975.
- [52] Ramon Nitzberg. *Adaptive Signal Processing for Radar*. Artech House, Norwood, MA, 1992.
- [53] Steven J. Nowlan. Max likelihood competition in RBF networks. Technical Report CRG-TR-90-2, Connectionist Research Group, University of Toronto, Toronto, Canada, February 1990.
- [54] Steven J. Nowlan. Maximum likelihood competitive learning. In David S. Touretzky, editor, *Advances in Neural Information Processing Systems 2*, pages 574-582. IEEE, Morgan Kaufmann, 1990.
- [55] E. Oja. *Subspace Methods for Pattern Recognition*. Research Studies Press, Letchworth, U.K., 1987.
- [56] Jim Orlando, Richard Mann, and Simon Haykin. Classification of sea-ice using a dual-polarized radar. *IEEE Journal of Oceanic Engineering*, 15(3), July 1990.
- [57] Richard A. Redner and Homer F. Walker. Mixture densities, maximum likelihood and the em algorithm. *SIAM Review*, 26(2):195-239, April 1984.
- [58] W. Richards, H.K. Nishihara, and B. Dawson. Cartoon: A biologically motivated edge detection algorithm. In Whitman Richards, editor, *Natural Computation*, chapter 4, pages 55-69. MIT Press, Cambridge, MA, 1988.

- [59] Ronald E. Rinehart. *Radar for Meteorologists*. Department of Atmospheric Sciences, University of North Dakota, Grand Forks, North Dakota 58202-8216, second edition, 1991.
- [60] A. Saha and J. Keeler. Algorithms for better representation and faster learning in radial basis function networks. Technical Report ACT-NN-028-90, Microelectronics and Computer Technology Corporation, Austin, TX, jan 1990.
- [61] Terence D. Sanger. An optimal principle for unsupervised learning. In David S. Touretzky, editor, *Advances in Neural Information Processing Systems 1*, San Mateo, CA, 1989. Morgan Kaufmann Publishers.
- [62] Merrill I. Skolnik. *Introduction to Radar Systems*. McGraw-Hill, New York, 2 edition, 1980.
- [63] A. A. Swartz, H.A. Yueh, J. A. Kong, L.M. Novak, and R. T. Shin. The optimal polarizations for achieving maximum contrast in radar images. NASA Contractor Report NASA-CR-183349, MIT, 1988.
- [64] Toshiro Terano, Kiyoji Asai, and Michio Sugeno. *Fuzzy Systems Theory and Its Applications*. Academic Press, San Diego, CA, 1992.
- [65] A. Ukrainec and S. Haykin. A neural network nonlinear predictor. In *International Joint Conference on Neural Networks*, pages II-622, Washington, DC, June 1989.
- [66] A. Ukrainec and S. Haykin. Application of unsupervised neural networks to the enhancement of polarization targets in dual-polarized radar images. In *25th Asilomar Conference on Signals, Systems & Computers*. IEEE Computer Society, November 1991.
- [67] A. Ukrainec and S. Haykin. Signal processing with radial basis function networks using expectation maximization algorithm clustering. In *SPIE 36th International Symposium on Optical and Optoelectronic Applied Science and Engineering*, July 1991.
- [68] A. Ukrainec and S. Haykin. Enhancement of radar images using mutual information based unsupervised neural network. In *Canadian Conference on Electrical and Computer Engineering*, pages MA6.9.1-MA6.9.4, Toronto, Canada, 1992.
- [69] Mark R. Walker and L. A. Akers. Information-theoretic analysis of finite register effects in neural networks. In *International Joint Conference on Neural Networks*, volume II, pages 666-671, Piscataway, NJ, 1992. IEEE.
- [70] B. Widrow and S. Stearns. *Adaptive Signal Processing*. Prentice-Hall, Englewood Cliffs, N.J., 1985.
- [71] B. Widrow et al. Adaptive noise cancelling: Principles and applications. *Proceedings of the IEEE*, 63(12):1692-1716, 1975.

- [72] John M. Wozencraft and Irwin Mark Jacobs. *Principles of Communication Engineering*. John Wiley & Sons, NY, 1965.
- [73] Richard S. Zemel and Geoffrey E. Hinton. Discovering viewpoint-invariant relationships that characterize objects. In Richard P. Lippmann, John E. Moody, and David S. Touretzky, editors, *Advances in Neural Information Processing Systems 3*, San Mateo, CA, 1991. Morgan Kaufmann Publishers.